Università degli Studi di Sassari
Università degli Studi di Cagliari

Preparation and Optical Properties of Boron Nitride Nanomaterials and their Nanocomposite Films

By

Junkai Ren

Supervisor:

Prof. Plinio Innocenzi

Coordinator:

Prof. Carla Cannas

To the challenges that I have encountered

To the people who have helped me in life and study

To my family for their continuous support and encouragement

PHD DEGREE

CHEMICAL SCIENCE AND TECHNOLOGY

CYCLE XXXIV

SCIENTIFIC DISCIPLINARY SECTOR

ING-IND/22 - MATERIALS SCIENCE AND TECHNOLOGY

Preparation and Optical Properties of Boron Nitride Nanomaterials and their Nanocomposite Films

By

Junkai Ren

Supervisor:

Prof. Plinio Innocenzi

Coordinator:

Prof. Carla Cannas

Final Exam. Academic Year 2020 – 2021

Thesis defense: May 2022 Session

Biography

Junkai Ren obtained his B.E. degree in materials forming & control engineering from Changsha University of Science & Technology (CSUST, China) in 2015 and received his M.S. degree in chemistry & physics of polymers from University of Chinese Academy of Sciences (UCAS, China) in 2018. He now is a Ph.D. student in chemical sciences & technologies in University of Sassari and Cagliari (UniSS-UniCA, Italy). Currently, he works at the Laboratory of Materials Science and Nanotechnologies (LMNT) to explore the optical properties of boron nitride nanomaterials and develop functional applications based on their nanocomposites.

Preface

Hexagonal boron nitride (*h*-BN) represents one of the most popular two-dimensional (2D) materials whose excellent properties are expected to have great potentials in electronics and optoelectronics. The fabricated *h*-BN nanostructures are usually composed of dangling bonds at the edges and saturated sp^2 BN bonds in the domains, in general, which also contain carbon, oxygen, and hydrogen impurities. As far as we know, the defects play a primary role in creating new properties of 2D *h*-BN, for example, enhanced absorption, emerging fluorescence, and photocatalytic activity. Therefore, managing and tailoring defects in *h*-BN systems is a key process for the exploitation of their advanced functions. However, clear correspondences of defects and properties still have not been well established in terms of *h*-BN basic research. In particular, the present carbon impurities heavily cause uncertainty in modulating and understanding the optical properties of *h*-BN systems. Herein, this **Thesis** has mainly focused on exploring the relationship between structure defects and optical properties of *h*-BN nanosheets and nanodots. Both the BN sheets and dots are produced using a carbon-free process for the targets of introducing special defects and thereby understanding the corresponding defect-property causality. Simultaneously, quantum chemistry calculations have been carried out to support the experimental findings. Subsequently, sol-gel chemistry has been applied to fabricate their nanocomposites by respectively incorporating the synthesized sheets and dots into transparent films (i.e. titania TiO_2 and silica SiO_2), which determine their possibility in solid-state devices in the fields of photocatalysis and light-emitting applications.

Contents

Chapter 1. Optics in Hexagonal Boron Nitride: An Introduction of This Thesis

At the beginning of the present thesis, we have summarized the main state-of-the-art in the preparations, properties, and applications of hexagonal boron nitride (h-BN) related materials, from bulk to nanoscale systems. In particular, the optical features of BN materials are presented; both nanodots and nanosheets are highlighted. After reviewing the current research, the purpose is put forward, as well as a brief introduction of this PhD project is shown.

1.1. Broad family of boron nitride allotropes

Boron nitride (BN), the compound of boron (B) and nitrogen (N) atoms, is a kind of chemically and physically stable materials. BN is an isomorphism of carbon (C), which also has two phases bonded by sp^2- or sp^3- hybridization.[1] In general, there are main four types of crystalline BN polymorphs, as shown in **Figure 1.1**, including hexagonal (h-), cubic (c-), rhombohedral (r-), and wurtzite (w-) BNs.[2]
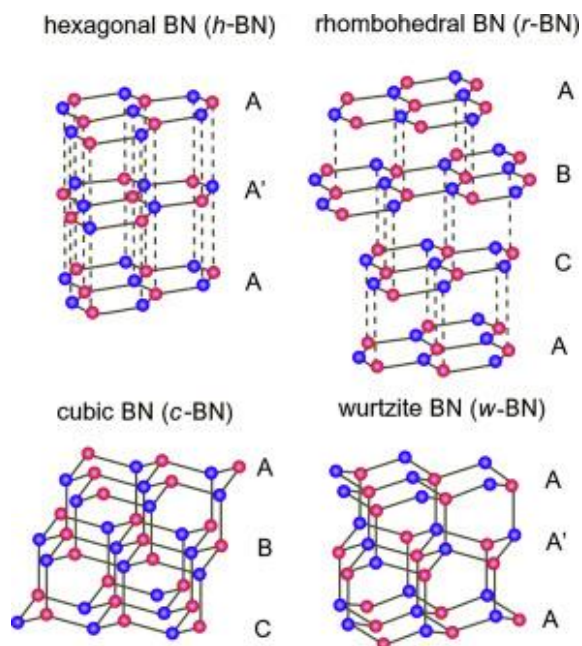
Figure 1.1 Structural models of the four types of BN phases, including h-, r-, c-, and w-BNs. Reproduced from Ref.[2] with permission of Copyright (2019) Elsevier Inc.

The most common one is h-BN, which presents sp^2 hybridized B-N bonds in each plane, where different planes are kept interacting via *van der Waals* forces. A graphite-like hexagonal network is shown with the lattice parameters of $a = 2.504$ Å and $c = 6.661$ Å. The special structure further allows h-BN to be a popular candidate in two-dimensional (2D) materials preparations and applications.[3] h-BN shows super high stability in extreme conditions, such as high temperature (up to 1000 °C in air), concentrated acids, or concentrated alkalis. The production of h-BN is usually carried out via a chemical vapor deposition (CVD) route with boric acid and urea, etc., as precursors.

The r-BN polymorph is also sp^2- bonded but with a rhombus as its basic unit, where the lattice parameters are $a = 2.498$ Å and $c = 9.962$ Å. Actually, a lot of experiments show that a pure and single r-BN crystal cannot be obtained without the presence of an h-BN system.[4] Therefore, the knowledge is still poor about physical and chemical properties in r-BN materials.

c-BN is composed of sp^3 B-N bonds and constructed by face-centered cubic B and N two cells with a lattice constant of $a = 3.615$ Å. The diamond-like structure of c-BN endows it with ultra-high hardness as well as outstanding thermal conductivity.[5] It thus has been applied as coating materials for cutter, anticorrosion, and heat dissipation. The preparation of c-BN is also via the common route under the conditions of high pressure and temperature.

w-BN is another structure consisting of sp^3 B-N bonds but arranged in a different way, in which B and N atoms are arrayed in a lonsdaleite configuration with lattice parameters of $a = 2.553$ Å and $c = 4.228$ Å. Similar to the r-BN situation, w-BN is far from being comprehensively understood because of the difficulties in the production of a single phase.[6]

Additionally, other phases of BN have often been discovered in some experiments. For example, the turbostratic (t-) phase of BN is linked by sp^2- B-N bonds like h- and r-BNs, but its form is disordered in the stacked axis. Therefore, the diffraction patterns

of *t*-BN are usually exhibited with much broader signals in 2θ than those of the pure phase of *h*- or *r*-BNs.[7] Apart from these crystalline phases, non-crystalline form is reported as amorphous (*a*-) BN, which is mainly sp^2- bonded. *a*-BN materials are well known for their excellent electronic properties, for instance, low dielectric constant.[8]

1.2. Nanomaterials of hexagonal boron nitride

A hexagonal geometry endows *h*-BN layers (see **Figure 1.2a**) with many characteristics similar to graphite.[9] Therefore, 2D *h*-BN is usually named "white graphene". Actually, the layered structure makes *h*-BN units flexibly form different nanomaterials. Considering the structural category, there predominantly are five kinds of popular nanoallotropes from both carbon and BN cells, including nanosheets, nanoribbons, nanotubes, fullerenes, and nanodots. In the case of BN nanomaterials (**Figure 1.2b-f**), they are termed as BNNSs, BNNRs, BNNTs, BN fullerenes (or cages), and BN nanodots (or quantum dots, QDs), respectively.
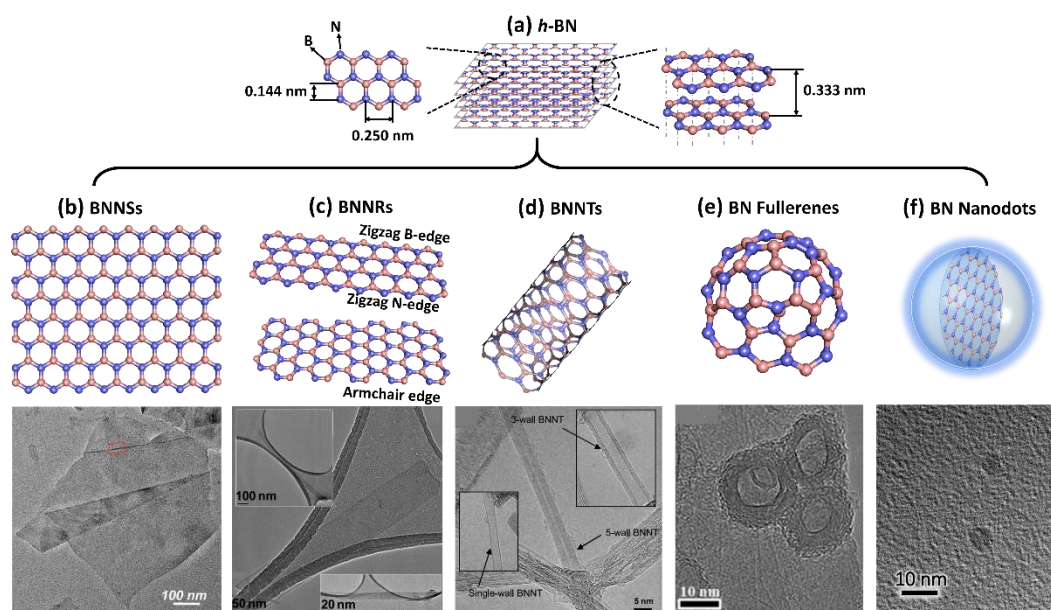
Figure 1.2 Schematic structures of (a) *h*-BN crystal, and its nanomaterials of (b) BNNSs, (c) BNNRs, (d) BNNTs, (e) BN fullerenes, and (f) BN nanodots. Reproduction with modification from Ref.[9] and Ref.[10] with permission of Copyright (2020) Springer Nature and Copyright (2021) Elsevier B.V.

1.2.1. 2D boron nitride nanosheets

Since monolayer graphene was firstly prepared and identified in 2004, various 2D materials have received unprecedented attention. Among them, 2D *h*-BNNSs have represented the most important role in BN-related systems, whose size is restricted to nanoscale in thickness direction but infinite in other two dimensions.[11-12] Diverse synthesis routes have been developed for the production of high-quality BN sheets via the typical top-down exfoliations and bottom-up growths. The applicability of different approaches depends on the dimension, purity, defects, etc. of the final products, as well as the costing, yield, and time of producing process.[13]

Top-down exfoliations

Mechanical force via cleavage technique can directly break *van der Walls* interactions of BN interlayers to achieve top-down exfoliation of the bulk crystals.[14] The shear force of the ball-milling system can also peel off thick and large *h*-BN into some fragments with few layers.[15] The introduction of chemical reagents, such as hydroxides and urea, can benefit a synergetic effect of kinetic energy and chemical peeling, which simultaneously allows the surface-functionalization of BN with -OH and -NH$_2$.[16-18] As shown in **Figure 1.3a**, Lee et al. have used NaOH solution to assist the ball-milling process, where a reaction is activated between *h*-BN and OH$^-$ ions on the edges and in-plane B sites.[16] The yields can reach up to 18%, and the resulting flakes have an average lateral size of 1.5 μm and thickness of 2.62 nm.

Liquid-phase exfoliation is another common top-down method to overcome BN *van der Walls* interactions under the assistance of sonication (bath or tip types) and surface tension of polar solvents.[19-22] Similar to ball-milling, various additives have already been used to promote exfoliation and functionalize products.[23-25] It should be noted that water has proven a special liquid phase with respect to organic solvents because of its critical role for creating hydroxyl defects.[20, 22] **Figure 1.3b** shows a three-step route to improve product yield of exfoliated BN sheets: (i) the sonication of *h*-BN in water can produce -OH groups and penetrate H$_2$O molecules into layers; (ii) the explosion of

water upon thermal treating can expand the space of BN interlayers; (iii) water-phase sonication again can allow producing hydroxyl-functionalized nanosheets.[19] The obtained BNNSs show an average lateral size of 0.58 μm and thickness of 3 – 8 nm; the yield of this green method even can reach 37%. Besides, it should be highlighted that the presence of defects has endowed *h*-BNNSs with more interesting functions beyond the pristine ones, such as emerging fluorescence (see our case in ***Section 4.1***)[22] and enhanced photocatalytic response (in ***Section 4.2***).[26]
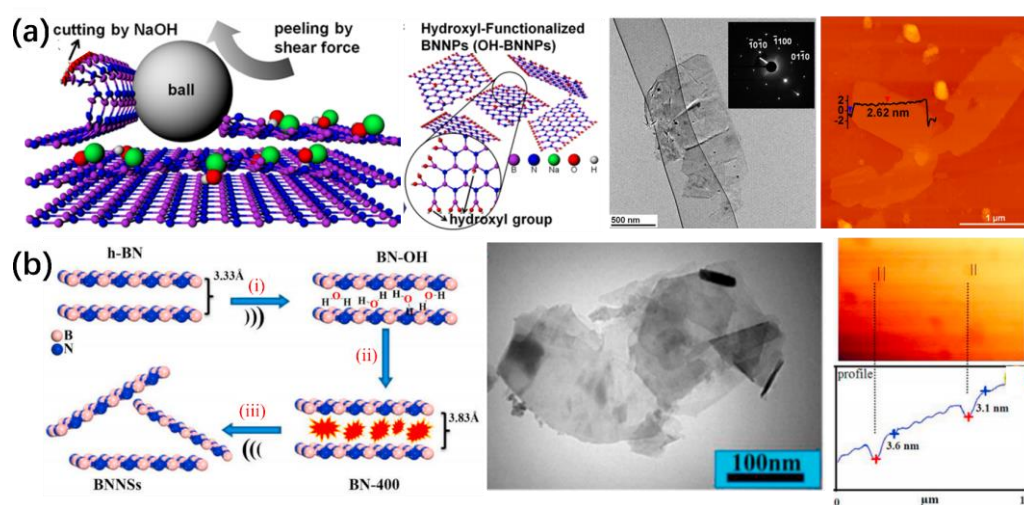
Figure 1.3 (a) The one-pot preparation of BNNSs via hydroxide-assisted ball-milling method. Reproduced from Ref.[16] with permission of Copyright (2015) American Chemical Society. (b) The three-pot fabrication of BNNSs by thermal-assisted hydrolysis and sonication exfoliation. Reproduced from Ref.[19] with permission of Copyright (2020) Elsevier Ltd.

Bottom-up growths

The bottom-up growths start from boron and nitride-containing components (e.g. ammonia borane, borazine, *β*-trichloroborazine, diborane/decaborane, and ammonia, etc.), which allows the precursors to react and assemble into a hexagonal structure.[27] The growths can further be divided into two classifications according to whether a substrate is used or not. The substrate-dependent one is usually carried out via chemical vapor deposition (CVD) methods, and the widely used substrates include Cu, Ni, Si, Fe, Ru, Pt, and so on. CVD is the main tool to allow the production of *h*-BN monolayer. For example, Song and co-workers have reported a wafer-scale growth of *h*-BN films by depositing on Cu (111) face via CVD process (see **Figure 1.4**).[28] The resulting BN

sheets show a triangular shape, and the domain edge length can reach 72 μm with a 92% percentage of the monolayer. In another hand, the CVD can also be conducted without substrates, for instance, directly performed from boric acid and melamine in a graphite crucible.[29]
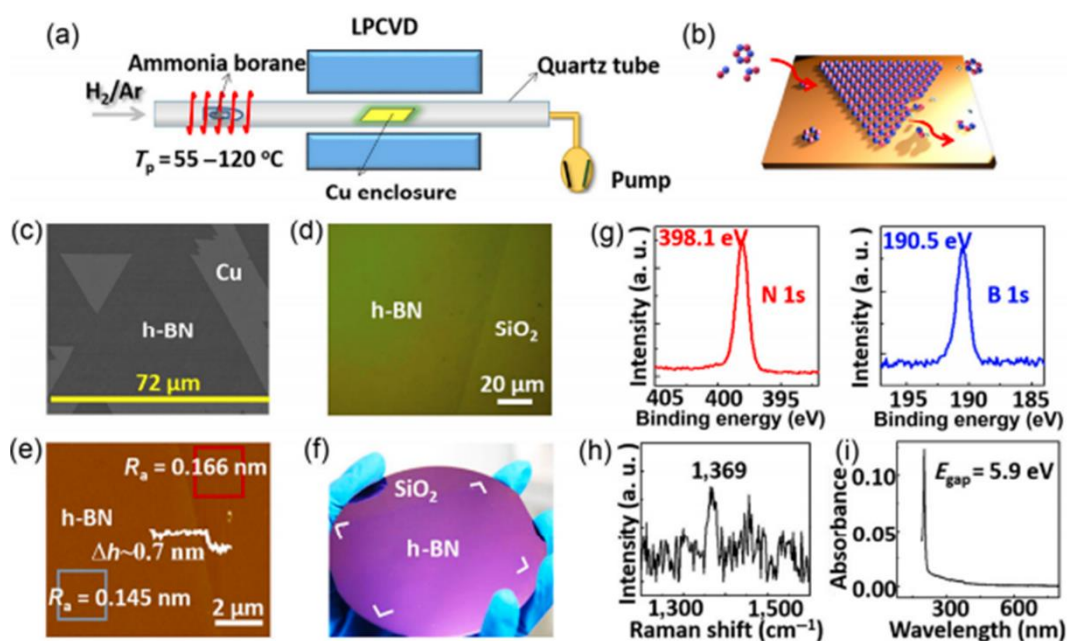
Figure 1.4 Large-area synthesis and characterizations of *h*-BN films via CVD process. Reproduced from Ref.[28] with permission of Copyright (2015) Springer Nature.

Besides, physical vapor deposition (PVD) is another bottom-up process to synthesize *h*-BNNSs. The vapor can be generated by thermal evaporation or sputtering of the *h*-BN source.[27] In recent years, some unconventional techniques have been developed for a gram-scale production of BN sheets, such as, via chemical-blowing synthesis from ammonia borane,[30] and biomass-directed route from boron oxide and nitrogen.[31]

1.2.2. 1D boron nitride nanotubes

Inspired by the discovery of carbon nanotubes in 1991, BNNTs were theoretically proposed in 1994 and experimentally synthesized in 1995.[32] They can be depicted as a rolled *h*-BN monolayer or multilayer, representing a single or multi-walled tube. It should be mentioned that the tubular interspacing is a bit larger than the layered one.[33] Both multi or single-walled BNNTs have been well developed and fabricated in the past decades, and the preparation of later ones is a more difficult design. Herein, **Table 1.1**

shows a summary of typical synthesis techniques for high-quality BNNTs according to several review articles.[32, 34]

Table 1.1 Synthesis techniques for BNNTs.

Methods	Precursors	Comments
Arc-discharge; 3500 °C	• h-BN; • B, YB_6, or ZrB_2; • N_2	➤ High crystallization, both single and multi-walled tubes; ➤ Containing impurities of BN onion and cages.
Laser ablation; 1200 or 5000 °C	• h-BN, or c-BN	➤ High crystallization, both single and multi-walled tubes; ➤ Containing impurities of BN cones.
Template synthesis; 750, 1000, or 1580 °C	• $B_3N_3H_3Cl_3$ or BH_3NH_3; • B_2O_3; • NH_3 or N_2	➤ Controlled morphology; ➤ Containing impurities of carbon in lattice.
Autoclave; 600 °C	• NH_4BF_4; • $Mg(BO_2)_2$ or B; • NH_4Cl, NH_3 or N_2	➤ Low-temperature process; ➤ Low quality and yield, containing impurities of B and BN cages.
Ball-milling; 1000 – 1200 °C	• B; • NH_3	➤ High yield; ➤ Poor purity, containing impurities of B and BN fiber.
CVD; 600, 800, 1100, 1200, or 1500 °C	• BH_3NH_3 or BN; • B, B_2H_6, B_2O_3, $NaBH_4$ or H_3BO_3; • NH_3, N_2, NH_4Cl or Urea	➤ High quality, gram-scale production; ➤ Requiring a special method with parameters.

1.2.3. 0D boron nitride nanodots

As an emerging kind of 0D materials, BN nanodots or quantum dots (QDs) have attracted increasing interest for their excellent properties, such as strong photoluminescence, large surface/volume ratio, high aqueous solubility, and good biocompatibility.[13, 35] The feature advantages make BN dots a promising candidate for numerous potential applications in the fields of photonics, optoelectronics, sensors, and biology.

Top-down routes

Although the studies on this type of nanodots are still in an early stage, the synthesis approaches, as well as potential applications, have been wildly explored and developed in the past few years. The top-down routes are the most used methods for the preparation of BN dots, which allow exfoliating bulk *h*-BN into sheets and further cracking them into fragments. As shown in **Figure 1.5a-b**, Liu et al. have fabricated a kind of monolayered BN QDs by exfoliation and disintegration of *h*-BN flakes, where a reaction is conducted between the intercalated potassium (K) in BN and ethanol-water solution under ultrasonication.[36] The QDs shows a blue emission under UV irradiation, and the authors have attributed the luminescence into three emissive defects (see **Figure 1.5c**): carbon-replaced nitrogen vacancies (e.g. 1, 3-B centers), zigzag carbene saturated edges, and BO_x^- species (x = 1, 2; the dominated mechanism in this case).
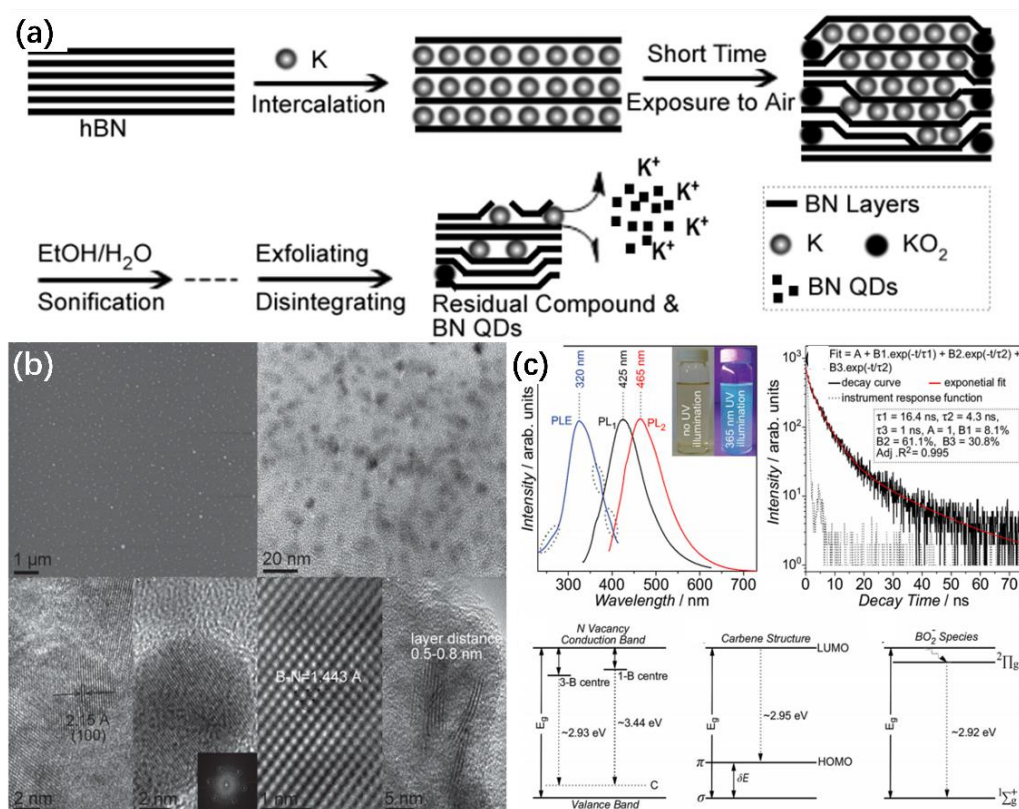
Figure 1.5 BN QDs produced via exfoliation and disintegration of *h*-BN flakes. (a) Schematic formation, (b) morphologies, and (c) luminescence characterizations. Reproduced from Ref.[36] with permission of Copyright (2013) John Wiley and Sons.

Currently, the main top-down strategy to obtain BN dots is the sonication-assisted or ball-milling liquid-phase exfoliation methods combined with refluxing, solvothermal, microwave-irradiation, laser-ablation treatments, etc. The former process results in the exfoliated BN sheets; the latter operation can further incise and cut the layers into nanosized dots. An example is shown in **Figure 1.6**, where the BN dots are fabricated by solvothermal treating the sonication-exfoliated sheets in dimethylformamide (DMF).[37] The dots with a size of 2.62 nm show strong blue emission and quantum yield (QY) up to 19.5%. Importantly, the BN QDs properties (including size, surface groups, and fluorescence intensity) can be tailored by controlling the solvothermal parameters (e.g. filling factor, reacted temperature, and time). In addition, Liu and co-workers have further found that the selection of solvents is a significant factor to regulate the color of emission spectrum.[38]
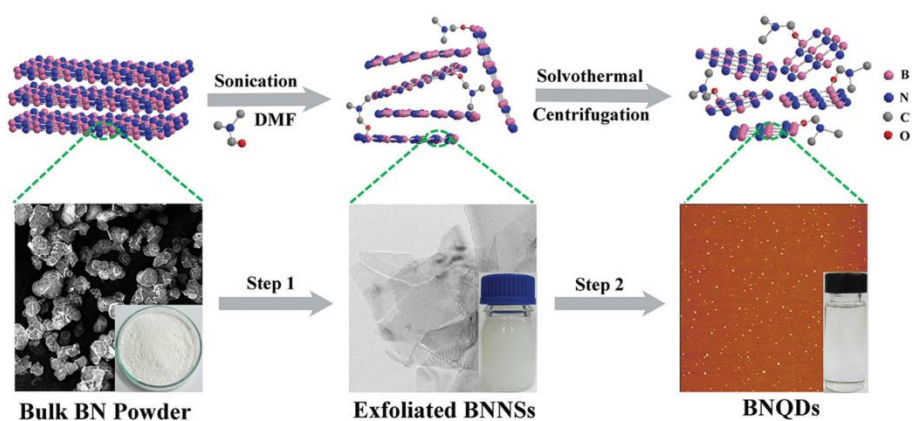
Figure 1.6 BN QDs produced via sonication and solvothermal process. Reproduced from Ref.[37] with permission of Copyright (2015) John Wiley and Sons.

Some novel approaches have also been performed through unconventional designing. For instance, a defect-engineering method has been reported to induce physical defects by heating iron nanoparticles and *h*-BN together. Subsequently, BN dots are produced via microwave and sonication treatments; then water-vapor exposure makes the nanodots edge-hydroxylated for the target of bioimaging.[39] In a report by Thangasamy et al., the exfoliation and disintegration of bulk BN crystals can be realized by a supercritical fluid process that allows rapid fabrication of blue emissive BN QDs.[40]

Duong and co-workers have obtained BN nanoparticles with a size of 3 nm using a cryogenic exfoliation followed by sonication, centrifugation, and filtration.[41] In the cryogenic process, the bulk powders are firstly soaked in liquid nitrogen and then thermally shocked in isopropanol-water solvent to peel off *h*-BN and introduce defects. In another study, thermal-induced intercalation plus sonication in phosphoric acid can result in progressive etching and size reduction of bulk BN into nanodots (see our case in *Section 5.2*).[10]

Bottom-up synthesis

With respect to the lengthy top-down process, the production of BN QDs via bottom-up technique describes a facile and effective route starting from boron and nitrogen sources. It usually involves hydrothermal, solvothermal, microwave-radiation, and calcination treatments. Herein, **Table 1.2** summarizes a series of bottom-up grown BN dots and their optical properties.

Generally speaking, top-down routes are lengthy processing and show a poor yield, but the crystallinity of the fabricated BN dots can be well inherited from the bulk powers. On the contrary, bottom-up methods can allow mass production of BN QDs only via a simple process, whilst they are mainly amorphous with a very limited and even negligible presence of *h*-BN crystalline phase (see our case in *Section 5.1*).[42]

Table 1.2 A summary of BN nanodots via bottom-up synthesis.

Precursors	Methods	Properties	Ref.
H_3BO_3; $NH_3 \cdot H_2O$	Hydrothermal reaction; 200 °C for 12 h; No purification.	PL at 395 nm, QY = 18.3%; Size 2.38 nm.	[43]
	Hydrothermal reaction; 200 °C for 12 h; pH=7 by HCl, and dialysis.	PL at 400 nm, QY = 32.3%; Size 4 nm.	[44]
	Hydrothermal reaction; 200 °C for 12 h; Dialysis.	Two emissions at 390 and 470 nm, QY = 7.4 and 4.6%; Size 10.2 nm.	[42]
H_3BO_3; $C_3H_6N_6$	Hydrothermal reaction; 200 °C for 15 h; No purification.	PL at 400 nm; Size 3 nm.	[45]

H_3BO_3; $CO(NH_2)_2$	Hydrothermal reaction; 200 °C for 15 h; Dialysis.	PL at 414 nm, QY = 5.9%; Size 4.04 nm.	[46]
H_3BO_3; $CO(NH_2)_2$	Solvothermal reaction; EtOH-H_2O, 200 °C for 12 h; Filtration and centrifugation.	PL at 330 nm; Size 3.2 nm.	[47]
H_3BO_3; $CO(NH_2)_2$	Microwave-radiation; 1000 Hz, 120 °C for 70 min; Centrifugation.	QY = 10.31%; Size 4.04 nm.	[48]
H_3BO_3; $CO(NH_2)_2$; $SC(NH_2)_2$		Sulfur-doping, QY = 8.9%; Size 9.8 nm.	
H_3BO_3; $CO(NH_2)_2$; H-Cys-OH		Sulfur-doping, QY = 2.0%; Size 9.2 nm.	
H_3BO_3; $C_3H_6N_6$	Microwave-radiation; 1000 Hz, 180 °C for 80 min; Centrifugation.	Electrochemiluminescence at 555 nm	[49]
H_3BO_3; $C_3H_6N_6$; NH_4F		Electrochemiluminescence at 575 nm; Fluorine-doping.	

1.3. Optical properties of hexagonal boron nitride systems

Recent research shows that *h*-BN possesses a wide bandgap of ~6 eV, a low dielectric constant of 2 – 5, high thermal conductivity up to 751 W mK^{-1} at room temperature as well as good chemical inertness.[50] These unique properties enable the *h*-BN of a promising candidate in a broad range of optical and electro-optical fields. Herein, the optical properties of *h*-BN are mainly discussed.

1.3.1. Band structure

In *h*-BN layer, B and N atoms are sp^2 hybridized; each B (or N) atom can generate three σ bonds with its immediate N (or B) atoms, consequently six electrons of a cell filling into the σ orbit. There are eight electrons in a BN cell, and the remaining two in *p* orbital (p_z) can form the vertical plane π bond.[51]

It has been reported that *h*-BN crystal shows both direct and indirect bandgap properties.[52-53] Theoretical calculation has been wildly performed to evaluate the band structure of *h*-BN based on density functional theory (DFT) with local density

approximation (LDA). However, the standard DFT process generally underestimates the bandgap energies.[13] Therefore, Green's function quasiparticle (GW) method can be used to correct DFT results. As shown in **Figure 1.7**, Arnaud et al. have calculated a minimum direct gap of 6.47 eV and an indirect gap of 5.95 eV via the GW approach, whilst the underestimated results are respectively 4.46 and 4.02 eV via the LDA method.[54]
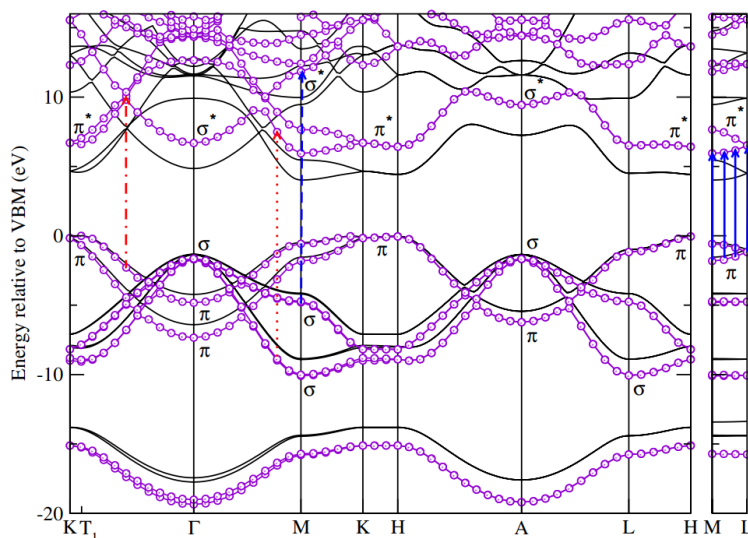
Figure 1.7 The calculated band structure of *h*-BN; the black solid lines represent the LDA results and the purple lines with circle display GW results. Reproduced from Ref.[54] with permission of Copyright (2006) American Physical Society.

1.3.2. Ultraviolet-Visible absorption

h-BN nanomaterials usually show an intense absorption band in the ultraviolet (UV) region of 190 – 220 nm and do not have optical absorption in the visible (Vis) region at 380 – 750 nm. The presence of defects in the BN structure can result in a shift of UV absorption peak, and also increase the absorption intensity in the visible area.[22, 55] For example, as shown in **Figure 1.8**, the introduction of -OH groups can not only improve the solubilization of BN sheets in water but also enhance the optical absorbance.[55] In another hand, when BN dots are generated, new bands will appear in their UV-Vis spectrum because of many defects and edge effects.[13, 35] The emerging bands further contribute to the UV and Vis fluorescence of BN dots under the corresponding excitation light.
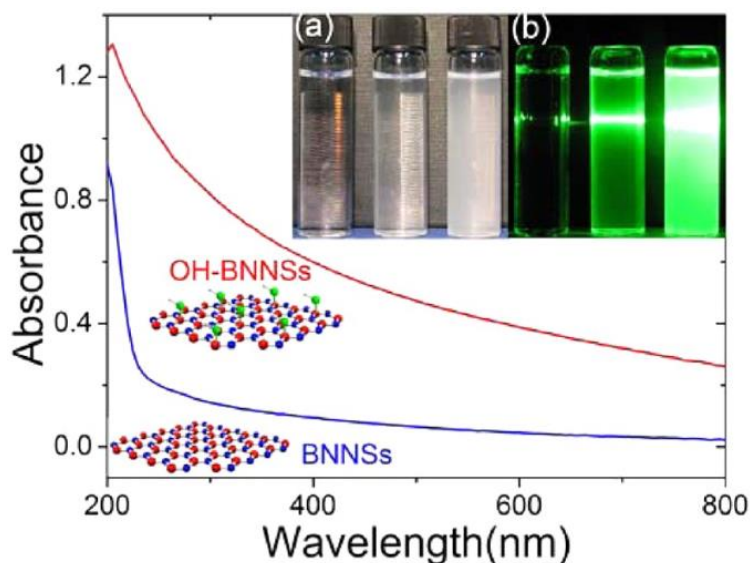
Figure 1.8 The UV-Vis absorption spectra of pristine and hydroxyl-functionalized *h*-BNNSs by dispersing into water. Reproduced from Ref.[55] with permission of Copyright (2012) American Chemical Society.

1.3.3. Photoluminescence

Luminescence properties of *h*-BN involve a broad range of cathodoluminescence (CL), photoluminescence (PL), photon emitter, laser emission, etc.[51] CL spectroscopy usually is corresponded to the near-band-gap structure, which is in the deep UV region.[52] PL emission can be attributed to the donor-acceptor pairs of localized centers in correspondence of defects coupled to the distal lattice points, where the visible light can make the carriers recombine in the traps.[56]

Figure 1.9 describes some typical defects in the 2D structure of *h*-BN.[57] There are generally three types of defects in *h*-BN nanomaterials contributing to PL emission at room temperature: B and/or N vacancies, carbon doping, and boron-oxygen species (e.g. BO_x^-, $x = 1$ or 2).[36, 58-59] Generally speaking, it is still highly different to distinguish the specific PL contributions from which defect. The vacancies are usually in charge of the emission in the UV region that is often observed from bulk *h*-BN with related defects.[39] The oxygen bonding in 2D layers is sensitive to the acid-base environment, hence the luminescence related to boron-oxygen species will change upon different pH conditions.[37, 39]

Carbon-induced defects can be further divided into carbon-replaced N vacancy point defects (3-B and 1-B centers) and zigzag carbene edge.[36-37] On the one hand, the emission can be created when the unpaired electrons transit from higher 1,3-B centers and lower carbon levels. On another hand, carbene structure at BN zigzag edges can also result in PL emitting, which shares a similar mechanism with graphene QDs. Very recently, Nguyen et al. have observed this kind of edge structures in fluorescent BN dots using HRTEM images and FFT patterns.[60]
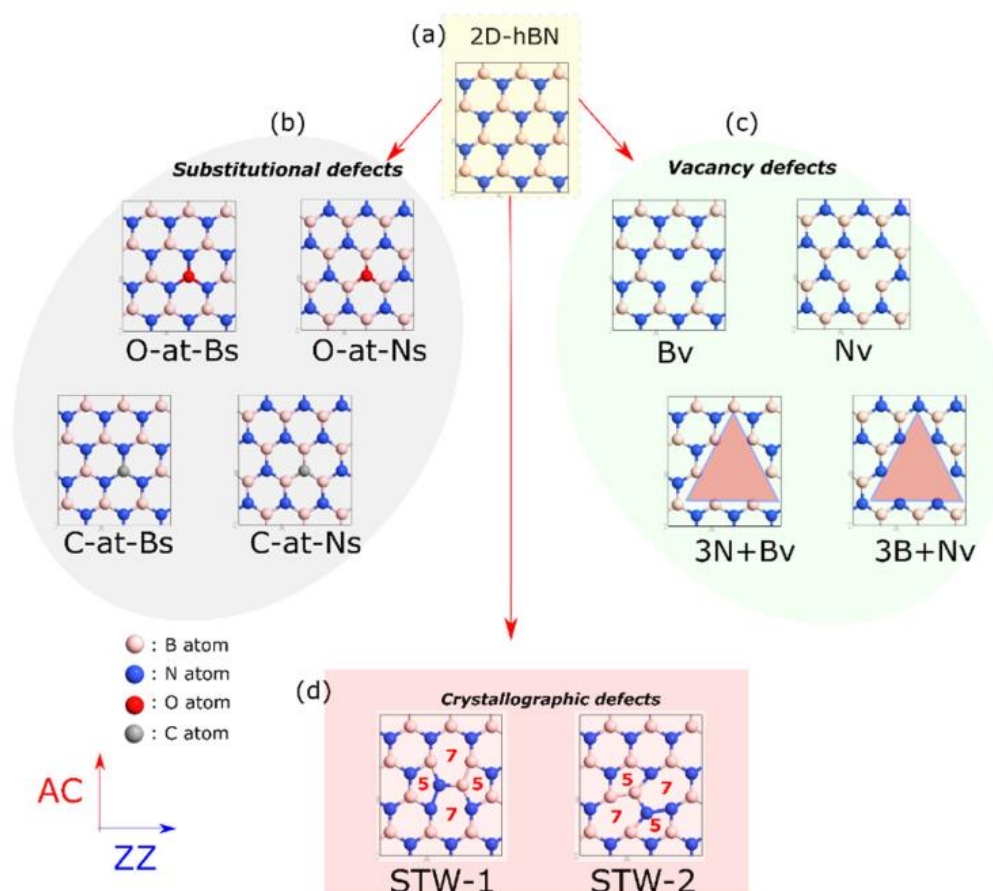
Figure 1.9 Different defects in the structure of 2D *h*-BN. Reproduced from Ref.[57] with permission of Copyright (2020) Springer Nature.

Unfortunately, the carbon impurities are causing challenging interferences for the origins of BN materials, in particular, BN QDs. Many researchers declare that they have obtained BN QDs using sonication-assisted solvothermal or microwave methods.[37-38, 61-63] However, the B content in their products can even be ignored according to their XPS survey and Raman spectra. In fact, they probably have obtained carbon dots due

to the carbonization of solvents or organic ligands. For example, Ding and co-workers have reported a strategy to produce full-color emissive BN QDs by solvothermal treatment of BN sheets with different amino ligands (see **Figure 1.10**).[63] In detail, when urea is used, they obtain blue light; when p-phenylenediamine is used, they obtain red light. However, they seem to forget the possibility that urea and *p*-phenylenediamine usually are used to prepare blue and red carbon dots, respectively. In addition, the B atoms in their BN QDs are less than 1% according to their XPS results.[63] It means that the presence or absence of BN sheets cannot contribute to a big change in the color of their final samples.
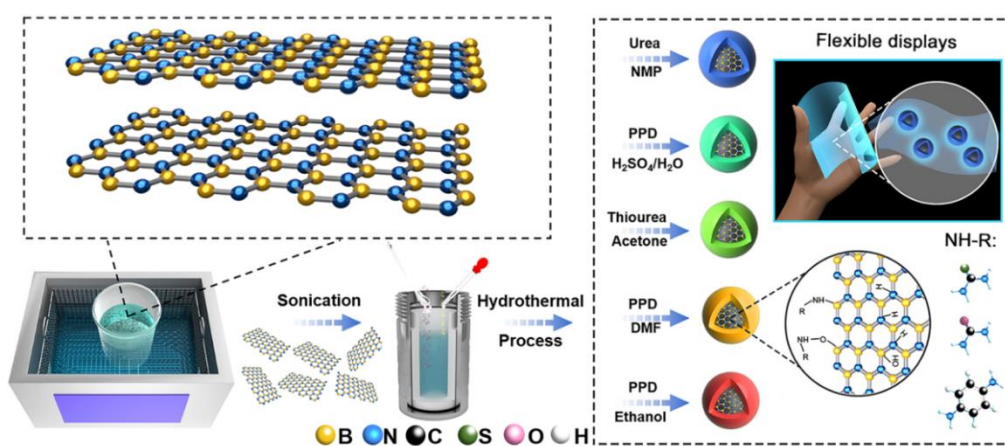
Figure 1.10 Schematic diagram of the preparation of full-color emitting BN QDs. Reproduced from Ref.[63] with permission of Copyright (2020) American Chemical Society.

1.3.4. Photocatalysis

In recent years, researchers have also focused on the incorporation of *h*-BNs as cocatalysts into semiconductor photocatalysts that can improve the catalysis effects in both organics degradation and water splitting.[64-65] However, the bare 2D *h*-BN materials do not have photocatalytic activity. Therefore, the combination of *h*-BN and semiconductor mainly contributes to the enhanced light absorption and charge-carrier-separation efficiency, which largely depend on the defects in BN structure and the formed heterojunction interface.[50, 66-67]

For example, Liu and co-workers have designed two types of BN-TiO$_2$ composites using porous and non-porous *h*-BN sheets, respectively.[68] The presence of porous *h*-

BNNSs can greatly improve the photocatalytic effect of TiO_2, whilst the non-porous sheets seem to make a negligible contribution. The authors think that the enhancement can be assigned to good dispersion of TiO_2 on BN sheets (see **Figure 1.11a-b**), and, in particular, the formation of special B-O-Ti bands between the boron dangling bonds at the open edges of pores in porous BN nanosheets and TiO_2 particles (see **Figure 1.11c-d**). **Figure 1.11e** furthermore explains the mechanism of B-O-Ti bonds in photogenerated reaction, which, on one hand, can lead to a narrow bandgap of the resulted heterostructures; on another hand, easily promote the transformation of generated electrons from TiO_2 conduction band to porous BN sheets.
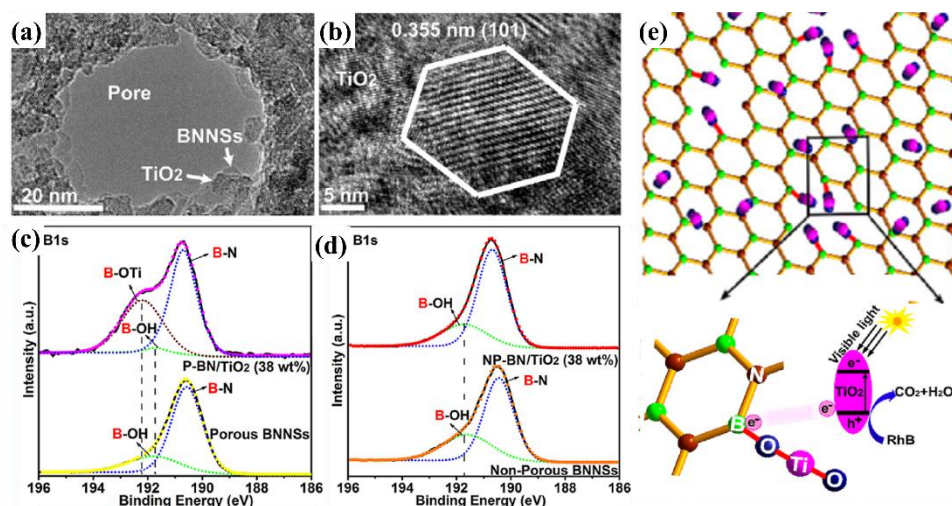
Figure 1.11 h-BN-TiO_2 photocatalyst. (a, b) TEM images of porous h-BNNSs and TiO_2 nanoparticles. (c, d) XPS B1s spectra of porous and non-porous BN nanosheets, as well as their TiO_2-hybrids. (e) Schematic diagram for the photocatalytic effect of porous BNs-TiO_2 heterostructure. Reproduced from Ref.[68], with permission of Copyright (2017) Elsevier.

1.3.5. Others

2D h-BNs are also a kind of nonlinear optical (NLO) materials that show strong optical limiting performance in a broad band range. Zhao and co-workers have prepared h-BNNSs by ions-intercalation assisted exfoliation and their dispersions in water show good NLO response with a positive nonlinear absorption coefficient under excitation at both 532 and 1064 nm.[69] The positive coefficient represents a potential application in the optical limiting field. For solid-state practical devices, Xie et al. have embedded hydrophilic BN sheets into an organically modified silicate matrix by a sol-gel way.[70]

The fabricated hybrid glass also shows outstanding optical limiting properties in an ultra-broadband range from 532 to 2000 nm.

Researchers have used 2D h-BNs in combination with Au or Ag for surface-enhanced Raman scattering (SERS).[71-72] Firstly, h-BN shows no remarkable signals and does not cause interference on the Raman spectrum of analyte; in another hand, h-BN surface possesses a better affinity for aromatic molecules. It should be noted that the SERS signals from h-BN monolayer are stronger than those from multilayer and bulk BN, as results of the empowered surface adsorption capability of h-BNNS for molecules.[71]

1.4. Purpose of this thesis

2D h-BN nanosheets, also named "white graphene", are representing one of the most popular layered materials whose excellent properties are expected to have great potentials in biology, electronics, and optoelectronics.[73] In one hand, the preparation of high-quality h-BN structures with fewer defects can achieve the maximization of their intrinsic properties, such as thermal conductivity and electrical insulation.[74] In another hand, the introduction of tailored defects can endow 2D h-BN with new properties, such as enhanced absorption, rising fluorescence, and improved photocatalytic activity.[50] Therefore, managing defects in h-BNNSs is a key process for good exploitation of their advanced functions. However, a clear relationship between defects and properties still has not been comprehensively explored in terms of h-BN basic research.

BN nanodots are composed of dangling bonds at the edges and saturated sp^2 BN bonds in the core, in general, which also contain carbon, oxygen, and hydrogen impurities.[10, 35] Although their exploration is still in a nascent stage, the excellent luminescence and non-toxic feature have allowed BN dots to become a new generation of fluorescent materials in optoelectronic and biomedical applications.[75-76] As far as we know, defects play a primary role in the emissive properties of BN nanodots. However, it is challenging to realize controlled fluorescence from BN dots because of unmanaged defects and unclear luminescent mechanisms. In particular, the present

carbon impurities heavily cause uncertainty in modulating and understanding the emissive properties of BN systems.
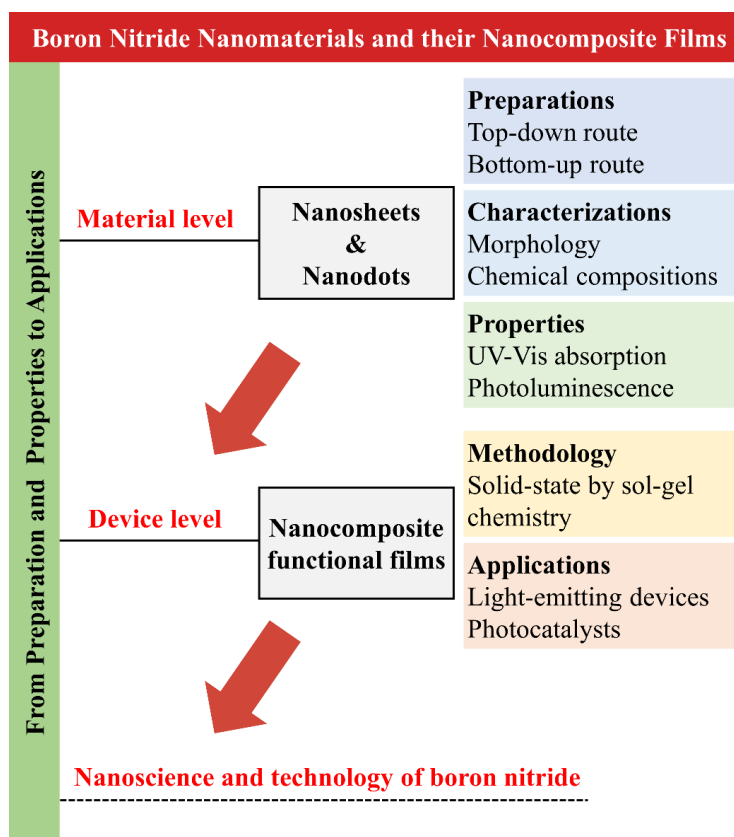
Figure 1.12 Graphical abstract of the thesis to show the main routes for the preparation of BN nanomaterials and their nanocomposite films.

In perspective, a better understanding of multiple defects largely determines the possibilities to create new properties of *h*-BN layered materials and develop their advanced functions. Herein, this **Thesis** has focused on the optical properties of the layered *h*-BN structure by the preparation and characterizations of BN nanosheets and nanodots. Particular attention has been paid to the correspondence of optical features and structural defects via analyzing fluorescence and exploring structure, combined with the assist of quantum chemistry calculations. Meanwhile, the sol-gel technique has been used to incorporate the synthesized nanomaterials into transparent nanocomposite films, which can envisage the future development of *h*-BN-based optoelectronic devices. **Figure 1.12** demonstrates the main routes to achieve the purpose of this ***Thesis***, which has mainly been divided into the following six chapters:

In **_Chapter 1_**, the state-of-art in BN materials has been summarized with a broad survey of the literature about _h_-BN. Particular attention has been devoted to the _h_-BNNSs and BN nanodots, in light of their optical properties.

In **_Chapter 2_**, the advanced characterizations of BN systems have been reviewed via studying current literature, such as morphology, structure, composition, and optics.

In **_Chapter 3_**, the used chemicals are listed, accompanied by the equipment of materials synthesis and characterization.

In **_Chapter 4_**, _h_-BNNSs have been prepared by sonication-assisted liquid-phase exfoliation of their bulk counterpart. On one hand, the exfoliation in water can make cavitation and produce hydroxyl-defective _h_-BNNSs which show fluorescence in the visible range (**_Section 4.1_**). On another hand, the exfoliation in dimethyl sulfoxide (DMSO) or N-methyl-2-pyrrolidone (NMP) only allows producing relatively defect-free sheets, consequently, without the corresponding emission. It highlights the critical role of hydroxylation and oxidation in the emissive feature as well as the rising optical absorbance of the 2D _h_-BN structure. Subsequently, the two kinds of nanosheets have been successfully incorporated into titania (TiO_2) mesoporous films to fabricate heterostructures using a template-assisted self-assembly technique (**_Section 4.2_**). Both bare and defective BN sheets do not show any photocatalytic property but can contribute to the anatase TiO_2 crystallization through heterogeneous nucleation. Importantly, the defects of _h_-BNNSs can further increase the absorbance in ultraviolet radiation A and thereby enhance the photocatalytic response of the heterostructure film. In a word, compared with the defect-free sheets, the tailored defects not only can induce visible fluorescence from the _h_-BN structure but also enhance the photocatalytic property of mesoporous BN-TiO_2 heterojunction.

In **_Chapter 5_**, both bottom-up and top-down approaches have been used to prepare fluorescent BN dots via a carbon-free process. Avoiding the presence of carbon impurities can allow revolutionizing the correspondence of structural defects and optical properties of BN dots. In the bottom-up case, the BN dots have been prepared

through a hydrothermal reaction of boric acid and ammonium. A series of characterizations including TEM, FTIR, XPS, and TGA-DTA have shown that the resulting nanoparticles possess a boron-oxynitride structure only with a limited amount of *h*-BN crystalline phase (***Section 5.1***). Interestingly, two-color emissions can be detected at 390 and 470 nm, respectively, which are corrected to network or BO_x^- defects in the oxynitride structure. In the top-down case, a combination of sonication and thermal treatments of bulk *h*-BN in phosphoric acid can achieve edge etching and size reduction, consequently creating defective BN nanodots. Significantly, the synthesized *h*-BN dots not only show general blue fluorescence but also a new emission in the UV region that is correlated to a characteristic infrared-active vibration (***Section 5.2***). Structural and optical characterizations have shown the relationship between the visible emission and the hydroxyl functionalization in the produced *h*-BN structure. Meanwhile, quantum chemistry calculations have been used to evaluate Stones-Wales defects as possible causes of the UV emission and the corresponding vibrational properties.

In ***Chapter 6***, the experimental works and conclusions are summarized, as well as a short discussion on future perspectives.

Chapter 2. Advanced Characterizations of Boron Nitride

This Chapter summarizes a series of techniques for the characterizations of boron nitride (BN) and its related materials, including morphology and composition analysis, as well as optical features.

2.1. Morphology analysis

Morphology analysis mainly focuses on size, thickness, and some morphological characteristics. The data can provide information on interlayer spacing, the number of layers, crystalline, and even some defects. Meanwhile, morphology measurements can also allow the chemical analysis of samples via assisted equipment.

2.1.1. Scanning electron microscopy

Scanning electron microscopy (SEM) is a commonly used measurement because of its simple sample preparation and easy operation, which allows capturing images in areas from micro to nano size. It is an electron microspore that can create an image by scanning sample's surface with a focused beam of electrons. The collected images can present information about both composition and topography. As seen in **Figure 2.1**, we can not only observe the morphology of *h*-BN doped by iron oxide, but also find the presence of 0.32 at% iron via an energy dispersive spectroscopy (EDS).[77] Furthermore, its elemental mapping reveals the uniform distribution of iron oxide on *h*-BN.
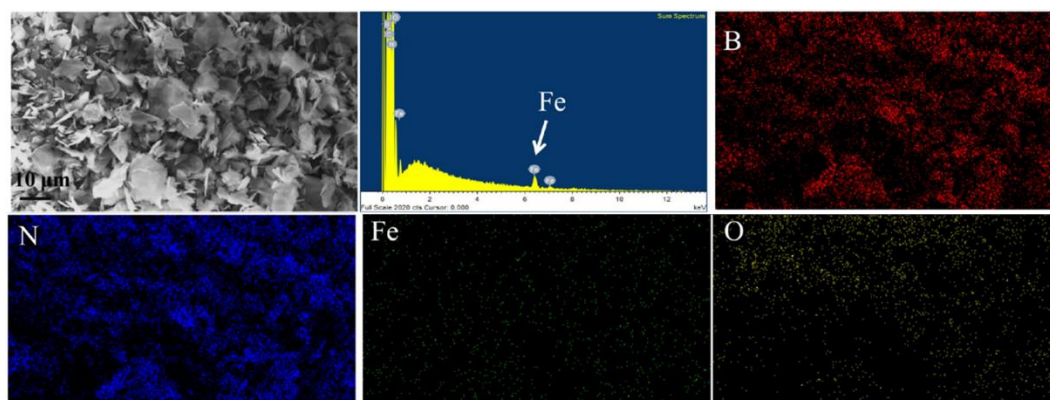
Figure 2.1 SEM image of iron oxide doping *h*-BN and its corresponding EDS and elemental mapping. Reproduced from Ref.[77] with permission of Copyright (2013) American Chemical Society.

2.1.2. Transmission electron microscopy

Transmission electron microscopy (TEM) has been the most popular approach to characterize nanomaterials by electron microscopy. It is an excellent tool to require internal structure and identify structural defects of BN materials under a high-resolution (HR) mode. As seen in **Figure 2.2a-c**, the layers of *h*-BN structure can be clearly observed from the HRTEM images.[78] Its crystallinity can be further examined via a selected area electron diffraction (SAED) in the TEM equipment, where the sixfold symmetrical spots reveal the hexagonal structure of BN (insert of **Figure 2.2a**).

An atomic TEM image can be collected when using aberration-corrected electron microscopy operated at low voltage, which reveals the lattice of BN (**Figure 2.2d**). Meanwhile, the interplanar spacings can be required from an atomic image, for example, 0.126, 0.217, and 0.33 nm corresponding to (11-20), (10–10) and (0002) planes, respectively.[79] A fast Fourier transform (FFT) analysis via the TEM process is also able to access the geometric characteristics (**Figure 2.2e**).
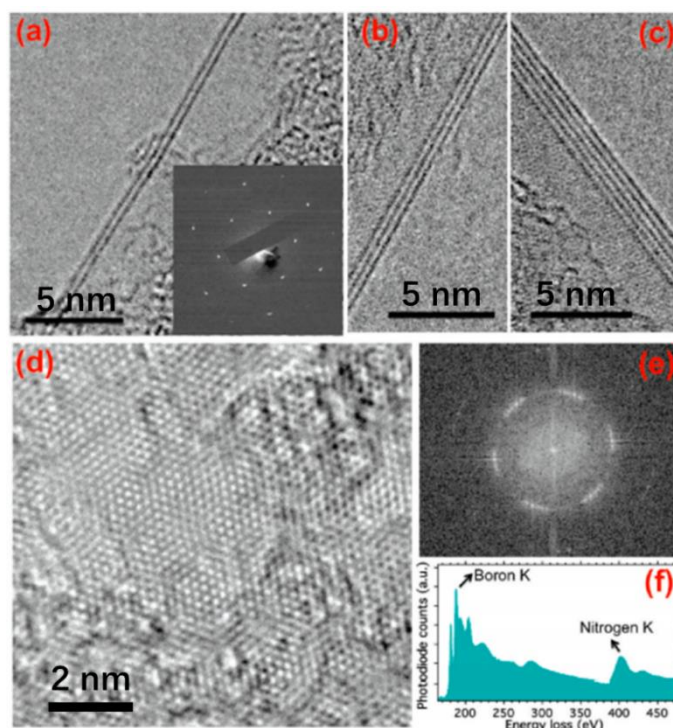
Figure 2.2 TEM analysis of *h*-BN layers. (a-c) HRTEM images of *h*-BN with 2, 3 and 5 layers, and the insert of (a) representing SEAD of the corresponding region. (d-f) An atomic HRTEM image and its FFT pattern, as well as an EELS spectrum of *h*-BN film. Reproduced from Ref.[78] with permission of Copyright (2010) American Chemical Society.

TEM usually equips with electron energy loss spectroscopy (EELS) instrumentation that regards chemical constituents of materials. **Figure 2.2f** shows an EELS spectrum of *h*-BN film with visible regions of B and N characteristic *K*-shell ionization edges. Another important information is that there are two bands in regions of both B and N elements, and the first one is attributed to *1s*-π^* antibonding orbit that means the nature of sp^2 configuration of *h*-BN. Interestingly, the EELS analysis not only reports composition but also permits identifying defects. For example, Cretu et al. have found that B-terminated tetravacancies can lead to the shift of π^* peak and a new appearing peak between π^* and σ^* bands of B *K* edge according to HR-EELS signature.[80]

2.1.3. Atomic force microscopy

Atomic force microscopy (AFM), a kind of scanning probe microscopy, captures information by the probe traveling near the specimen surface based on Hook's law (a scheme in **Figure 2.3a**). It permits information of height, friction, and magnetism of 2D materials via different measuring modes, such as friction, adhesion, electrostatic and magnetic interactions. **Figure 2.3b** shows two AFM images of the same BNNS area by adhesion (topography) and friction (lateral force) modes, respectively.[81] The layered morphology is well reflected in the two images. It should be noted that the fraction image, where the bright region corresponds to higher friction, can show a more detailed surface feature than the topography one.[82]

AFM is an excellent choice to intuitionally determine the thickness and consequent layer number of 2D nanomaterials. However, it is still a challenging task to make a precise determination of layer number in the cases of mono- or few-layer BN, because the trapped molecules between specimen and substrate (Si, SiO$_2$, or mica) cannot be neglected. Although the interlayer spacing is 0.333 nm for *h*-BN, a thickness of less than 1 nm usually is assigned to the result of a monolayer.[83-85] Therefore, other characterizations will be required to correlate with the final AFM-derived layer number. For example, **Figure 2.3c** describes a three-step profile of stacked BN layers showing heights of 0.54, 1.31, and 2.35 nm. The authors attribute them to one, three, and six

layers of BN domains after the correlation of Raman spectra (to be discussed in *Section 2.2*).[81]

Besides characterizations, the AFM scan has been developed as a tool of nanomachinery in fabricating nanomaterials. In a recent report of Yao et al., a rotation of BN homostructure is realized by adjusting the twist angle between stacking BN interfaces using nanomechanical energy derived by AFM tip.[86]
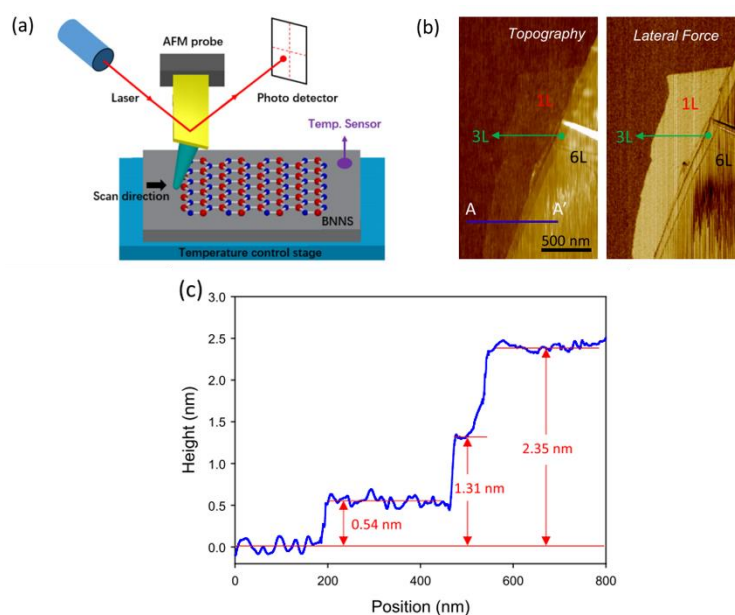
Figure 2.3 AFM analysis of *h*-BNNSs. (a) A technique scheme of AFM with temperature sensor. (b-c) AFM images and height profile of *h*-BNNSs. Reproduced from Ref.[81] with permission of Copyright (2017) AIP Publishing.

2.2. Structure and composition

Structure analysis can allow determining the phase of BN products; composition tests can show the chemical compositions and the present defects.

2.2.1. Fourier-transform infrared spectroscopy

Fourier-transform infrared spectroscopy (FTIR) can analyze chemical compositions, surface groups, and defects of BN materials according to the vibrational frequencies of different bonds. The operation usually requires a pellet of potassium bromide (KBr) or substrate of silicon wafer (e.g. films); in another hand, the equipment of attenuated total

reflection (ATR) can directly permit the infrared measurements of samples in solid state or liquid solvents.

There are two characteristic bands, E_{1u} and A_{2u}, in terms of *h*-BN. As seen in **Figure 2.4**, the former vibration represents in-plane B–N stretching mode at 1310 – 1400 cm^{-1} range; the latter one is the out-of-plane B–N–B bending band in the wavenumbers of 770 – 810 cm^{-1}.[1] However, it is impossible to distinguish BN phases via IR spectra, because *h*-, *t*-, and *a*-BNs show similar E_{1u} and A_{2u} peaks. In the case of cubic phase, there is generally only an IR peak located in 1050 – 1100 cm^{-1}, which allows identifying *c*-BN.[87-88]

It is inevitable to introduce some functional groups and defects when exfoliating bulk crystals into nanomaterials. Here are two examples of BNNS and BN dots in **Figure 2.4**. The common groups are the hydroxyl and amino species on B sites, as well as absorbed water, which appear in the high-wavenumber range of 2800 – 4000 cm^{-1}.[89-90] The oxygen-doping defects, e.g. N-B-O, usually are centered at the region of 850 – 1200 cm^{-1};[42, 91] the presence of boroxyl ring of O-B-O groups can cause the vibrational frequencies in lower wavenumbers of 400 – 700 cm^{-1}.[92]
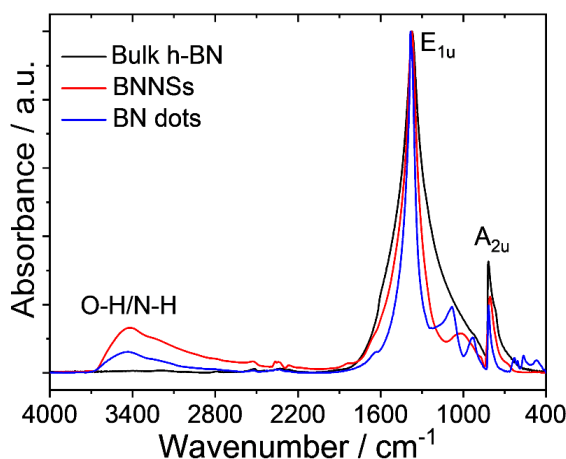
Figure 2.4 FTIR spectra of commercial bulk *h*-BN, top-down prepared BN nanosheets (see *Section 4.1*) and nanodots (see *Section 5.2*).

2.2.2. Raman spectroscopy

Raman spectroscopy can provide spectrum characteristics of specific intra- and inter-molecular vibrations that rely on measuring the interaction between laser light and

matter where the light is inelastically scattered. In particular, Raman scattering can show modes in a low-frequency region that permits important information on crystal lattices and backbone structures of samples.

Firstly, Raman scattering is useful to judge the crystalline phase of BN materials. For h-BN, only one characteristic peak, E_{2g} mode, can be observed at ~1366 cm^{-1}.[93] In the case of c-BN, longitudinal optical (LO) and transverse optical (TO) two modes can be detected at around 1304 and 1055 cm^{-1}, respectively.[94] The situation of w-BN is complex; three characteristic peaks have been mainly reported via theoretical and experimental analysis, including E_1 (LO), E_1 (TO) and E_2 modes at around 1293, 1075, and 979 cm^{-1}, respectively.[95-96] As for a-BN, in spite of the amorphous structure, two broad peaks can be still observed in the range of 1200 – 1500 cm^{-1}, because of the coexistence of sp^2 and sp^3-bonded BNs.[8, 97]
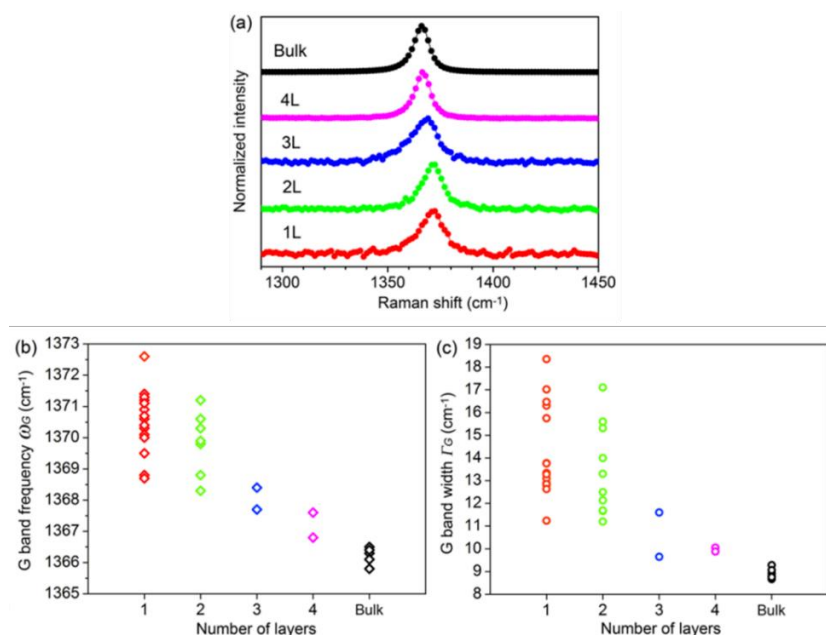
Figure 2.5 (a) Normalized Raman spectra of h-BN layers, and the corresponding E_{2g} (G) band (b) frequencies and (c) FWHM (with). Reproduced from Ref.[98] with permission of Copyright (2014) American Chemical Society.

Interesting findings are that the layer number of h-BN can influence the intensity, frequency, and width of Raman-active mode. Gorbachev et al. have found that the E_{2g} Raman band will proportionally increase in intensity when the number of BN layers increases from mono- to few-layer.[93] **Figure 2.5a** displays normalized Raman spectra

of *h*-BNNSs and their bulk counterpart, and the Raman band of 1 – 4 layered BN shows a distinct blue shift concerning the bulk crystals.[98] The band frequency is 1366.2 cm^{-1} for bulk *h*-BN, determined by the average value of six samples; and they are 1370.5, 1370.0, 1367.8, and 1367.2 cm^{-1} for mono, di, tri, and tetra-layer sheets (see **Figure 2.5b**). The upshift of E_{2g} is due to higher in-plane strain and lower interlayer interaction in few-layer BNNSs, consequently resulting in phonon softening. Meanwhile, the full width at half-maximum (FWHM) of the Raman band is also larger with the number of BN layers decreases from bulk to mono (**Figure 2.5c**).

2.2.3. X-ray photoelectron spectroscopy

X-ray photoelectron spectroscopy (XPS) is a quantitative technique for identifying the elemental composition and quantity of samples, and the binding states of corresponding elements can be analyzed by deconvoluted spectra. As seen in **Figure 2.6a**, the B and N elements can be detected at around 190.5 and 398.5 eV; other elements usually are from the presence of impurities or functionalization in BN products.[99] Sometimes the peaks of Si and C appear in the survey spectrum because of SiO_2/Si substrate or carbon tape.[36, 100] **Figure 2.6b** gives the peaks of B 1s and N 1s that can report chemical states and their ratios, such as B-O and N-H. Except for the sharp core bindings, the sp^2-bonded BN atoms usually cause two small broad peaks at around 200 and 425 eV.[101] Although the two peaks do not arise in pure *c*- or *w*-BNs, it cannot allow further distinguishing *h*-, *r*-, *t*- and *a*-BNs.
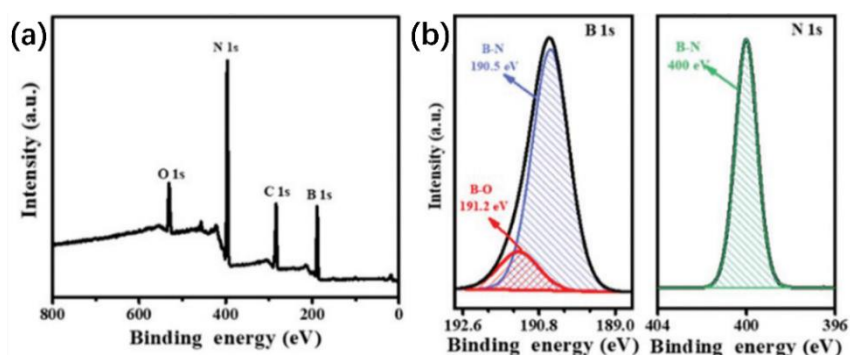
Figure 2.6 (a) XPS spectrum of hydroxyl-functionalized BNNSs, and their (b) B 1s and N 1s photoemission spectra. Reproduced from Ref.[99] with permission of Copyright (2018) The Royal Society of Chemistry.

2.2.4. X-ray diffraction

X-ray diffraction (XRD) is an analytical technique for identifying the phase of a crystalline sample and providing information on its unit cell dimensions. XRD is the primary possibility to distinguish different crystal phases of BN materials. Herein, the classic patterns of BN crystals are shown in **Figure 2.7** according to the corresponding ICDD PDF Cards. The main peak of *h*-BN is at 26.75° of (002) plane reflection, which is closed to (003) plane of *r*-BN is at 26.72°. To differentiate the two sp^2 BNs, we should still consider other peaks, for example, (100) and (102) planes at 41.61° and 50.16°of *h*-BN, (101) and (012) planes at 42.62° and 45.57°of *r*-BN.[102] The key reflection of *c*-BN is located at 43.30° corresponding to the (111) plane, and others can be deleted, such as, at 74.20° and 89.93° to (220) and (311) reflections. Three primary peaks in range of 40 – 48° are the characteristic of *w*-BN XRD, and they are 40.83°, 42.86° and 46.37° of (100), (002) and (101) planes, respectively.
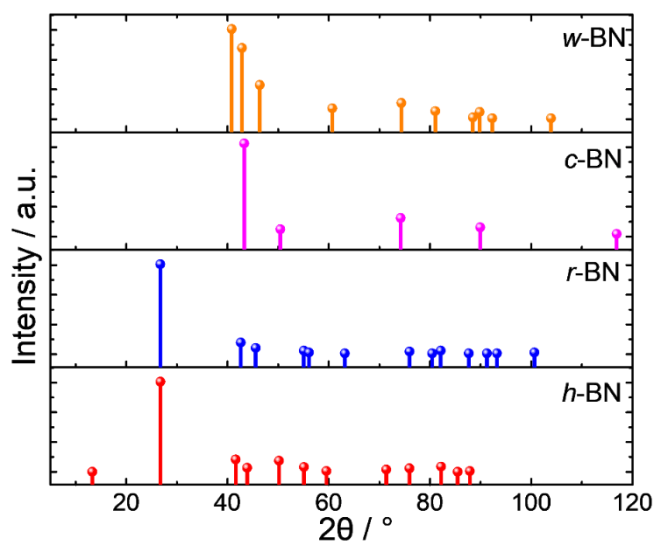
Figure 2.7 XRD patterns of *h*-, *r*-, *c*-, and *w*-BNs according to ICDD PDF Cards Nos. 01-073-2095, 00-045-1171, 00-026-0818, and 00-049-1327, respectively.

In addition to phase identification, XRD technique also allows material purity, crystallite size, and, in some cases, morphology information.[103] For example, Rietveld refinement of collected XRD spectrum can be performed based on the Lorentz equation that permits the contributions of different BN phases and the sample purity.[104-105] When bulk BNs are cut into the nanoscale, the crystallite size will decrease and the

XRD peaks consequently broaden. Then Scherrer equation can be used to quantitatively evaluate the crystallite size of BN samples via the broadening diffraction angles.

2.3. Optical measurements

This Section has concentrated on the measurements for optical properties, especially fluorescence, of BN materials.

2.3.1. Ultraviolet-Visible spectroscopy

Ultraviolet-visible (UV-Vis) spectroscopy refers to absorption, transmittance or reflectance spectroscopy. As shown in **Figure 2.8a**, a sharp and intense band can be detected in UV rang from BN sheets or thin film that is assigned to the typical band-to-band transition.[106] In another hand, poor absorption in visible region leads to its transparent feature under optical microscopy.

The Tauc equation permits a good elevation for the bandgap of the sample according to its UV-Vis absorption or transmittance spectrum.[107] In this case, the calculated gap is ~6.02 eV that agrees well with the bandgap value of 2D h-BN (**Figure 2.8b**).[106]
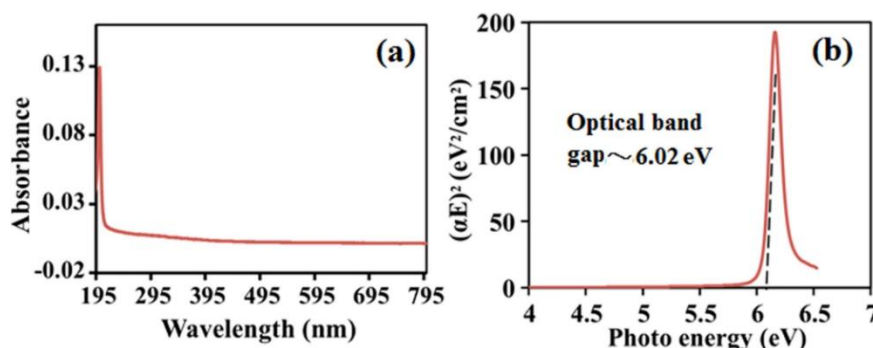
Figure 2.8 (a) UV-Vis absorption spectrum and (b) Tauc plot of h-BN film. Reproduced from Ref.[106] with permission of Copyright (2015) Springer Nature.

2.3.2. Fluorescence spectroscopy

Fluorescence spectroscopy is a kind of electromagnetic spectroscopy that analyses the fluorescence of samples. Photoluminescence spectroscopy generally referred to as PL, is the light emission from any matter after the stimulation of light energy, or photons. **Figure 2.9** shows 3D excitation-emission and 2D excitation-dependent PL spectra of BN QDs, and both can report the maximum emission as well as the corresponding best

excitation.[46] The former allows a fast and intuitive understanding; the latter displays more detailed data of a single spectrum.
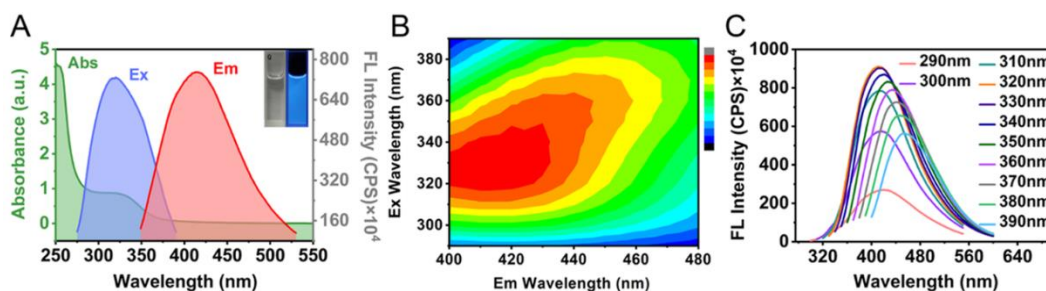
Figure 2.9 (a) UV-Vis absorption, PL emission and excitation spectra, (b) 3D excitation-emission spectra, and (c) 2D excitation-dependent PL spectra of BN QDs. Reproduced from Ref.[46] with permission of Copyright (2020) American Chemical Society.

2.3.3. Time-resolved photoluminescence spectroscopy

Fluorescence lifetime (τ) is an intrinsic characteristic of luminescent species that provides insight into the excited state dynamics. Time-resolved PL (TR-PL) is the tool of choice, under the excitation of pulsed lasers, to study the fast electronic deactivation process after the illumination of material occurs. **Figure 2.10** shows an example of the TR-PL spectrum of BN QDs, which can be well fitted via a tri-exponential function. It means that there are three types of emissive centers in this PL process.[36]
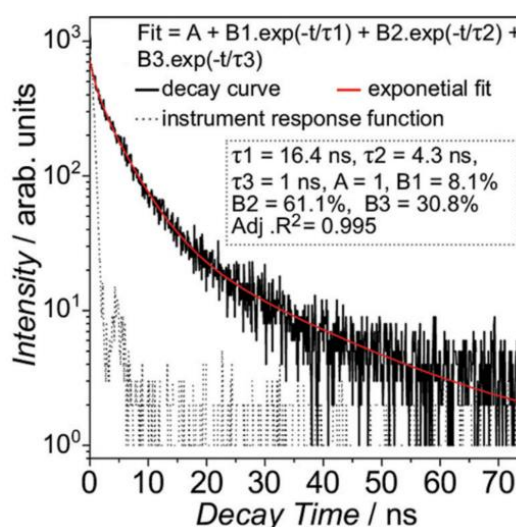
Figure 2.10 TR-PL decay profile of BN QDs. Reproduced from Ref.[36] with permission of Copyright (2013) John Wiley and Sons.

Chapter 3. Chemicals and Characterizations

In this Chapter, the chemicals used in this thesis are shown, coupled with the equipment lists of materials synthesis and characterization.

3.1. Chemicals and reagents

The solid and liquid materials, as well as organic solvents, involved in this thesis, are listed in **Tables 3.1**, **3.2**, and **3.3**, respectively. Additionally, deionized water was used in the preparation process. Silicon wafer and silica glass were used for measurements of films.

Table 3.1 The solid chemicals for experiments.

Name	CAS Number	Purity and Producers
Boric acid (H_3BO_3)	10043-35-3	99.5%, Carlo Erba
Hexagonal boron nitride (*h*-BN)	10043-11-5	99.5%, Alfa Asear
Sodium hydroxide (NaOH)	1310-73-2	96%, Wako
Potassium bromide (KBr)	7758-02-3	IR, 99%, Sigma-Aldrich
Pluronic F-127	9003-11-6	~12600 g mol^{-1}, Aldrich
Stearic acid	57-11-4	97%, Sigma-Aldrich

Table 3.2 The liquid chemicals for experiments.

Name	CAS Number	Purity and Producers
Ammonium hydroxide solution ($NH_3 \cdot H_2O$)	1336-21-6	30-33% NH_3 in H_2O, Sigma-Aldrich
Methyltriethoxysilane (MTES)	2031-67-6	98%, Abcr
Tetraethoxysilane (TEOS)	78-10-4	99%, Abcr
Hydrochloric acid (HCl)	7647-01-0	37% HCl in H_2O, Sigma-Aldrich
Orthophosphoric acid (H_3PO_4)	7664-38-2	85% H_3PO_4 in H_2O, Fluka
Titanium (IV) chloride ($TiCl_4$)	7550-45-0	99.9%, Aldrich

Table 3.3 The organic solvents for experiments.

Name	CAS Number	Purity and Producer
Ethanol (EtOH)	64-17-5	99.8%, Carlo Erba
N,N-Dimethylformamide (DMF)	68-12-2	99%, Sigma
Dimethyl sulfoxide (DMSO)	67-68-5	99.9%, Sigma
N-Methyl-2-pyrrolidone (NMP)	872-50-4	99.5%, Supelco

3.2. Equipment for the preparation and treatment of materials

Here is the equipment list used for the preparation of materials in this thesis in **Table 3.4**.

Table 3.4 The equipment list of materials synthesis in this thesis.

Name	Manufacturer
Analytical balance	CRYSTAL 100 CAL CE - Gibertini Elettronica
Sonicator	CEIA CP102 Ultrasonic Cleaner - 2.5 L
High-temperature furnace	Neytech Vulcan Model 3-550 Multi-Stage Programmable Furnace
Dip coater	KSV NIMA Dip Coater
Spin coater	Specialty Coating Systems G3P-8 Spin Coater
Centrifuge	NEYA 16 Lab Centrifuge
Laboratory water purification system	Millipore PE Tank with Automatic Sanitization Module 100 Liter
Handheld UV lamp (254 and 365 nm)	Spectronics Model ENF-280C/FE

3.3. Characterizations

3.3.1. Characterizations for structure and composition of materials

Transmission electron microscopy (TEM) images were captured by using an "FEI Tecnai 200" microscope (Thermo Fisher Scientific, USA) working with a field emission electron gun and operated at 200 kV. High-resolution (HR) TEM images were collected by a "JEM 2010" microscope (JEOL, Japan).

Atomic force microscopy (AFM) measurements were performed with a "Ntegra"

microscope (NT-MDT, Russia) in a semicontact mode with a scan speed of 0.8 Hz, equipped with a silicon tip with a nominal resonance frequency of 150 kHz, 5 N m^{-1} force constant, and 10 nm typical curvature radius.

Dynamic light scattering (DLS) curves were recorded using an "LB-550" nanoparticle size analyzer (Horiba, USA) to calculate hydrodynamic diameters of nanomaterials.

Fourier-transform infrared spectroscopy (FTIR) measurements were carried out by an "infrared Vertex 70v" interferometer (Bruker, Germany) with the range from 4000 cm^{-1} to 400 cm^{-1} and a 4 cm^{-1} resolution. The solid power-state samples were tested by putting them in KBr pieces, and the films were analyzed on silicon wafer as substrate. Under the assist of an electrical heating jacket (Specac, UK) as a temperature controller, *in situ* FTIR spectra were recorded in the range from 25 to 250 °C. Combined with an A225/Q Platinum attachment (Bruker, Germany), the IR spectra of samples in liquid-state were collected by the attenuated total reflection (ATR) technique.

Raman spectroscopy was obtained by a "Senterra" microscope (Bruker, Germany) in the range of 1555 – 65 cm^{-1}. The spectra were recorded under an excitation wavelength of 532 nm (0.5 mW), 633 nm (0.2 mW), or 785 nm (1.0 mW) laser, using a 3~5 cm^{-1} resolution and a 10 s integration time.

Thermal gravimetric analysis (TGA) was tested by an "SDT-Q600" instrument (TA Instruments, USA), which was operated from 25 to 800 °C with a ramp rate of 5 °C min^{-1} under nitrogen gas flow of 20 mL min^{-1}.

X-ray photoelectron spectroscopy (XPS) tests were performed at room temperature condition by a "custom-designed ultra-high vacuum (UHV)" equipment with an Omicron electron analyzer. The test was carried out at a 10^{-10} mbar pressure using a dual non-monochromatized Al K$_\alpha$ X-ray source (1486.6 eV). The collected parameters were set as 0.1 eV step, 0.5 s collection time, and 20 eV pass energy, respectively.

X-ray powder diffraction (XRD) analysis was captured by a "Rigaku D/Max-B" diffractometer with a Cu K$_\alpha$ radiation (1.54056 Å) and a monochromator in the diffracted beam. The spectra were collected under the condition of a 0.05° step-scan and 15 s counting-time per point.

3.3.2. Characterizations for functional properties of materials

UV-Vis absorption and transmission spectra were recorded by using a "Nicolet Evolution 300" spectrophotometer (Thermo Fisher Scientific, USA) from 190 to 900 nm with a 1.5 nm bandwidth.

Fluorescence spectra, including 2D and 3D spectroscopy, were measured by a "Fluoromax-3" spectrofluorometer (Horiba Jobin Yvon, Japan).

Absolute fluorescent quantum yields (QYs) were obtained using a "NanoLog" spectrofluorometer (Horiba Jobin Yvon, Japan) equipped with a "quanta-ϕ" integrating sphere accessory. The calculations were processed through "FluorEssence V3.9" software. Here, the same instrument was also used to capture the fluorescence lifetime curves with the NanoLED-270, 340 and 405L, respectively, as the excitation light sources ($\lambda = 266$ nm, pulse duration < 1.2 ns; $\lambda = 340$ nm, pulse duration < 1.2 ns; and $\lambda = 405$ nm, pulse duration < 200 ps). A "DataStarion" software was used to record the time-resolved fluorescence curves, then a "DAS6 Analysis" software was used to fit the recorded data.

Time-resolved luminescence curves were collected by using long pulses of 200 fs as the excitation light of the samples. The laser pulses were delivered from an optical parametric amplifier (Light Conversion TOPAS-C, Lithuania) pumped under a regenerative Ti: sapphire amplifier (Coherent Libra HE, USA) with a frequency of 1 kHz. The fluorescent signals were recorded by a streak camera (Hamamatsu C10910, Japan) with the equipment of a grating spectrometer (Princeton Instruments Acton SpectraProSP-2300, USA).

A spectroscopic ellipsometer (α-Woollam, USA) with a fixed angle geometry was used for the measurements of the thickness and refractive index of hybrid films. The experimental data were evaluated and fitted based on a Cauchy model in the case of silicon wafer supported the transparent film.

Chapter 4. Boron Nitride Nanosheets

Chapter 4 can be divided into the following two parts, Sections 4.1 and 4.2:

In Section 4.1, we have mainly explored the assistance of defects on the photoluminescence (PL) properties of hexagonal boron nitride nanosheets (*h*-BNNSs). Firstly, it is found that the obtained *h*-BNNSs possess -OH species when sonication-assisted exfoliation of the bulk counterpart is carried out in the water phase. The as-prepared defective few-layer nanosheets show a weak fluorescence in the visible region with a peak at ~400 nm. Tailored defects can be further introduced by thermal oxidation in the air atmosphere, which also lead to the change of emission in intensity. Moreover, the results of quantum chemical calculations can verify the experimental results. Besides, when water was replaced by dimethyl sulfoxide (DMSO) and N-methyl-2-pyrrolidone (NMP), defect-free *h*-BNNSs can be obtained, which show non-fluorescence.

In Section 4.2, we have mainly investigated the structure and properties, especially the photocatalytic effect, of BN-titania heterostructures. The heterostructures have been fabricated by incorporating two types of BN sheets, respectively with and without defects, into titania mesoporous films to explore the functions of BN defects on heterojunction features. It has been found that the BNNSs are optically transparent without any intrinsic photocatalytic response, but contribute to the anatase crystallization via heterogeneous nucleation effect. The defective BNNSs can promote the photocatalytic effect of TiO_2 because of improved crystallization and optical absorption.

4.1. Defect-assisted luminescence in boron nitride nanosheets

This Section is summarized according to the following article: **Junkai Ren**, Luigi Stagi*, Carlo Maria Carbonaro, Luca Malfatti, Maria Francesca Casula, Pier Carlo Ricci, Antonio Del Rio, Francesco Bonaccorso, Laura Calvillo, Gaetano Granozzi, and Plinio Innocenzi*. Defect-assisted photoluminescence in hexagonal boron nitride nanosheets. *2D Mater.*, **2020**, 7, 045023.

Various contents and figures in this Section are reproduced with permission of Ref.[22], Copyright (2020) IOP Publishing Ltd.
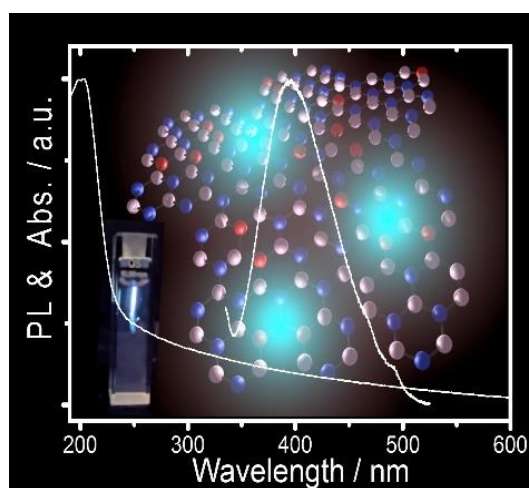
4.1.1. Introduction

Since the discovery of graphene, hexagonal boron nitride (*h*-BN) has been the focus of interest in 2D materials areas. The wide bandgap values of ~6 eV including both direct and indirect gaps have been theoretically and experimentally confirmed, which have endowed *h*-BN with valuable applications in photonics and optoelectronics.[3, 108-109] Apart from the excellent ultraviolet luminescence for DUV LED and laser applications,[109] researchers have also paid their interest in room temperature photoluminescence (PL) in the visible region from *h*-BN materials, for example, the fluorescent 0D nanodots and 2D nanosheets.[13, 110] The presence of carbon, oxygen, and hydrogen impurities generally has resulted in the formation of multiple defects in

the BN structure. The visible PL properties have been largely attributed to the possible defect emissive centers including boron or nitrogen vacancies, carbene structure, and oxygen-doping.[36] However, it is still difficult to make a comprehension of BN emissions because of the simultaneous presence of multiple impurities or heterogeneous distribution of various defect states.

Fluorescent *h*-BN nanosheets (*h*-BNNSs) can be obtained by both top-down and bottom-up routes. Some carbon and/or oxygen impurities are usually unavoidable in the produced 2D BN via bottom-up methods, which mainly depend on the precursors and the synthesis conditions.[111] Particularly, the vacancies of boron and nitrogen are the most common existence in the BN layers, and it is impossible to completely avoid these vacancies. As for top-down approaches, ultrasonication-assisted liquid-phase exfoliation is one of the most straightforward routes to allow producing few-layer *h*-BNNSs, for example, a selection of water as the liquid phase. Although it is a relatively controlled preparation, some structural defects are still formed in the processing. In detail, the ultrasonic waves can drive the final exfoliation of layered materials mainly by explosion and implosion of generated microbubbles, which is known as cavitation.[112-113] The cavitation can not only stimulate the exfoliated process by changing the pressure, temperature, and shear force, but also induce the formation of more structural vacancies, edge defects, and hydroxyl species (e.g. B-OH).[114-115]

A defect-free *h*-BN system cannot show emission in the visible region, while the BNs with defective structures display emerging visible fluorescence. Some theoretical models have been put forward to build a good correlation between the emissive properties and the defect types.[116-118] However, it still lacks a comprehensive understanding of the experimental observation of the wide intragap emission in 2D *h*-BN.

In this Section, we have tailored oxygen-defects in liquid-phase exfoliated *h*-BNNSs via a top-down sonication-assisted method. A relationship is established between the optical features and defects according to the experimental data as a function of a series of thermal treatments in air, as well as the corresponding supports by quantum chemical calculations.

4.1.2. Experimental section

4.1.2.1. Preparation of *h*-BNNSs with defects

The nanosheets were prepared through a water-assisted liquid exfoliation, as shown in **Scheme 4.1.1**. Briefly, 20 mg *h*-BN bulk powders were dispersed in 20 mL H_2O, then sealed in a 25 mL glass bottle. After 15 h ultrasonic treatment, the dispersions were centrifuged at 8000 rpm for 10 min to collect the supernatant containing *h*-BNNS products.

The liquid was used for optical measurements, including fluorescence and UV-Vis absorption. The dried powers could be obtained by volatilizing the water, which was further used for the characterization (i.e., FTIR, XPS) and the next oxidation thermal treatments (in air for 1 hour under 100, 300, 500, and 700 °C, respectively).
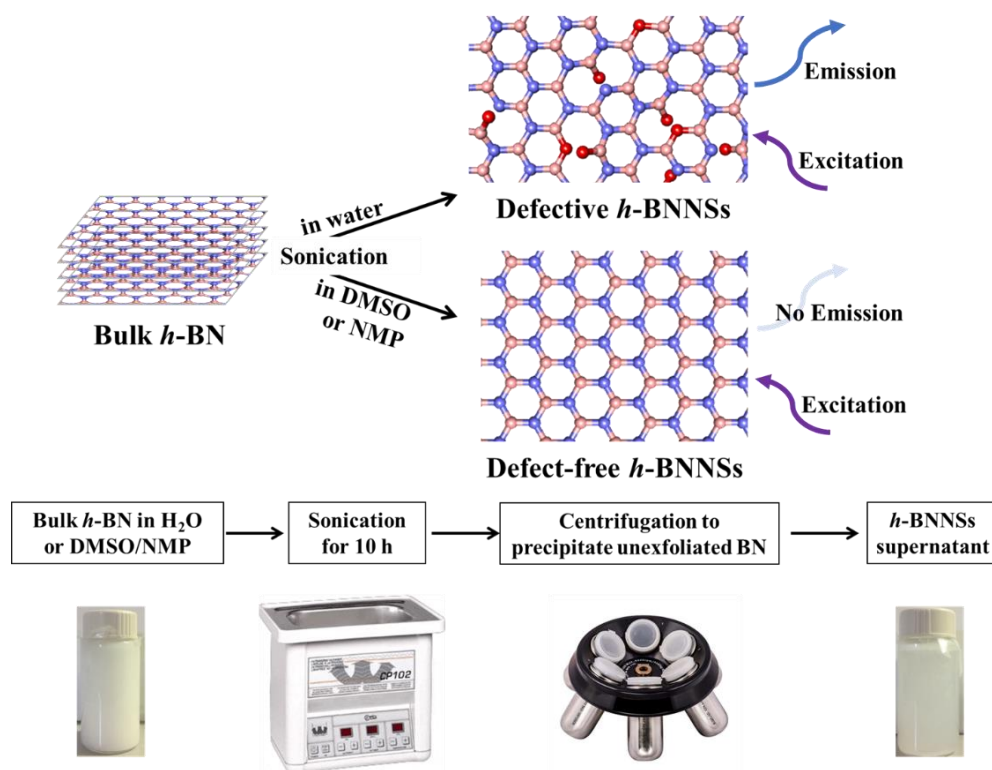
Scheme 4.1.1 Schematic illustration for the preparation of *h*-BNNSs with or without defects.

4.1.2.2. Preparation of *h*-BNNSs without defects

A similar method was performed to prepare another kind of *h*-BNNSs derived in DMSO or NMP. H_2O was substituted by DMSO or NMP. After 15 h ultrasonic

treatment, the dispersions were centrifuged at 5000 rpm for 10 min to collect the supernatant containing *h*-BNNS products.

4.1.2.3. Quantum chemical calculations

Density functional theory (DFT) combined with a cluster-based method was used for the investigation of the relationship between optical and structural features of *h*-BN monolayer. Firstly, the BN clusters with different sizes were used for the calculations of defect-free models. Then some possible defects were implanted for the analysis of defective systems, such as B/N vacancies and O doping.

These theoretical calculations were performed using Gaussian 16 code,[119] while the energy calculations were run within DFT based on Becke's three parameters and Lee-Yang-Parr's nonlocal correlation functions.[120] A 6-31 G(d, p) was used for the sets of B, N, O, and H atoms. Time-dependent (TD)-DFT route was used for the calculations of electronic excitation energy. GaussView 6 was used for interpreting the computed results.[121]

4.1.3. Results and discussion

4.1.3.1. Morphology and structure

The water-derived *h*-BNNSs show the fluorescence in the visible region because of the presence of hydroxyl species and oxygen-related defects. On the contrary, the DMSO or NMP-derived sheets are defect-free and cannot exhibit visible emission. Therefore, a series of measurements have been used to explore the corrections of optical and structural properties.

The morphology of the *h*-BNNSs exfoliated in water phase is presented by both TEM and HRTEM images. **Figure 4.1.1a** shows that the lateral sizes of the fresh nanosheets are in the range of hundreds of nanometers. High-temperature treatment does not cause an obvious change in their morphology (e.g. 300 and 700 °C in **Figure 4.1.1b-c**). The HRTEM images in **Figure 4.1.1d-h** describe the crystalline structure of the as-prepared BNNSs, in which the interplanar distances accord well with *h*-BN configuration (JCPDS-ICDD PDF Card 34-421).[79] The crystallinity is not affected by thermal

treatments (**Figure 4.1.1j-k**), suggesting that the hexagonal structure of *h*-BNNSs is still stable under this temperature range.
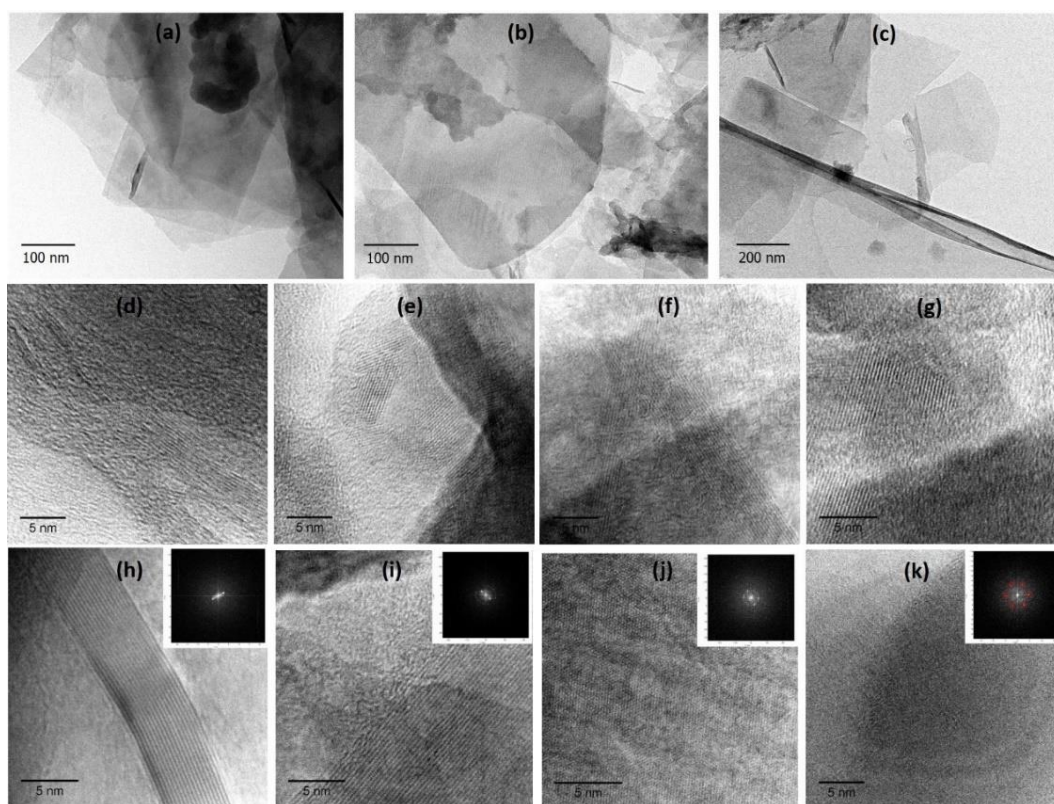

Figure 4.1.1 TEM and HR-TEM images of (a, d-h) the as-prepared h-BNNSs, and after treating at (b, j) 300 °C and (c, k) 700 °C, as well as the corresponding inset of FFT. The red circles of (k) inset highlight the hexagonal symmetry.
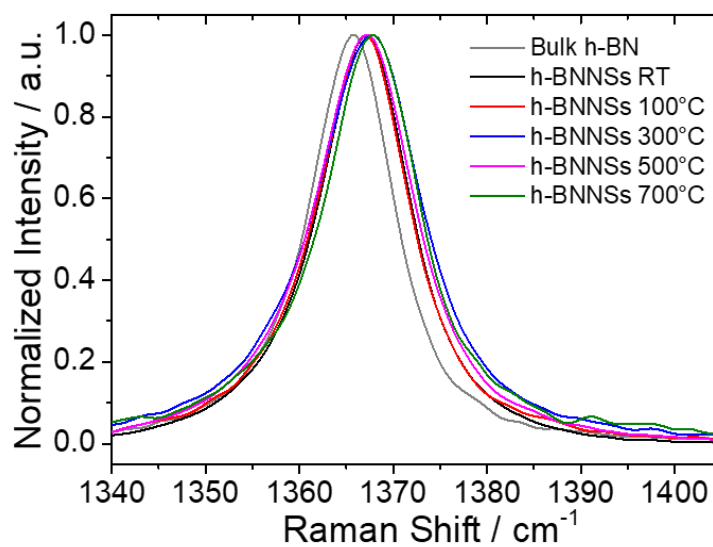

Figure 4.1.2 Raman spectra in the range of 1340 – 1405 cm^{-1} from bulk *h*-BN as well as *h*-BNNSs before and after thermally treating.

The Raman spectra of the samples in **Figure 4.1.2** have been collected to explore the impact of ultrasonication on BN nanostructure. As a reference, the bulk *h*-BN is characterized by a peak at 1365.5 cm^{-1}, which is attributed to the E_{2g} vibrational mode (generally termed as G band). The G band is detected at ~1367.0 cm^{-1} in the exfoliated BNNSs, meaning that the obtained flakes are few-layered in thickness.[93, 98] Meanwhile, the shape of the band shows slightly wider than the bulk counterpart, and then becomes wider after thermal treating. It can be assigned to the results of oxidation.

FTIR measurement has been further performed to the present groups or structural defects from the nanosheets. **Figure 4.1.3** shows the infrared spectra in absorption modus, which has been divided into five parts in the light of the detected signals. The region I of ~3800 – 2850 cm^{-1} clearly represents the -OH stretching mode, which is presented by a broad band. This -OH band can be further subdivided into two overlapped species at 3240 and 3450 cm^{-1}, respectively.[122] The component at lower wavenumbers is originated from the absorbed water, and the one in the higher region is classified as the B-OH groups. Overall, the intensity of this area shows a decreasing trend after thermal treatments in air.

In the regions of II and IV, the peaks at 1375 and 815 cm^{-1} are typically corresponding to the in-plane B-N stretching and the out-of-plane B-N-B bending vibrations, respectively. The heating process does not cause a shift of those two models. As for region III of 1185 – 845 cm^{-1}, it can be assigned to the oxidization of BN into N-B-O groups.[59] Because of the oxidized results in air, the band increases in intensity with the rise of thermal temperature.

The infrared alterations show a possible trend of defect-structural changes in BNNSs upon the subsequent thermal treatments. It is strong conjunction that the intensity of B-OH goes down, while that of N-B-O goes up with the rise of temperature. In this case, it concludes that B-OH sepsis tends to be oxidized into N-B-O defects. When the temperature increases to 500 and 700 °C, a band in region V newly appears at ~460 cm^{-1}. It is due to the formation of O-B-O bands, indicating that N-B-O groups are further oxidized into the resulting boroxyl tings.
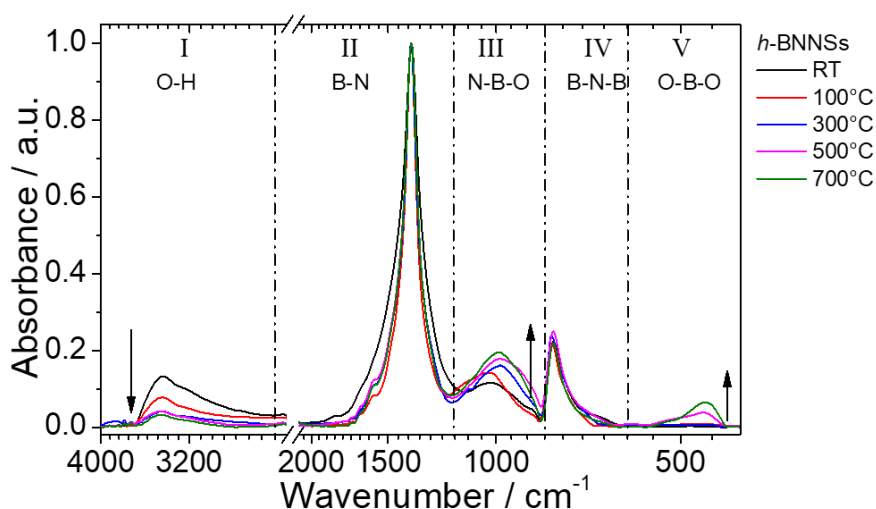
Figure 4.1.3 Normalized FTIR spectra of the *h*-BNNSs before and after thermally treating. The inserted arrows show the intensity change (up: increase; down: decrease) as a function of heating temperature.

Furthermore, the information of O-H groups in region I has been detailly studied using *in situ* heating approach until a temperature of 250 °C (see **Figure 4.1.4**). Based on Gaussian fitting, the overlapped spectra can be deconvoluted into two components of absorbed water and B-OH (in agreement with **Figure 4.1.3**). The B-OH peak at 3450 cm^{-1} shifts to a higher wavenumber, suggesting the hydrogen bonds decline in content. Then the B-OH groups are possible in an isolated or twin state after thermal treating. The absorbed water centered at 3240 cm^{-1} also decreases in intensity as heating progresses. When thermal treatment is up to 200 and 250 °C, the intensity of O-H band is negligible in detection.

In **Figure 4.1.5**, TGA-DTA data have been analyzed by coupling with the *in situ* FTIR spectra as a function of temperature. The DTA from the heat flow curve describes three endothermic cases. The first one is a drying process with ~0.80% weight loss from 25 to 95 °C, which is due to the lost adsorbed water. Then the second step continues to show a 1.34% loss in weight, because of intercalated water, during the temperature range of 95 to 135 °C. The third process happens from 135 to 300 °C with ~1.04% weight loss associated with the condensation of B-OH groups. The FTIR-TGA joint data suggest that it can produce a kind of change in structure as a result of the condensed B-OH when the thermal treatment is performed with a temperature below 300 °C.

Subsequently, a higher temperature than 300 °C can initiate oxidation and another structural change, finally leading to the formation of boron-oxygen rings.
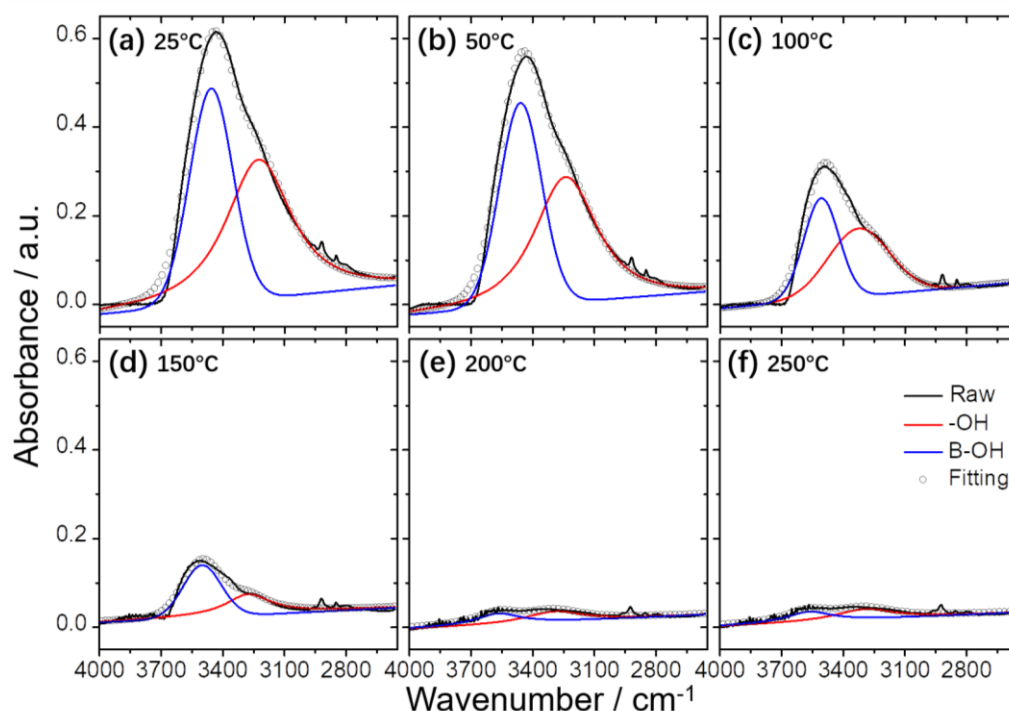
Figure 4.1.4 *In situ* FTIR spectra in the range of 4000 – 2400 cm^{-1} of the as-obtained *h*-BNNSs as the function of temperature from 25 to 250 °C.
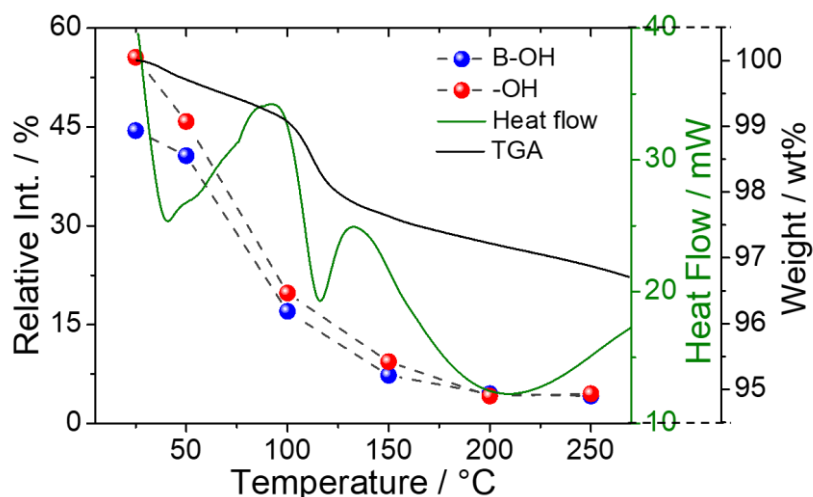
Figure 4.1.5 The relative intensity of two components of *in situ* infrared spectra, accompanied by TGA and heat flow curves, as a function of increasing temperature.

XPS measurement has also been used to investigate the chemical compositions of these samples. The estimated atomic percentages are listed in **Table 4.1.1**, where the

relevant sensitive factors are also taken into consideration. It should be noted that a small number of carbon atoms have been detected in the testing process, which are mainly associated with adventitious carbon. Firstly, the ratio of B: N is in good agreement between the bulk *h*-BN crystals and the as-prepared exfoliated sheets, which points out a small overdose of N to B atoms and the presence of O atoms. It is as expected that the thermal treating can bring about a rise of O element in amount. A change of B: N ratios is further clearly detected when the materials are heated at 500 and 700 °C.

Table 4.1.1 Chemical composition (at.%) of the samples determined by XPS.

Sample	B	N	C	O	B: N ratio
h-BN bulk	42.8	46.3	3.1	7.8	1 : 1.08
h-BNNSs RT	42.6	44.2	2.8	10.4	1 : 1.04
h-BNNSs 300 °C	37.9	41.0	3.6	17.5	1 : 1.08
h-BNNSs 500 °C	35.0	51.4	2.0	11.6	1 : 1.47
h-BNNSs 700 °C	29.9	50.8	3.5	15.8	1 : 1.70

4.1.3.2. Optical properties

The optical properties of the water-derived *h*-BNNSs have been studied by UV-Vis absorption, fluorescence, lifetime, etc. They are also compared with the NMP and DMSO-derived sheets in aspects of PL and IR.

Figure 4.1.6a presents the UV-Vis absorption spectra of the *h*-BNNSs and the samples after heating at different temperatures. In the UV region, the spectra show a strong band centered at ~206 nm, which is assigned to the direct band-gap transition of *h*-BN materials. It is clearly seen that the heating oxidation can increase the intensity of the broad absorption from the UV tail continuously to the visible region. Subsequently, the corresponding bandgap E_g can be assessed by the Tauc equation according to the UV-Vis data (see **Figure 4.1.5b** and **Supplementary Note I**). The E_g value decreases from 5.62 to 5.02 eV with the increase of heating temperature, which is in correction with the increased oxygen amount in the *h*-BNNSs.
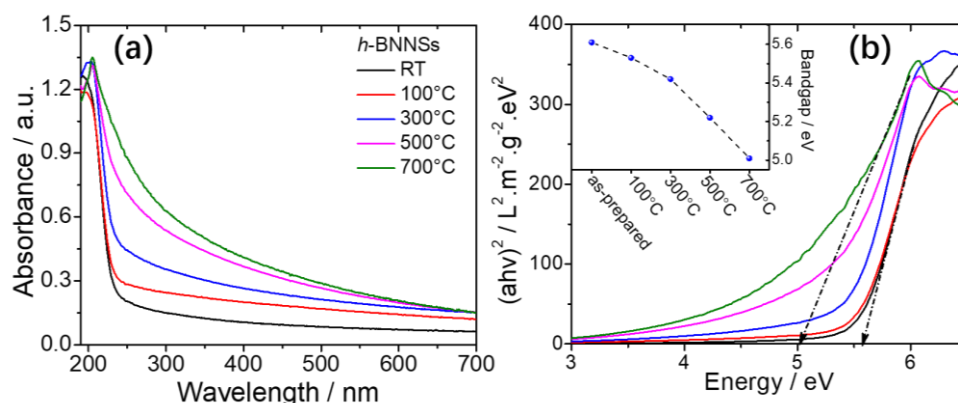
Figure 4.1.6 (a) UV-Vis absorption spectra of the as-prepared *h*-BNNSs and treated sheets at different temperatures (measured in aqueous solution), (b) the corresponding evaluations of E_g in these samples by Tauc method, inset showing the calculated values.
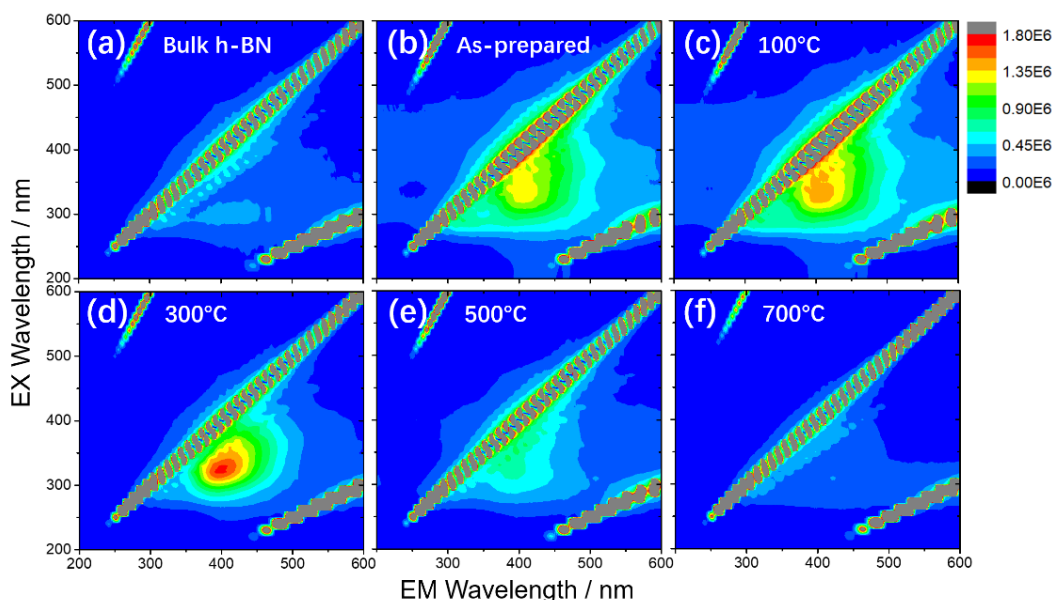
Figure 4.1.7 3D excitation-emission-intensity fluorescent spectra of the samples in aqueous solution. The gray regions are due to the 1st and 2nd order artefacts.

Figure 4.1.7 describes the fluorescent spectra of the samples in water solution by a 3D excitation-emission intensity map. Here the PL spectrum in *h*-BN bulk crystal is given in **Figure 4.1.7a** as a reference, which shows a negligible emission within the detection limit. Meanwhile, the as-obtained *h*-BNNSs (**Figure 4.1.7b**) present an emission in visible blue region with the maxima peaking at ~405 nm under excited light of ~325 nm. After treating at 100 and 300 °C, the PL intensity of the samples increases from $4.5 * 10^5$ to $5.0 * 10^5$ and $9.0 * 10^5$ counts (see **Figure 4.1.7c-d**). As shown in

FTIR data, the N-B-O bands also increase in the range, indicating the hypothesis that N-B-O defects in *h*-BN structure are corrected with the improvement of fluorescence. Then the luminescence goes down after treating at higher temperatures (e.g. 500 and 700 °C), because that high temperature can promote the transformation of defect-structure from N-B-O to O-B-O oxygen-containing defects.

To prove the significance of the present defects produced during the sonication process in water phase, the defect-free *h*-BNNSs prepared in NMP or DMSO solution are investigated as a comparison. As shown in **Figure 4.1.7a**, the FTIR spectra of the pristine *h*-BNNSs before and after treating at 300 °C do not show any detectable infrared bonds of oxygen-related groups, such as O-H, N-B-O, or O-B-O. Therefore, the corresponding samples show no obvious emission even after thermal treating (**Figure 4.1.7b-c**). The results once again prove the importance of N-B-O defects on the origin of luminescence in 2D *h*-BN structure.
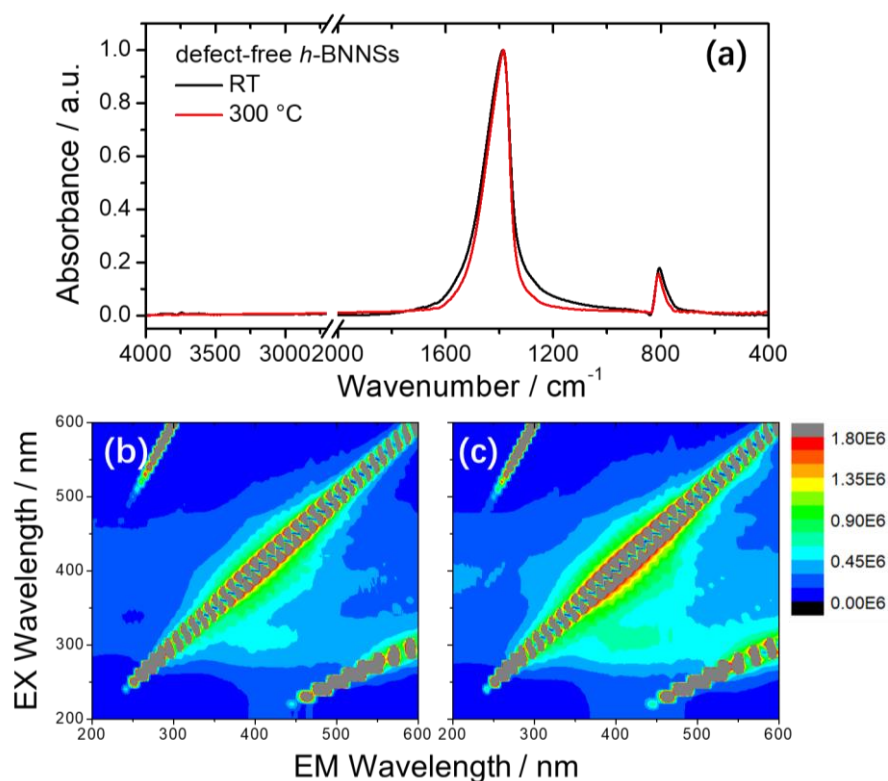
Figure 4.1.8 The properties of defect-free *h*-BNNSs derived by NMP or DMSO. (a) FTIR spectra of the *h*-BNNSs before and after thermal treatment, (b) PL spectrum of the as-prepared one, (c) PL spectrum of the sample treated at 300 °C.

Figure 4.1.9 shows the time-resolved PL curves of the samples under excitation of 300 nm. From the nanosheets treated at different temperatures, all these spectra can be well fitted by a double-exponential function. The PL decays are exhibited by two lifetimes of ~ 2 ns and ~ 10 ns, and there are no detectable variations from different samples. The similar lifetime values mean that the fluorescent response of these *h*-BNNSs is from the same type of defective structures. It can agree that the thermal treatments can contribute to the contents of emissive defects, therefore it only affects the steady-state emission in intensity.
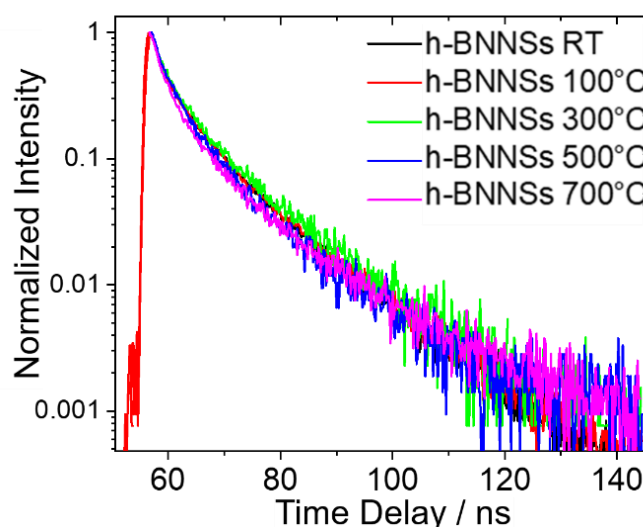
Figure 4.1.9 The time-resolved luminescent curves of the as-obtained *h*-BNNSs and the samples treated at different temperatures.

4.1.3.3. Theoretical calculations

For a deeper understanding of the role of defects in optical properties from *h*-BNNSs, theoretical calculations based on DFT have been carried out on BN clusters with different sizes and defects. Then their relevant absorption properties are reported. In the beginning, four clusters have been selected for the evaluation with different numbers of BN rings, including 7, 19, 37, and 61, representing an increasing size. Meanwhile, H atoms have been exploited to terminate their edge. As shown in **Table 4.1.2**, all the presented structures are the minimum energy configurations. Here, the cluster of 19 rings is considered as the optimal compromise that shows a good agreement with the experimental absorption.

Many investigations have reported that the direct bandgap of bulk h-BN crystals is ~6.0 eV, whilst that of their monolayer is ~5.95 eV. In our experiments, the calculated bandgap values by the Tauc method are reflected as an indirect one resulted from the absorption data. Compared with the reported results in publications, the bandgap of ours shifts to a lower value, because the defects are introduced in the ultrasonic process and the subsequent thermal oxidation. Therefore, the following calculations have been continued by considering some primary defects, such as. B/N vacancies and O impurities.

Table 4.1.2 Absorption edge as a function of cluster size.

Number of BN Rings	$\Delta E_{HOMO\text{-}LUMO}$ (Ha)	Absorption spectrum
7	0.2544	
19	0.2417	
37	0.2355	
61	0.2313	

There are two optical transitions at 6.02 and 6.26 eV (206 nm, f = 0.33; and 198 nm, f = 0.39) in the defect-free BN cluster (19 rings, $B_{27}N_{27}H_{18}$, in Table 4.1.2). Then a

supercell method is used for the calculations of the corresponding defect formation energies, where are implanted by a previous case,[123] according to the equation:

$$E_{form} = E_D(q) - E_{BN} + n_i\mu_i + q(E_{VBM} + E_F)$$ **Equ. 4.1.1**

where $E_D(q)$ is the energy of charge state q in the defective cluster, E_{BN} is the energy in the pristine BN cluster, n_i is the number of exchanged species, and μ_i is the chemical potential for the related reservoir. E_F represents the Fermi energy, E_{VBM} referring to the maximum of the valence band, which reflects the highest-occupied molecular orbital (HOMO) state in this work.
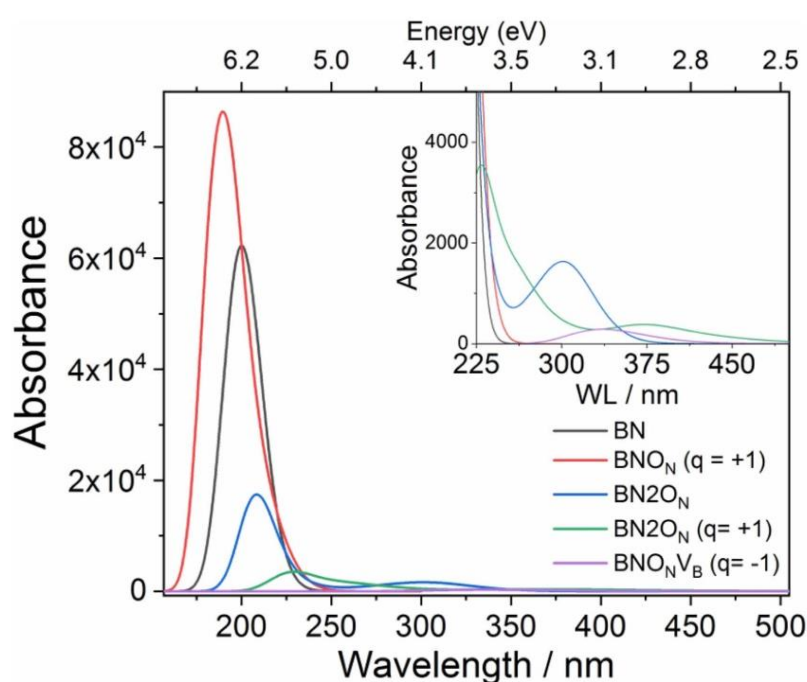
Figure 4.1.10 The theoretical UV-Vis absorption of the h-BN clusters, including the pristine and different defective types. Inset shows the enlarged range in 250 – 500 nm.

Some typical defects presented in structure of bulk and nano *h*-BN have been taken into account for the calculations of their absorption bands, including V_B and V_N (B and N vacancies), O_N and O_{2N} (one or two O atoms on N sites), and O_NV_B (O inclusion on N site near a B vacancy), respectively. **Figure 4.1.10** summarizes the computed absorption spectra of the mentioned defects in *h*-BN systems, which suggests that the O incorporations can lead to a red-shift of band-to-band absorption. Meanwhile, **Table 4.1.3** reports the corresponding energy gaps of HOMO-LUMO with different types of defects. Considering that the formation energy highly depends on the electronic states

of the defects, the influences of charged defects on the optical properties have also been detailly examined as reported in **Table 4.1.4**.

Table 4.1.3 HOMO and $\Delta E_{HOMO\text{-}LUMO}$ values in the defective h-BN clusters.

Structure /q	E_{HOMO} (eV)	$\Delta E_{HOMO\text{-}LUMO}$ (eV)
BN	-6.53	6.58
BNO_N/+1	-9.10	5.96
$BN2O_N$/0	-4.97	4.77
$BN2O_N$/+1	-6.92	3.73
$BN2O_NV_B$/-1	-1.01	3.17

Table 4.1.4 Simulations of the UV-Vis absorption situations in the defective h-BN clusters.

Defect	q	$\Delta E_{HOMO\text{-}LUMO}$ (Ha)	E_{HOMO} (Ha)	Absorption spectrum
V_B	0	0.09031	-0.24006	
V_B	-1	0.05088	-0.07138	
V_B	-2	0.05658	-0.06592	
V_N	+1	0.16635	-0.33554	

V_N	0	0.11215	-0.11448	
V_N	-1	0.12358	-0.03551	
O_N	+1	0.2189	-0.33459	
O_N	0	0.0328	-0.03724	
O_N	-1	0.01808	-0.07620	
$O_N V_B$	0	0.20264	-0.22690	
$O_N V_B$	-1	0.16311	-0.08043	

2O$_N$	+1	0.13722	-0.25444	
2O$_N$	0	0.17525	-0.18266	
2O$_N$	-1	0.01318	-0.06499	
2O$_N$V$_B$	+1	0.01575	-0.33092	
2O$_N$V$_B$	0	0.24269	-0.24286	
2O$_N$V$_B$	-1	0.11662	-0.03725	

Table 4.1.5 Representations of HOMO and LUMO in the defective *h*-BN clusters.
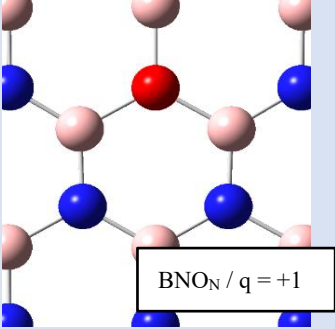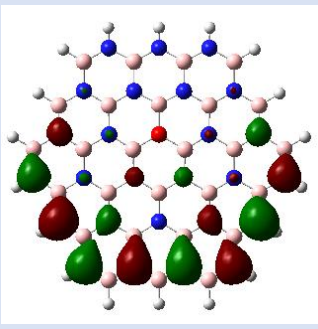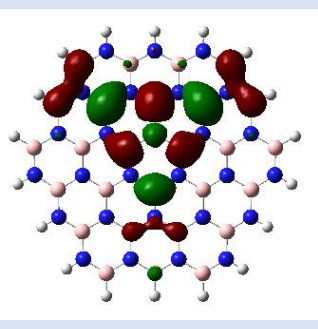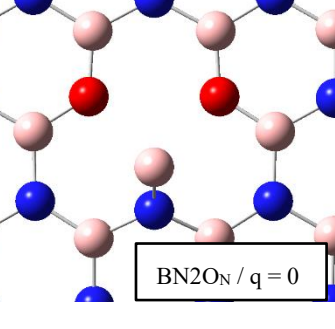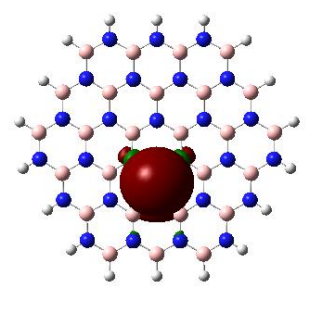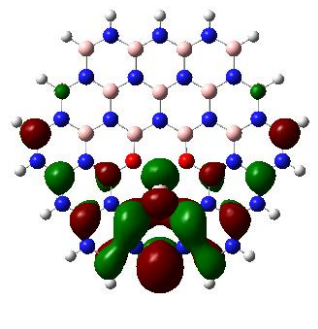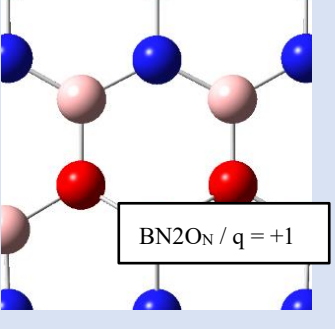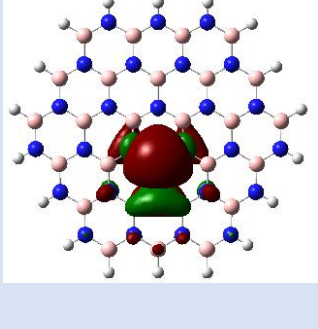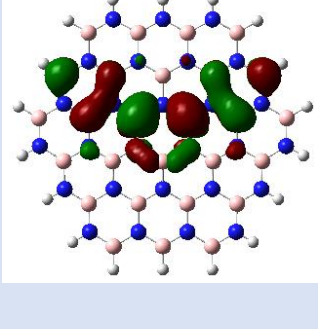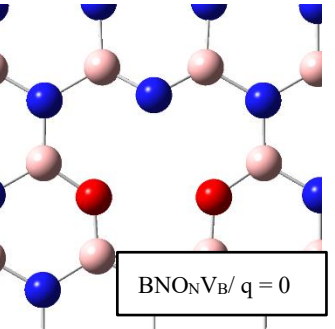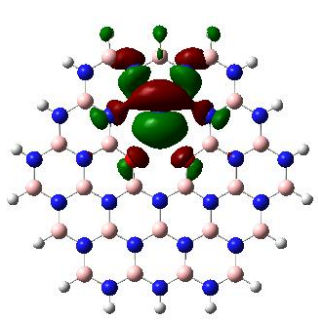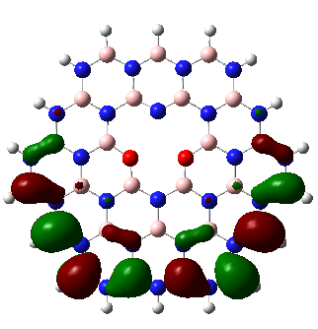
Defect / Charge	HOMO	LUMO
BNO_N / q = +1		
$BN2O_N$ / q = 0		
$BN2O_N$ / q = +1		
BNO_NV_B/ q = 0		

Table 4.1.5 has reported the optimized geometry of representations of HOMO and LUMO in the computed defective *h*-BN clusters. It proves that these point-defects will undergo different transition mechanisms under excitations, which mainly depends on their typologies and charges. For instance, the charged (q = +1) O impurities (OB$_3$) can play the role of withdrawing sites in the HOMO-to-LUMO process, whilst the 2O$_N$ and O$_N$V$_B$ defects can act as the recombination centers.

In fact, it is still different to point out the accurate impacts of O defects in *h*-BN clusters by chemical calculations. Here, at least, we have found that the presence of specific defects and charges endows BNNSs with a meaningful modulation of energy level, which conversely is in charge of the UV-Vis absorption performances after thermal treatments.

4.1.4. Conclusions

The liquid-phase assisted exfoliation by sonication in water can allow producing a kind of defective nanosheets from the bulk *h*-BN crystals. The *h*-BNNSs with defects have shown a broadly visible luminescence centered at ~405 nm. The following thermal treatment in air has further caused changes in structural defects, which can increase or decrease the fluorescent intensity. In detail, the emission reaches to the maximum value when the samples are oxidized at 300 °C; then a higher temperature leads to luminescence quenching.

Our investigations by tracking structural changes have shown a good correlation between the presented hydroxyl species and emission during the oxidation process as a function of thermal treatment. As a comparison, the defect-free *h*-BNNSs derived in DMSO or NMP exhibit undetectable emission in the same region, which has stressed the significance of the generated defects on the origins of visible emission in *h*-BN systems. The subsequent theoretical calculations by DFT have also supported the experimental results from the computed UV-Vis absorption spectra. It notes that the charged oxygen-related defects have been the most promising candidate in charge of the changed optical features in defective *h*-BN materials. In the theory, the O impurities

can click on the transitions of absorption, which is effectively responsible for the reproduction of the resulted fluorescence.

4.2. Boron nitride-titania mesoporous film heterostructures

This Section is summarized according to the following article: **Junkai Ren**, Luigi Stagi*, Luca Malfatti, Sebastiano Garroni, Stefano Enzo, and Plinio Innocenzi*. Boron nitride-titania mesoporous film heterostructures. *Langmuir*, **2021**, 37, 5348.

Various contents and figures in this Section are reproduced with permission of Ref.[26], Copyright (2021) American Chemical Society.
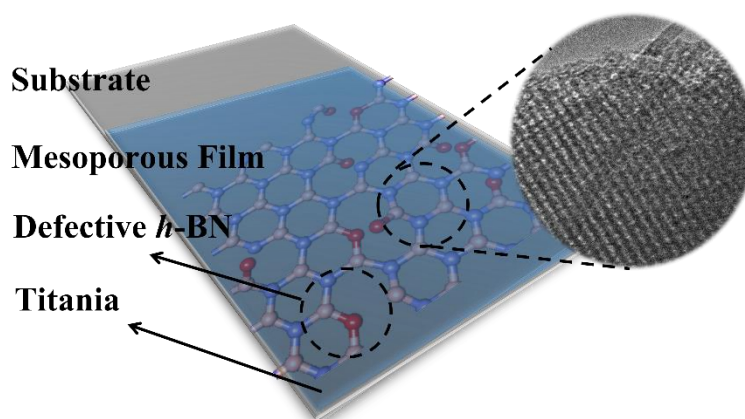
4.2.1. Introduction

Hexagonal boron nitride (*h*-BN) is a layered and optically active material with a structure similar to graphite. It possesses an ultrawide bandgap of ~ 6 eV and optical transparency in the visible range. 2D *h*-BN also represents a kind of particular nano insulators, which shows a weak p-type feature at high temperature (e.g. > 700 K) and a high resistivity (e.g. ~1600 $\Omega \cdot$cm at 790 K).[124]

h-BN nanosheets (BNNSs) can be prepared by both top-down and bottom-up methods, which allow producing 2D *h*-BN with few layers. A key issue in the synthesis is to control the defects. Hydroxyl-functionalization, for example, can induce important properties including solvent solubility, optical absorption, and photoluminescence.[9] Therefore, the assessment of the defective states is a mandatory step to construct the heterostructures for photocatalysis whose effects largely depend on the effective combination of optically active materials.

57

BN sheets have been well doped into some semiconductors for an enhanced photocatalytic response, including TiO_2, SnO_2, InS_2, etc., where, however, these nanocomposites have been mostly fabricated in the form of micro or nanoparticles.[125-127] Among them, titania shows an excellent photocatalytic effect and has been considered as the benchmark material. But European Union recently has classified titania powders as a category 2 carcinogen through inhalation, which has severely limited these applications of micro and nano- titania particles.[128] Considering the health risk, an alternative way is constructing BN-TiO_2 heterostructures in the form of mesoporous films by a bottom-up soft-chemistry approach, which can avoid the presence of TiO_2 particles. Meanwhile, the incorporation of 2D BN into thin porous films can allow producing advanced heterostructures with tailored functions extending their possible application fields.

Actually, the effective combination of h-BN and titania has been well investigated, as well as several applications, for example, water splitting and photocatalysis.[129] Particularly, sufficient effort has been dedicated to fabricating BN-TiO_2 nanocomposites for the enhanced photocatalytic response.[127] However, the current experimental results in the literature have not shown a coherent menu in terms of intrinsic physical-chemical properties. It seems to appear that the final contribution of BN to TiO_2 largely depends on the synthesis methods and the corresponding structural defects.[68, 130]

It is still mostly unexplored for the construction of heterostructures by incorporating 2D materials into mesoporous films. The key step is to design a preparation route that allows embedding 2D sheets into thin film without disrupting its original pore organization. The one-pot sol-gel technique, where the nanomaterials are directly dispersed in the sol of targeted precursors, has been the most feasible tool because all the engineering can be carried out via integrated processing.[131]

In this Section, we have used a template-assisted sol-gel approach to prepare a kind of BN- titania heterostructures. The mesoporous TiO_2 thin films are the matrix, and h-BN sheets include defect-free and defective two types. On one hand, the role of h-BN sheets has been explored in synthesizing heterojunctions. On another hand, their

photocatalytic response has been investigated and compared under UV light irradiation.

4.2.2. Experimental section

4.2.2.1. Preparation of *h*-BNNSs

Defective and defect-free *h*-BNNSs were prepared according to the *4.1 Section*. The sheets were finally dispersed in EtOH with a concentration of 5 mg mL^{-1} for next step.

4.2.2.2. Synthesis of BN-TiO$_2$ mesoporous film heterostructures

The mesoporous and heterostructure films were fabricated by a typical template-assisted route. Firstly, the precursor sol was prepared by adding 2.2 mL TiCl$_4$ and 1.3 g Pluronic F127 into 46.8 mL EtOH under continuous magnetic stirring. After 15 min, 3.6 mL H$_2$O was dripped into the mixing solution. The molar ratio of the final sol was TiCl$_4$: F127: EtOH: H$_2$O = 1: 0.005: 40: 10. After another 10 min, 600 μL BNNSs (two types, respectively) were added into the 6 mL titania sol for BN-TiO$_2$ heterostructure film. For controlled comparison, 600 μL EtOH was added into the 6 mL titania sol for titania mesoporous films.

Dip-coating technique (see **Scheme 4.2.1**) was used for depositing films with a 10 cm min^{-1} withdrawal rate by using silicon wafer and silica glass slide as substrate. The substrates were immersed in the titania-BNNSs sol for 30 s before extraction. The dip-coating was carried out in an environment with relative humidity low than 30% (controlled by dried air flow). These thin films of TiO$_2$, TiO$_2$-BNNS, and TiO$_2$-BNNS-defects were firstly dried at 60 °C for 10 h and then were thermally treated in air at different annealing temperatures (300, 350, and 400 °C).
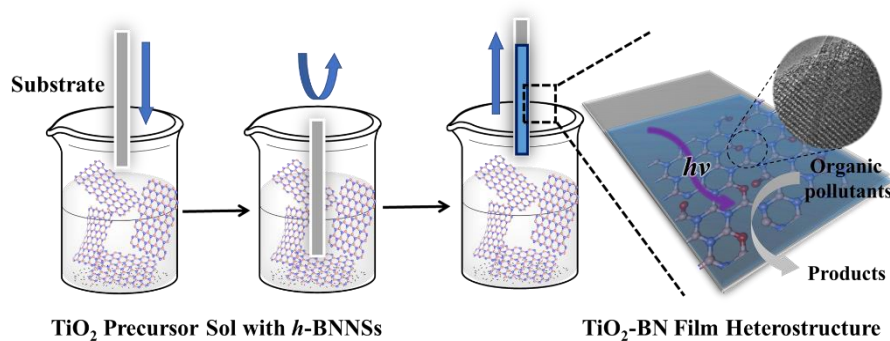
Scheme 4.2.1 Schematic illustration for the preparation of BN-TiO$_2$ heterostructures via dip-coating.

4.2.2.3. Evaluation of photocatalytic activity

Stearic acid was selected as a model to evaluate the photocatalytic effect according to the collected data of C-H vibrational stretching in $2945 - 2840$ cm^{-1} by FTIR spectra (see **Figure 4.2.1**).
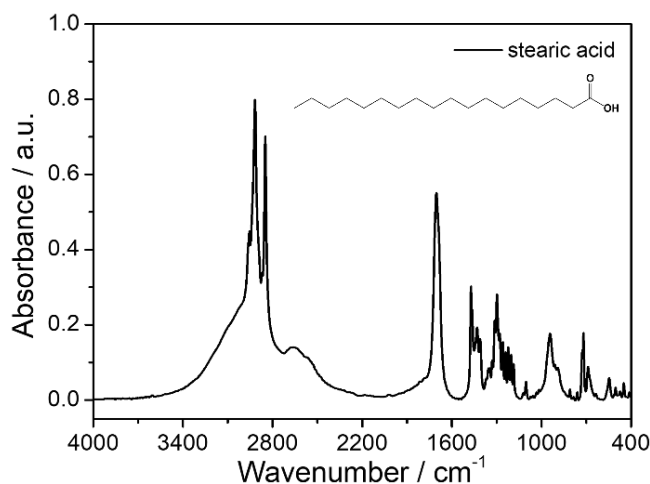
Figure 4.2.1 FTIR spectrum of stearic acid. Inset shows its molecular structure.

Firstly, 100 µL stearic acid solution (in EtOH, 3.3 mg mL^{-1}) was deposited on the mesoporous films via spin-coating at 1500 rpm for 30 s. Subsequently, the films were irradiated under 365 nm light with a distance of 10 cm to the UV lamp. FTIR spectra were recorded immediately after irradiation, and the illumination time was fixed from 0 to 120 min.

4.2.3. Results and discussion

4.2.3.1. Photocatalytic activity

Figure 4.2.2 shows the UV-photoinduced degrading curves of stearic acid on the different films produced at different temperatures. Herein, the intensity of IR absorption I_t is recorded as a function of exposure time t (min) under UV light; I_0 (at $t = 0$ min) represents the original IR intensity before irradiation; then the degradation value (*stearic acid/%*) can be calculated by the equation of "*stearic acid/% = I_t/I_0 * 100%*". Before evaluating the activity of films, reference curves are obtained by using the bare silicon or with BNNSs (defect-free and defective) as the surfaces for catalytic degradation under UV illumination (see **Figure 4.2.3**). The infrared intensity of stearic

acid keeps an unchanged trend after 35 min UV irradiation on silicon and BN sheets, suggesting that single *h*-BNNSs cannot present any catalytic activity if not integrated into TiO_2 or other semiconductors to form a heterostructure. The photodegrading data in **Figure 4.2.2** can be well fitted by an exponential decay rule of $I(t) = I_0 e^{-kt}$, where the parameter *k* corresponds to the degradation kinetics rate. The fitted *k* values are summarized in **Table 4.2.1**.

The mesoporous films after annealing at 300 °C show a relatively weak catalytic effect with comparable IR intensity decays (**Figure 4.2.2a**). In this case, two-hour UV exposure only allows ~30% removal efficiencies with *k* values at 0.004 min^{-1} ($\pm$ 5%) from the three types of films.
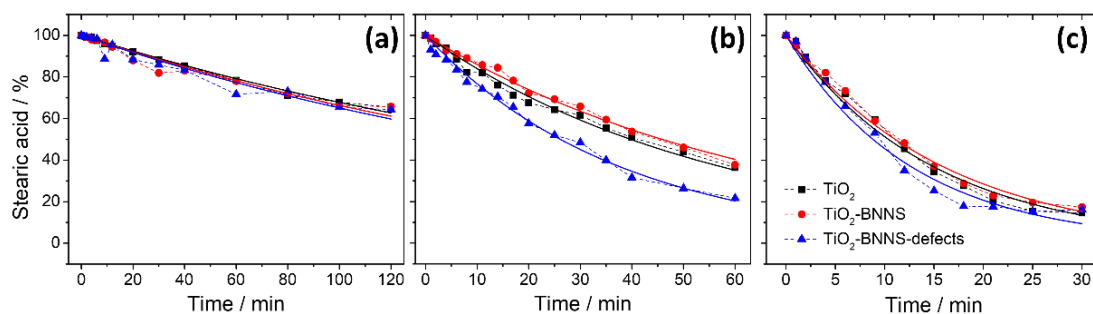
Figure 4.2.2 UV-deriving photodegrading curves of stearic acid on films of TiO_2, TiO_2-BNNS, and TiO_2-BNNS-defects, treated at temperatures of (a) 300, (b) 350, and (c) 400 °C, respectively. The dots are the recorded data, and the solid lines are the corresponding fitting results.
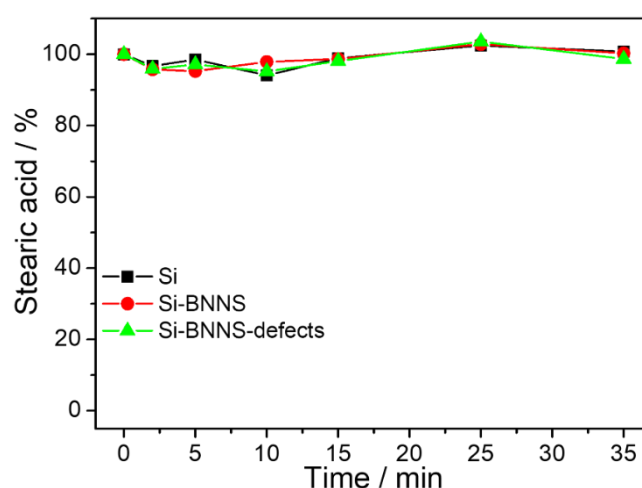
Figure 4.2.3 Photodegrading data of stearic acid deposited on a bare silicon substrate and substrates with BNNSs.

Table 4.2.1 Degradation rate (k values, min^{-1}) of stearic acid on these mesoporous films annealed at different temperatures.

Mesoporous films	300 °C	350 °C	400 °C
TiO$_2$	0.00389	0.0175	0.0649
TiO$_2$-BNNS	0.00410	0.0151	0.0637
TiO$_2$-BNNS-defects	0.00429	0.0266	0.0787

Interestingly, the films after treating at 350 °C exhibit an excellent photocatalytic effect with an obvious difference in degrading trends (**Figure 4.2.2b**). The degrading k value of TiO$_2$-BNNS-defects film (0.0266 min^{-1}) is around 50% higher than the corresponding values of TiO$_2$ and TiO$_2$-BNNS films (0.0175 and 0.0151 min^{-1}). It means that the defective BNNS structure plays an active role in the enhanced photocatalytic effect of TiO$_2$ mesoporous film. The photodegrading rate continues to increase when the annealing temperature reaches 400 °C in air, but the difference in the photocatalytic response of the three samples is smaller than that of 350 °C (**Figure 4.2.2c**).

Based on the above discussion, the photocatalytic performance mainly shows two aspects: (i) The degrading rate is improved by incorporating defective BNNSs into TiO$_2$ to form film heterostructure, whilst the TiO$_2$ and TiO$_2$-BNNS (defect-free) films exhibit similar results; (ii) The annealing treatment can enhance the photodegrading effect by promoting the transformation of amorphous titania into anatase. Moreover, treatment at a higher temperature can cause that the final k values tend to coincide regardless of the structures of the doping BN sheets.

4.2.3.2. Morphology and structure

To explore the impact of h-BN defects in the film heterostructures at 350 °C, extensive investigations have been carried out to characterize their structural features and optical properties. **Figure 4.2.4** demonstrates the TEM images of these nanocomposite films, revealing their well-organized porous mesostructures. The relevant wall-to-wall distance can be calculated by surface plot analysis, resulting in 11.74 nm (TiO$_2$), 11.99 nm (TiO$_2$-BNNS), and 11.56 nm (TiO$_2$-BNNS-defects),

respectively. Therefore, the incorporation of BN sheets, irrespective of bare and defective, does not influence the order and dimension of TiO_2 mesopores.
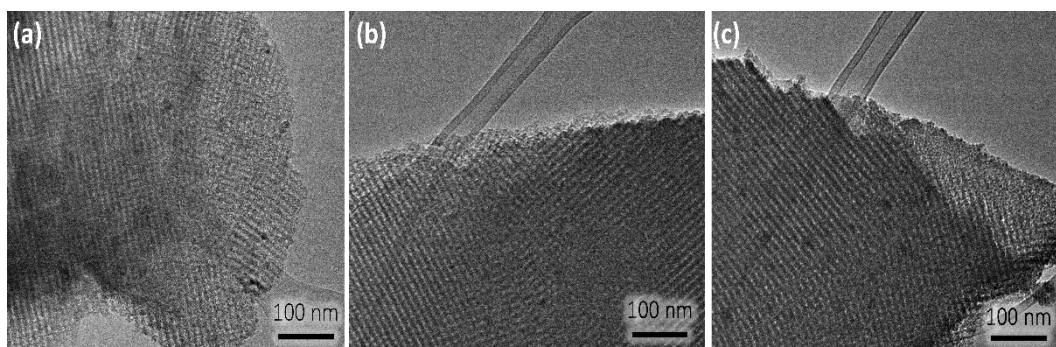
Figure 4.2.4 TEM images of the heterostructure films after treating at 350 °C: (a) TiO_2, (b) TiO_2-BNNS, and (c) TiO_2-BNNS-defects.

The XRD patterns in **Figure 4.2.5** characterize the composite films by four diffraction signals at 25.4, 38.1, 48.1, and 55.1°, stemming from (110), (004), (200), and (211) reflections of titania anatase.[132] The detected peak at 26.7° can be attributed to the (002) plane of *h*-BN phase. The detected XRD signals indicate a successful preparation of heterostructure by incorporating 2D BN materials into titania mesoporous films.
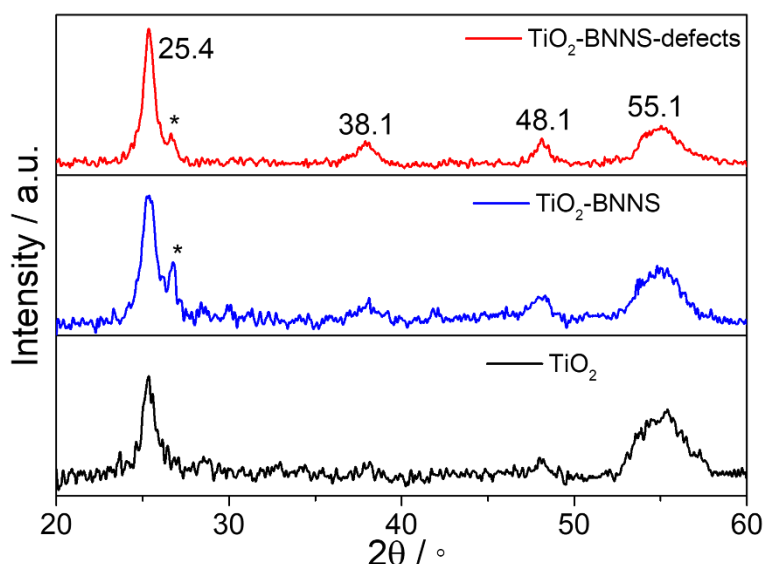
Figure 4.2.5 XRD patterns in the 2θ range of 20 – 60° from the nanocomposite films upon 350 °C. The symbol * represents the *h*-BN phase.

The crystallite size of titania can be estimated by the Scherrer equation (see **Supplementary Note II**). The main plane of (110) at 25.4° is selected for estimation

of crystallite size to result in 8.4, 9.0, and 10.5 nm for TiO_2, TiO_2-BNNS, and TiO_2-BNNS-defects, respectively. The data describes that the addition of BNNSs in the mesoporous films benefits the crystallization of titania, as presented by the increase in the crystallite size and also the intensity of the diffraction.

Raman spectra in **Figure 4.2.6** can well support the results from XRD analysis. Firstly, at a low treating temperature (e.g. 300 °C in **Figure 4.2.6a**) the titania films are mainly in an amorphous state, therefore the Raman signal from crystalline phase is too weak to detect. In **Figure 4.2.6b**, the small band at 1367.5 cm^{-1} is assigned to the G mode of h-BN, which appears in all the BN-TiO_2 films regardless the temperature and BNNS types. It indicates the implantation of 2D BN into titania in accordance with XRD results. The peaks at 145 and 640 cm^{-1} are from the characteristic E_g vibration of O-Ti-O in anatase phase,[133] which increase in intensity at higher temperature (e.g. 400 °C in **Figure 4.2.6c**) due to the thermal-induced transition of amorphous-to-anatase state.[134-135]
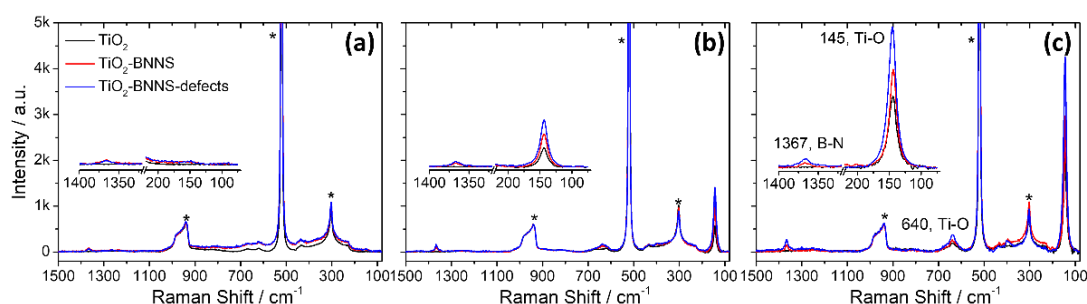
Figure 4.2.6 Raman spectra of the nanocomposite films after treating at (a) 300, (b) 350, and (c) 400 °C, inset showing the enlarged region in 1400 – 1300 and 200 – 70 cm^{-1}. The symbols * at 300, 520, and 940 cm^{-1} represent the Raman signals from the silicon wafer.

FTIR spectroscopy has also been carried out to analyze these films, and **Figure 4.2.7** shows the absorption spectra. Similar to Raman discussion, the infrared band at 463 cm^{-1} is assigned to the E_u (TO) mode of TiO_2 anatase, which is barely shown in samples upon 300 and 350 °C and becomes sharper and more intense after 400 °C treating. The IR peak at 1374 cm^{-1} is attributed to the in-plane B-N stretching mode, which does not change in position and intensity regardless of the annealing temperatures.

The FTIR spectra can also present the effect of thermal treatment on the hydroxyl groups and surfactant residues. The broad and intense band at high wavenumbers in

$4000 - 2600$ cm^{-1} is characterized by the Ti-OH and H-O (H$_2$O) groups, and decreases in intensity after higher temperature treatment. It represents the completion of condensation to construct the Ti-O-Ti netstructure. In another hand, the residual Pluronic F127 can be well monitored by IR absorption in $1600 - 1400$ cm^{-1} region of -CH$_2$ and C-O groups, which can be totally removed after treating at 400 °C.
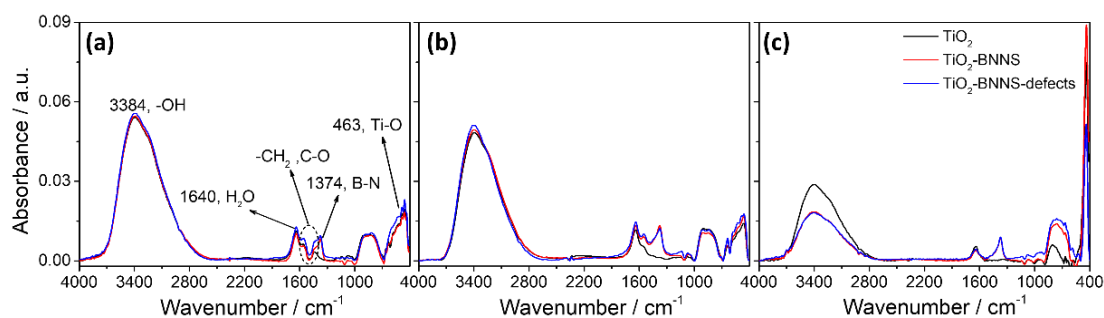
Figure 4.2.7 FTIR spectra of the nanocomposite films after treating at (a) 300, (b) 350, and (c) 400 °C.

The structural characterizations by XRD, Raman, and FTIR have highlighted the impact of *h*-BN sheets in prompting the heterogeneous crystallization process of titania film. The data can explain the enhanced photocatalytic activity of samples at 350 °C. However, this phenomenon still does not allow reaching a comprehensive understanding on the role of defective BNNSs in the photodegradation process.

4.2.3.3. Optical properties

Figure 4.2.8 shows the transmission spectra in UV-Vis range of the composite films on silica glasses. As expected from similar photocatalytic results, the three films upon 300 °C exhibit a comparable curve in transmittance. The transmittance at around 395 nm shows a decreasing trend from 86% to 65% (for the undoped titania) with the rise of the treating temperature from 300 °C to 400 °C. Adding the BNNSs further leads to an aggravating decrease of transmittance in the region. At 350 °C annealing process, for example, the defective BNNSs in titania matrix have a stronger absorption (77.5% *vs* 82.4%/83.3% at 380 nm in transmittance), which agree well with the better photodegrading effect compared to the pristine BNNSs. The improved absorption is contributed to the generated oxygen-defects in *h*-BN during the exfoliation in water.

In the visible region of $500 - 900$ nm, the transmittance of all the films can well

remain above ~80%, where both annealing treatment and the doped BNNSs cause a negligible influence.

Corresponding to the optical absorption, the band gap E_g values of the films can be evaluated via Tauc equation according to the testing absorption data (see **Figure 4.2.9** and **Supplementary Note I**). The incorporated BNNSs do not cause obvious change on E_g with respect to the undoped titania, whilst the increase of annealing temperature from 300 to 400 °C can shift the E_g from 3.40 ± 0.005 to 3.32 ± 0.007 eV.
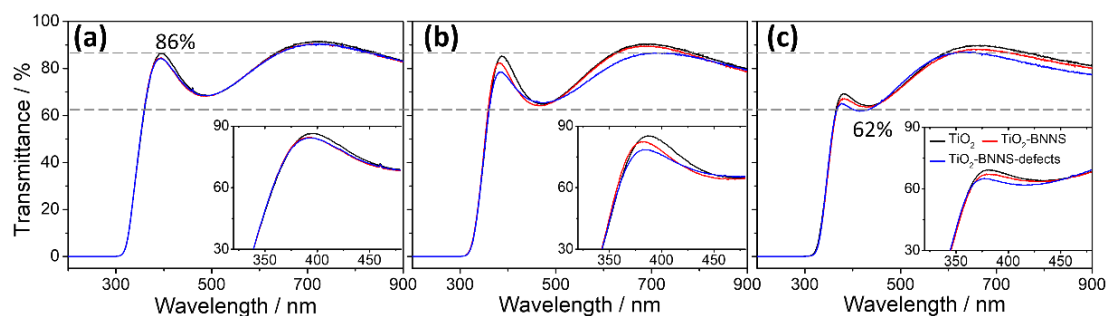
Figure 4.2.8 UV-Vis transmission spectra of the nanocomposite films after treating at (a) 300, (b) 350, and (c) 400 °C. The insets show the enlarged spectra in the range of 320 – 480 nm.
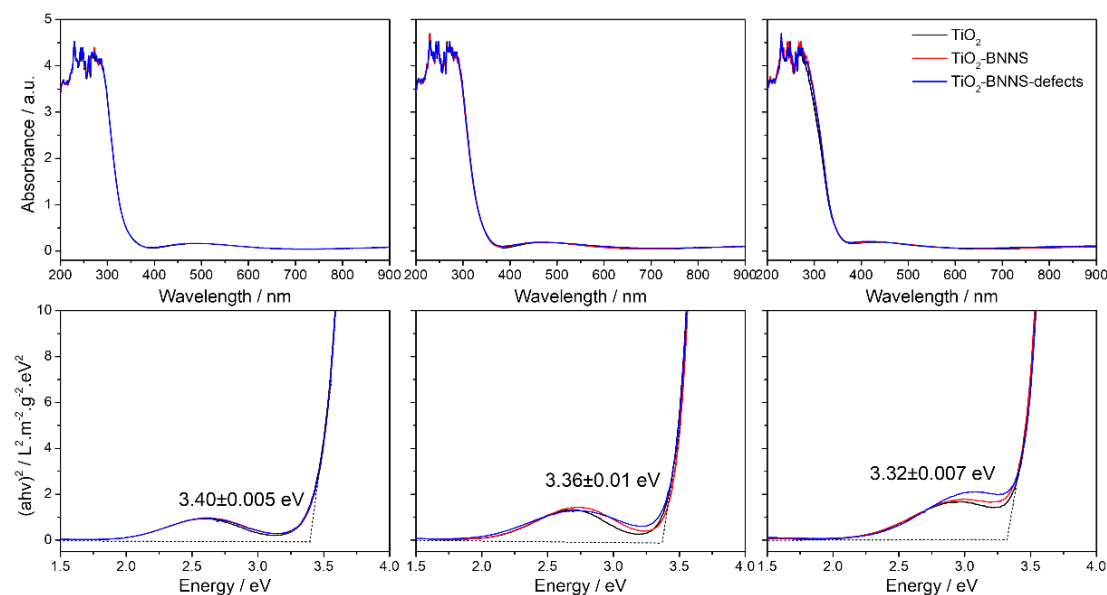
Figure 4.2.9 UV-Vis absorption spectra (on top) and E_g evaluation using Tauc equation (on bottom) of the nanocomposite films. The data of left to right are from the films firing at 300, 350, and 400 °C, respectively.

Spectroscopic ellipsometry has allowed measuring the thickness and refractive index (n) of these mesoporous films. In view of an experimental error of ~10 nm, the three films treated at different temperatures possess a similar thickness in range of 160 – 175

nm (**Table 4.2.2**). It suggests that these films do not undergo a detectable expansion or shrinkage during a narrow range of annealing temperatures (e.g. 300 – 400 °C). The containing BNNSs also cause a negligible impact on the final thickness.

Figure 4.2.10 shows the dispersion spectra of the refractive index as a function of wavelength in 380 – 900 nm. The refractive index goes up with an increasing temperature and is higher in the heterostructure films than in undoped titania. On the one hand, the rise of refraction can partially result from the increase in pore dimension of films, because the treatment at higher temperature can remove more surfactant templates (see FTIR).[136] On another hand, the increased crystallinity of titania can contribute to the rising refractive index (see XRD and Raman).[137]

Table 4.2.2 Thickness of the nanocomposite films tested by spectroscopic ellipsometer.

Mesoporous films	300 °C	350 °C	400 °C
TiO$_2$	161.7 ± 0.28 nm	158.2 ± 0.46 nm	169.8 ± 0.34 nm
TiO$_2$-BNNS	164.5 ± 0.21 nm	179.1 ± 0.30 nm	172.1 ± 0.50 nm
TiO$_2$-BNNS-defects	168.5 ± 0.23 nm	165.8 ± 0.17 nm	154.6 ± 0.70 nm
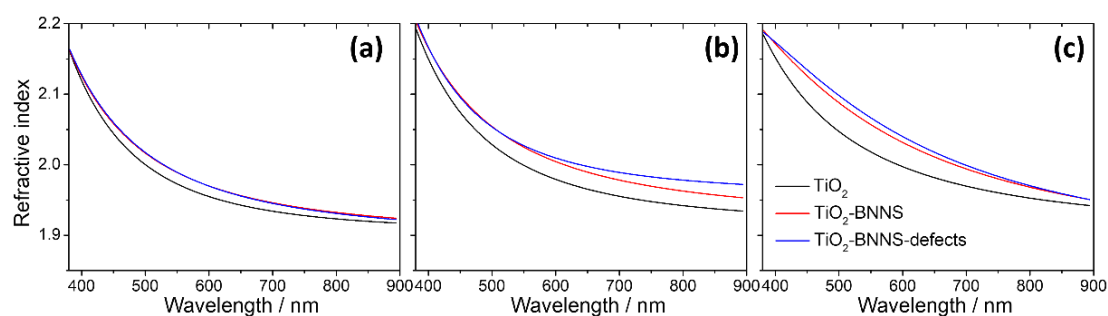
Figure 4.2.10 Refractive index as a function of wavelength in 380 – 900 nm of the nanocomposite films after treating at (a) 300, (b) 350, and (c) 400 °C.

These experimental data show that introducing defects into BNNSs can endow the final BN-TiO$_2$ heterostructure with an enhanced photo-responsive effect. The defective BN sheets can increase the absorbance in the UV region, and promote the hole reactions in photocatalysis. The annealing temperature is still an important impact on the photodegrading effect of the heterostructures. For example, after firing at 400 °C, the titania transformation from amorphous to anatase state can govern the light-triggered

catalysis mechanism, and the defective BNNSs thus do not improve the optical properties of the films in a significant way. Additionally, the presence of BN sheets can also reduce the energy barrier and promote the heterogeneous nucleation of the anatase phase in the mesoporous films.

4.2.4. Conclusions

A template-assisted self-assembly method has been used to fabricate a series of BN-TiO$_2$ mesoporous films. The exfoliated h-BN sheets can be well incorporated into titania without disrupting its pore order to form hetero-constructed films, which can promote the heterogeneous crystallization of amorphous titania into the anatase phase during the annealing process. The addition of defective BNNSs can produce an improved photocatalytic response from mesoporous TiO$_2$, because of a higher absorption in the UV range.

It has been a viable approach for controlling the properties of the heterostructures to fabricate a kind of BNNS-TiO$_2$ optically transparent films through deposition from their liquid phase sol-gel precursors.

Chapter 5. Boron Nitride Nanodots

Chapter 5 can be divided into the following two parts, Sections 5.1 and 5.2:

In Section 5.1, we have mainly explored the BN-based nanodots prepared via a bottom-up hydrothermal method with H_3BO_3 and NH_3 as precursors. A series of analytical characterizations, i.e., FTIR, XPS, TGA-DSC, describe the produced dots with a boron-oxygen-nitrogen-hydrogen (B-O-N-H) net-structure, hence, termed as boron oxynitride nanodots (BONDs). Fluorescent measurements of both 2D and 3D spectra show a well-defined two-color emission from the BONDs aqueous solutions, which can also be kept well in solid state by incorporating the dots into a hybrid organic-inorganic film.

In Section 5.2, we have prepared a kind of *h*-BN nanodots via a top-down route starting from bulk powders. The syntheses process involves a combination of thermal treatment and bath-sonication of bulk crystals in concentrated Brønsted acid, which allows etching edges and reducing size. An interesting finding is that an emission in UV region has been detected in the obtained BN particles, which is well correlated to a characteristic infrared-active mode. Besides, a broad emission is shown in visible area. The UV fluorescence will quench after thermal treatment higher than 100 °C; the visible band can reach a maximum in intensity upon treating at 200 °C. The latter one is attributed to the hydroxyl covalent functionalization of *h*-BN. Along with structural and optical characterizations, quantum calculations have evaluated the causes of Stones-Wales defects in the UV emitting and infrared vibration.

5.1. Two-color emissive boron oxynitride dots via bottom-up route

This Section is summarized according to the following article: **Junkai Ren**, Luca Malfatti, Stefano Enzo, Carlo Maria Carbonaro, Laura Calvillo, Gaetano Granozzi, Plinio Innocenzia*. Boron oxynitride two-colour fluorescent dots and their incorporation in a hybrid organic-inorganic film. *J. Colloid Interface Sci.*, **2020**, 560, 398.

Various contents and figures in this Section are reproduced with permission of Ref.[42], Copyright (2019) Elsevier Inc.
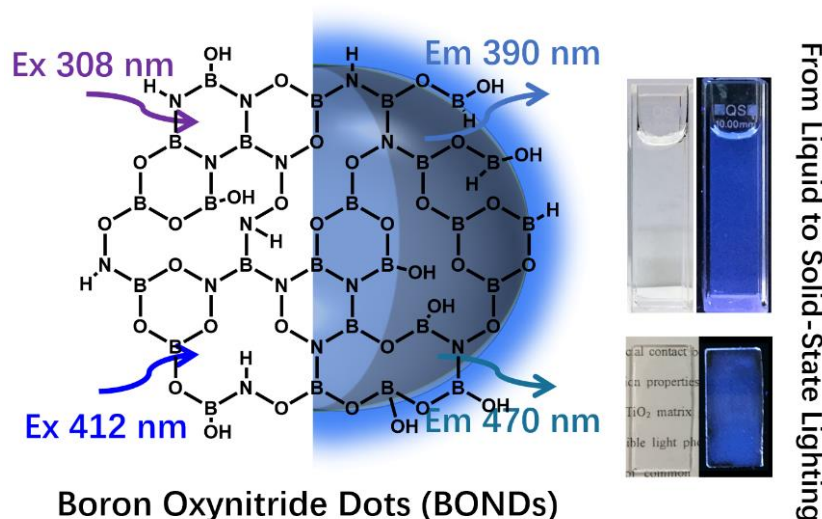
5.1.1. Introduction

Among 2D materials, hexagonal boron nitride (*h*-BN) monolayer has exhibited an excellent optical activity, which shares structural similarity to single-layer graphene. As reported, layered *h*-BNs are characterized by a large bandgap (experimentally, ~5.97 eV).[52] The optical properties of BN layers, particularly room-temperature and quantum emission, are driving scientists to invest efforts into the 2D BN-based materials. Recently, BN nanodots or quantum dots (QDs) have attracted increasing attention due to their excellent properties, such as stable photoluminescence (PL), good

dispersibility, outstanding chemical inertness, and low cytotoxicity.[35] Localized defects presented in the B-N structure are largely considered as the source of the visible emission in BN dots.

A homologous structure of bulk h-BN to graphite allows using similar routes for preparing graphene QDs to produce BN nanodots. For example, top-down methods, including high-intensity sonication,[138] sonication-solvothermal method,[38] laser irradiation,[139] and high-temperature defect route,[39] have been widely applied to cut BN flakes into smaller fragments and finally produce fluorescent BN dots. Meanwhile, a bottom-up route has become a feasible alternative approach for preparing BN dots by the chemical reaction between H_3BO_3 (B source) and NH_3 (N source) under a hydrothermal condition.[43-44] In compositions, it should be noted that apart from boron and nitride, these synthesized BN dots usually also contain oxygen, carbon, and hydrogen elements. It thus cannot avoid the presence of net-structure such as boron oxynitride and carbon-boron oxynitride in the resulted BN QDs. Actually, it is still a challenging task to prepare BN nanoparticles with a precisely controlled composition. Carbon and oxygen atoms generally enter in BN structure as impurities and defects in the preparation process. Carbon elements are implanted into BN QDs due to the carbonization of the involved organic matters, for instance, the liquid solvents after solvothermal treatment.

In another hand, the presence of defects takes an important role in the fluorescence features from BN materials.[59] The synthesis via bottom-up is a specially critical approach since it is not an easy process to control the chemical compositions of BN products even if there are only two precursors, e.g. H_3BO_3 and NH_3. Furthermore, the data in reports have shown several unclear and even contradictory points of composition in their BN dots, which opens some inquiries on the repeatability and reliability of bottom-up methods.[43-44] Therefore, the future development of this kind of materials largely depends on a good understanding of the relationships of their preparation-nanostructure-property. For a possible solid-state device, another important issue is to incorporate the dots into a proper transparent matrix, which can fully exploit the BNs optical properties and, particularly, their emission.

In this Section, a hydrothermal bottom-up approach has been performed to prepare a type of fluorescent BN-based dots, namely boron-oxygen-nitrogen-hydrogen dots (termed as BONDs). The BONDs show a two-color fluorescent spectrum. Furthermore, to meet the growing applications, sol-gel chemistry is applied to fabricate fluorescent thin films with solid-state lighting from the obtained BN dots, which can be used in lighting applications.

5.1.2. Experimental section

5.1.2.1. Preparation of BONDs

As shown in **Scheme 5.1.1**, the BONDs were prepared via a one-step hydrothermal method. Briefly, 0.31 g H_3BO_3 was dissolved in 10 mL H_2O, and 2 mL $NH_3 \cdot H_2O$ solution was subsequently added to form a transparent solution (molar radios of H_3BO_3 : NH_3 = 1 : 6). Then the solution was transferred into a Teflon-lined autoclave and kept at 200 °C for 10 hours with a 10 °C min^{-1} ramp rate. After cooling to room temperature, the produced solution was dialyzed against water (2000 MWCO) for 3 days to obtain purified BONDs. Finally, the BONDs solid powders could be obtained after the drying process. The thermal treatments of BONDs were performed in the air atmosphere for 1 h under 100, 200 and 300 °C, respectively.
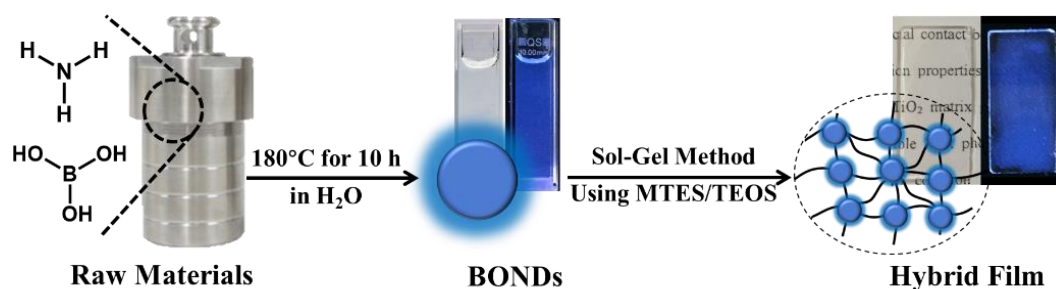
Scheme 5.1.1 Schematic illustration for the preparation of the BONDs and their sol gel glasses.

5.1.1.2. Preparation of BONDs-hybrid films

The BONDs-doped hybrid inorganic film was fabricated by a sol-gel chemical process, using hydrolytic condensation of silane with the catalysis of acid medium in presence of BONDs. Briefly, tetraethyl orthosilicate (TEOS) and methyltriethoxysilane (MTES) were mixed together with 2 mg BONDs, using H_2O, HCl, and EtOH as the

hydrolysis, catalyst, and solvent (molar ratios of MTES: TEOS: H_2O: EtOH: HCl = 0.3: 0.7: 3.7 : 3.7: 0.0124). After stirring for 30 min, the sol precursors were deposited on silica glass slides and silicon substrates by spin-coating at 400 rpm for 30 s. Lastly, the hybrid films were dried in an oven at 60 °C for 2 days.

5.1.3. Results and discussion

5.1.3.1. Morphology and structure

TEM image of the as-obtained BONDs is shown in **Figure 5.1.1a**, revealing an average diameter of ~10.20 nm. DLS curve in **Figure 5.1.1b** describes a hydrated size of the nanoparticles with a ~13.70 nm value, which agrees well with the TEM result.
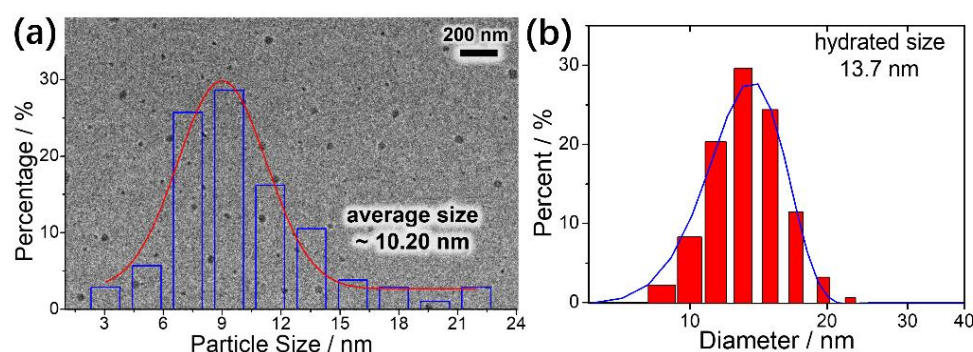
Figure 5.1.1 (a) TEM image, and (b) DLS curve of the as-prepared BONDs in aqueous solution. Overlapped inset of (a) is the counted size distribution.

Figure 5.1.2 presents the FTIR spectra between 4000 and 2800 cm^{-1} of the resulted BONDs and the dots thermally treated at 100 – 300 °C. **Figure 5.1.2a** shows the spectrum of the precursor H_3BO_3 as a comparative reference, which is mainly from B-OH stretching. Considering the diverse hydrogen-bonded (H-bonded) situations, the band can be divided into two kinds of deconvolutions. The blue line with higher wavenumber represents the H-bonded species of long-chain, whilst the red line is attributed to the smaller cooperative H-bonds (i.e. monomer, dimer, etc.).[140-141]

In **Figure 5.1.2b**, the similar absorptions of B-OH are detected at 3432 and 3181 cm^{-1} by multi-peak fitting analysis, as well as an additional peak at 3281 cm^{-1} due to the N-H stretching.[43-44] With an increase of heating temperature, the intensity of both blue and green lines in **Figure 5.1.2c-e** shows a rapid decrease. It indicates that the thermal treat can finally lead to that the residual B-OH bonds are becoming isolated in the

nanodots. The analysis based on **Figure 5.1.2** suggests that the B-OH groups are a significant presence in the BOND structure, which shows an expected condensation after undergoing a thermal process.
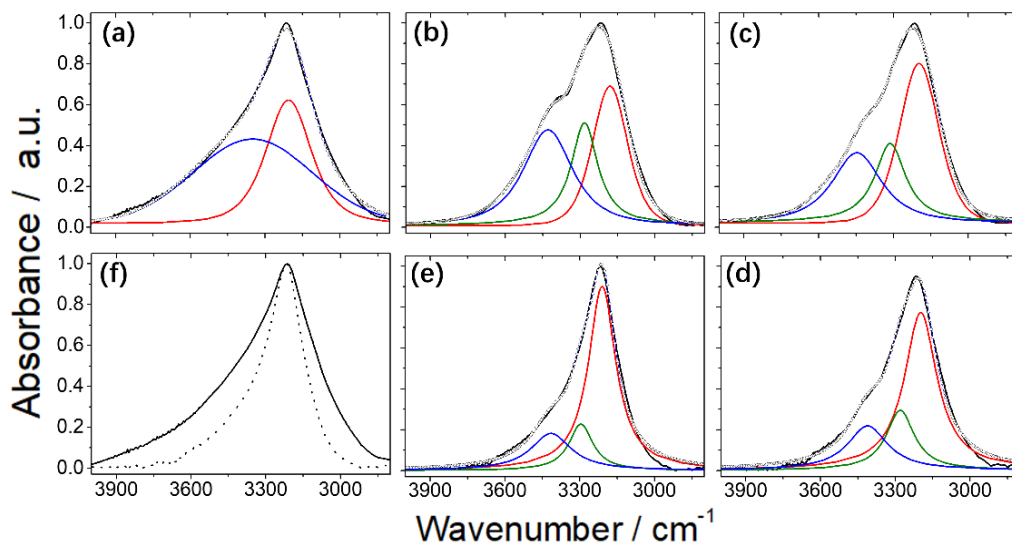
Figure 5.1.2 Normalized FTIR spectra in 4000 – 2800 cm^{-1} range from (a) H$_3$BO$_3$ as a reference, (b) the as-prepared BONDs, and the dots after thermal treatment at (c) 100, (d) 200, and (e) 300 °C, (f) comparison between H$_3$BO$_3$ (solid line) and BONDs at 300 °C (dot line). The black lines are the raw curves, the hollow dotted lines are the fitting results, the red and blue lines are the two deconvolutions attributed to B-OH, and the green curves to N-H.

More infrared information is shown in **Figure 5.1.3** to assess the evolutionary process of heating BONDs in the structural aspect. In the 900 – 500 cm^{-1} region of **Figure 5.1.3a**, the peaks at 882, 833, 712, 655, 594, and 545 cm^{-1} are owing to boron-oxygen related groups of B-O stretching, B-OH deformation, B-O-B deformation, BO$_3$ symmetrical deformation, B-OH antisymmetric deformation, O-B-O asymmetric stretching vibrations, respectively.[92, 142] On the other hand, the observed bonds at 744 and 821 cm^{-1} are attributed to the vibrations of N-H wagging and B-N-B out of plane. It is found that the intensity of the O-B-O group shows an increasing trend after thermal treatment, which is because of the B-OH condensation.

Figure 5.1.3b shows the FTIR spectra in 1700 – 1250 cm^{-1} range, which are characterized by three types of vibrational modes with an overlapping region. The peak at 1464 cm^{-1} originates from v_{as} (B-O) bond, while those at 1371 and 1338 cm^{-1} can be ascribed to v_s (B-N) and δ_s (B-N-B) bonds, respectively.
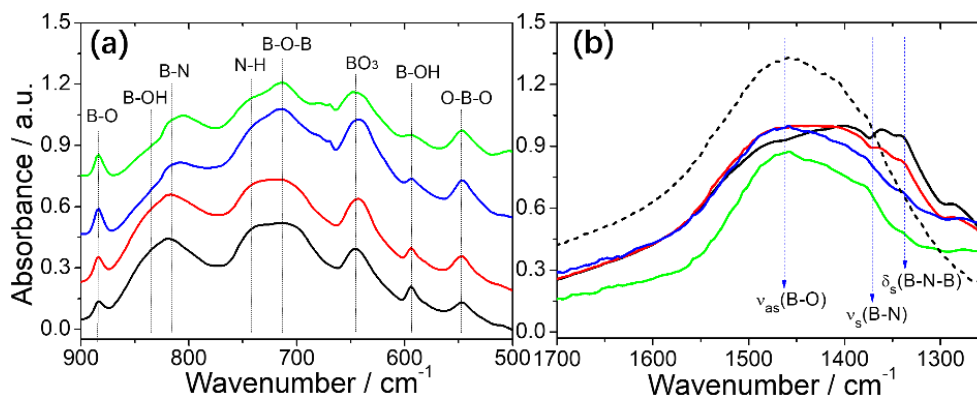
Figure 5.1.3 FTIR spectra in the ranges of (a) 900 – 500 cm^{-1} and (b) 1700 – 1200 cm^{-1} in the as-obtained BONDs and thermally treated at 100, 200, and 300 °C (the red, blue, and green lines), respectively. The dotted line in (b) is the spectrum of H$_3$BO$_3$.

The infrared data also shows the possibility of residual boric acid still present in the produced BONDs. The residue of H$_3$BO$_3$ in produced BONDs can be estimated according to TGA-DSC measurement, which is carried out from room temperature to 500 °C. As shown in **Figure 5.1.4**, there are two endothermic reactions happened at 132 and 162 °C successively, which correspond to the dehydration process and B-OH condensation. The assessed value is ~5.5% of present H$_3$BO$_3$ in the products by calculation using TGA data (see **Supplementary Note III**).
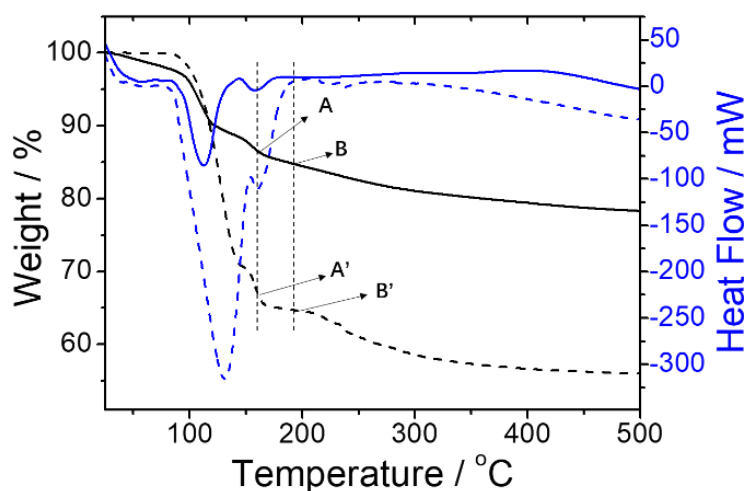
Figure 5.1.4 TGA (wt%) and heat flow (mW) of the as-prepared BONDs (solid line) and a reference H$_3$BO$_3$ (dot line) as a function of temperature from 25 to 500 °C.

XPS analysis has been performed to explore more composition characteristics of the series of products. **Figure 5.1.5** exhibits high-resolution spectra of B 1s and N 1s regions and **Table 5.1.1** summarizes the relevant fitting data. The raw B 1s spectra can

be deconvoluted into three kinds of chemical components. The first peak at ~190 eV is assigned to the interaction of B bound to N atoms,[143-144] which is singed as B-N and corresponding to the bands at 1371 and 821 cm^{-1} of FTIR. The second but the main one peak at ~192 eV is ascribed to the B bound to O and N atoms,[43, 143] labeled as B-(N, O) component. The third peak at ~193.5 eV is due to the B bound to O atoms (termed as B-O),[43] reflecting an incomplete hydrothermal reaction of B and N precursors. When the pristine BONDs are thermally treated upon increasing temperature, the B-(N, O) area goes down, and the B-O region goes up in intensity, which is caused by the oxidation process during the material treatment in the air atmosphere.

As for the N 1s region, it is also divided into three parts including N-B, N-(B, O), and N-H bonds at 398.0, 399.5, and 401.7 eV respectively.[43, 143-144] Obviously, N-H composition has been the main interaction, which is formed by the incomplete reacting NH$_3$ and edge NH$_2$ groups. The rise of treating temperature will also lead to a decrease in the intensity of N-B and N-(B, O) related compositions.
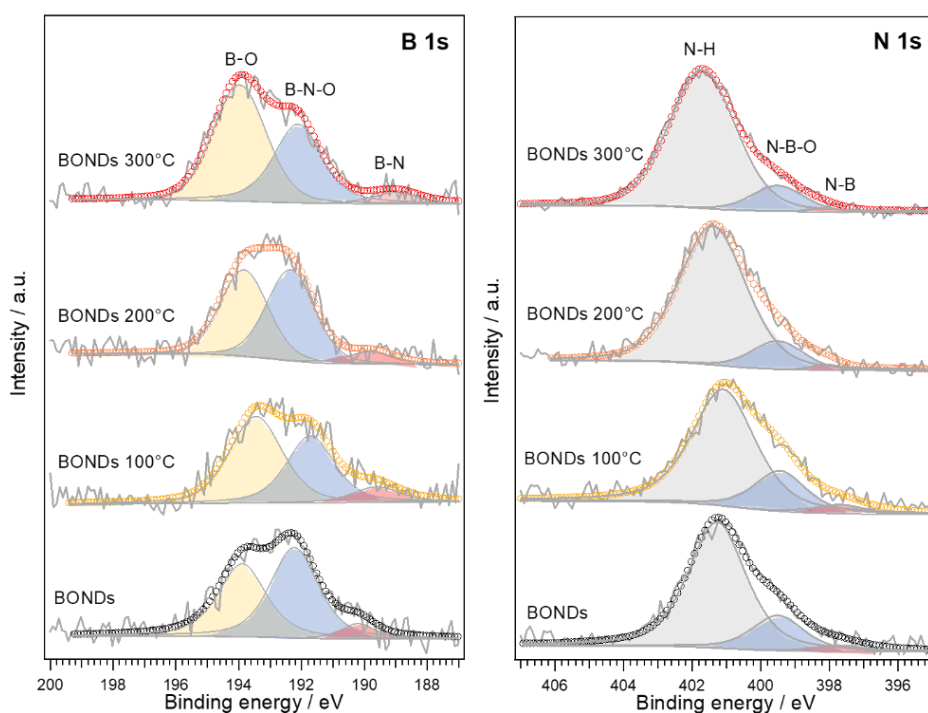
Figure 5.1.5 B 1s (left) and N 1s (right) XPS spectra of the BONDs before and after thermal treatments.

Table 5.1.1 Data of B 1s and N 1s XPS results of the BONDs before and after thermal treatments.

BONDs	B 1s			N 1s		
	B-N	**B-(N, O)**	**B-O**	**N-B**	**N-(B, O)**	**N-H**
As-prepared	190.1 eV	192.1 eV	193.7 eV	397.6 eV	399.4 eV	401.2 eV
	6.2 %	51.0 %	42.8 %	3.3 %	19.5 %	77.2 %
100°C	189.5 eV	191.7 eV	193.4 eV	397.6 eV	399.3 eV	401.2 eV
	8.9 %	38.5 %	52.6 %	4.6 %	21.1 %	74.3 %
200°C	189.7 eV	192.2 eV	193.7 eV	398.1 eV	399.4 eV	401.3 eV
	7.3 %	47.5 %	54.8 %	1.5 %	13.0 %	85.5 %
300°C	189.4 eV	192.2 eV	193.8 eV	398.1 eV	399.4 eV	401.6 eV
	5.5 %	38.6 %	55.9 %	1.0 %	12.4 %	86.6 %

The XRD test of the pristine BONDs is shown in **Figure 5.1.6**, which shows the coexistence of both H_3BO_3 sassolite (JCPDS No. 00-030-0620) and h-BN crystalline (JCPDS No. 01-073-209). The fitting result by HighScore Plus Software exhibits the content of *h*-BN phase is limited of ~5%, indicating amorphous-state is the main domain in the BONDs instead of crystallization.
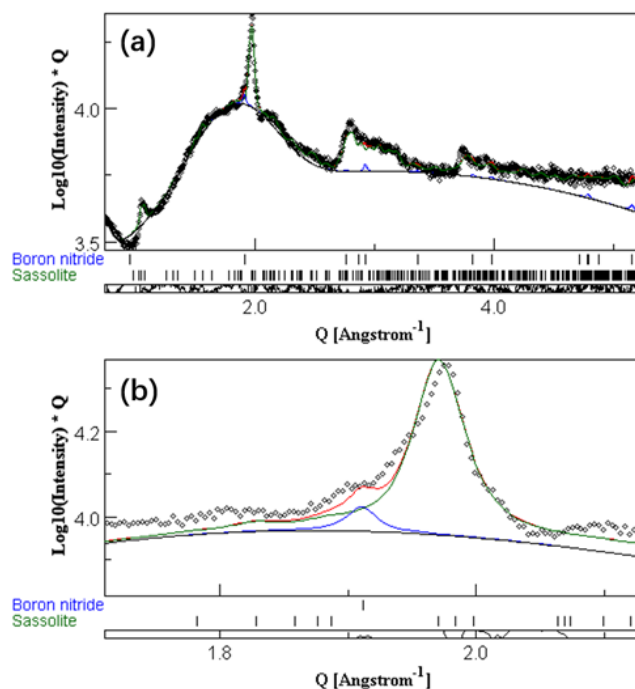
Figure 5.1.6 (a) XRD analysis of the as-obtained BONDs. (b) Enlargement of the overlapped range of H_3BO_3 and h-BN which has been deconvoluted.

According to the above analysis, **Scheme 5.1.2** describes a possible structure and composition of the as-prepared nanoparticles. It is important to point out that B-N is

not the basic unit, while boron-oxynitride is the main ingredient. Different from some publications, there is no carbon-containing matter in the obtained dots, which is already sure from the FTIR data. Meanwhile, the content of B atoms is much larger than N atoms, although the molar of H_3BO_3 to $NH_3 \cdot H_2O$ reaches up to 1: 6. The hydrothermal treatment allows the O and H in boric acid to form boroxyl ring (see **Scheme 5.1.2a**), whilst the introduction of NH_3 can promote the final formation of boron-oxynitride. The structural characterizations suggest the nanoparticles possess a crosslinked boron-oxygen-nitrogen-hydrogen (B-O-N-H) net-structure (see **Scheme 5.1.2b**).
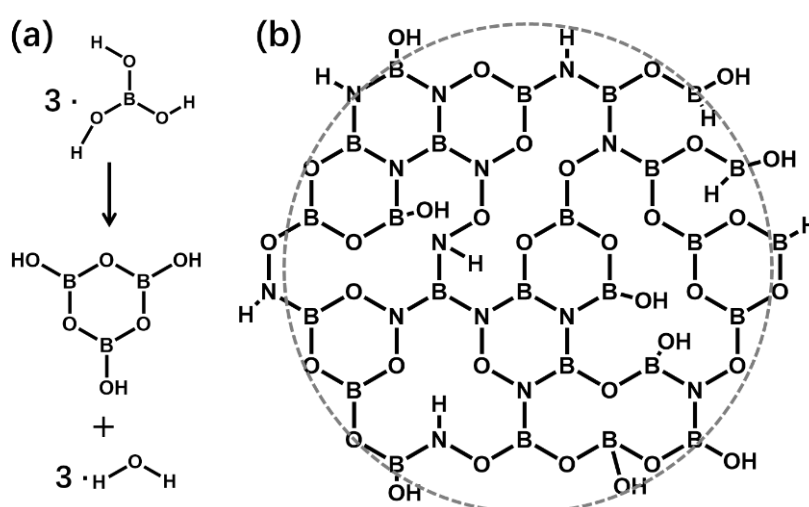
Scheme 5.1.2 (a) The formation route from boric acid to boroxyl ring, (b) A possible netstructure of the BOND materials.

5.1.3.2. Optical properties

The UV-Vis absorption spectra of these dots are shown in **Figure 5.1.7**, as well as their corresponding Gaussian deconvolution analysis. From a general overview, the thermal treatment can lead to the decline of absorption in intensity. These spectra are divided into four areas: the first one at 221 nm shows an intense and sharp shape, while the other three bands with long-overlapped regions are at 264, 308, and 413 nm, respectively.

Although the structure of BONDs is not pure BN phase, the peaks at 221 and 264 nm are actually similar to absorption states of BN layered sheets.[145] Another two bands, located at 308 and 413 nm, are possibly contributed from the presence of net-structure or BO_x^- defects (x = 1, 2), as well as the H and O related impurities.[146-147]
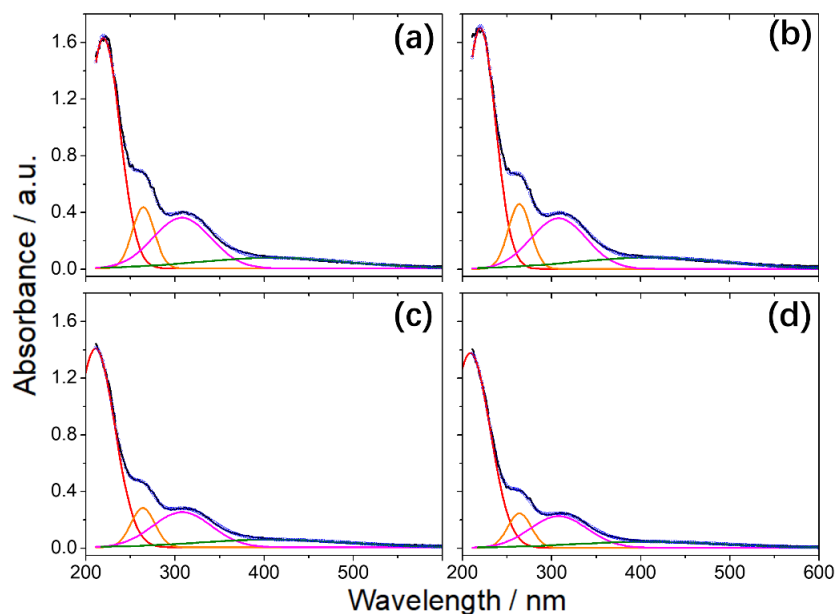
Figure 5.1.7 The UV-Vis absorption spectra and their relevant peak-fitting results of the as-prepared BONDs (a), and treated at 100, 200, and 300 °C (b-d), respectively, in aqueous solutions. The colorful lines are the deconvoluted bands with peaks at 221, 264, 308, and 413 nm, respectively.

Furthermore, the absorption peak at the low wavelength is assorted to the bandgap (E_g) of BN (see **Supplementary Note I**). As shown in **Figure 5.1.8**, the E_g values are calculated by the general Tauc method according to the deconvoluted UV-Vis data. The evaluated E_g value in BONDs shifts from 5.02 to 5.14 eV with an increasing heating temperature, which is owing to the reduction of hydroxyl-related species.[148] Compared with the E_g of reported h-BN sheets, the value of BONDs is lower because of the presence of oxides.
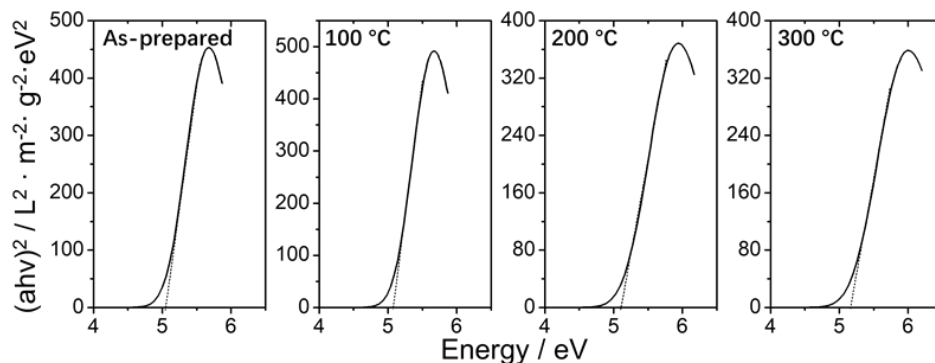
Figure 5.1.8 The evaluation of the energy gap for these BOND nanoparticles.

The fluorescent features have been presented by 3D excitation-emission-intensity PL spectra in **Figure 5.1.9**. The PL map of the as-obtained BONDs is represented with well-defined double-color emissive centers under different excitation wavelengths. As shown in **Figure 5.1.9a**, one is in the violet range of ~375 – 430 nm, with the best emission peaking at 390 nm under the excitation wavelength of 310 nm; the other is in the blue range of ~430 – 550 nm, where the maximum emission locates at 470 nm when the excitation light is 410 nm. The thermal treatments do not cause a shift of the two emissive peaks, while the fluorescence shows a decreasing trend in intensity, and the two-color region is more overlapped (see **Figure 5.1.9b-d**).
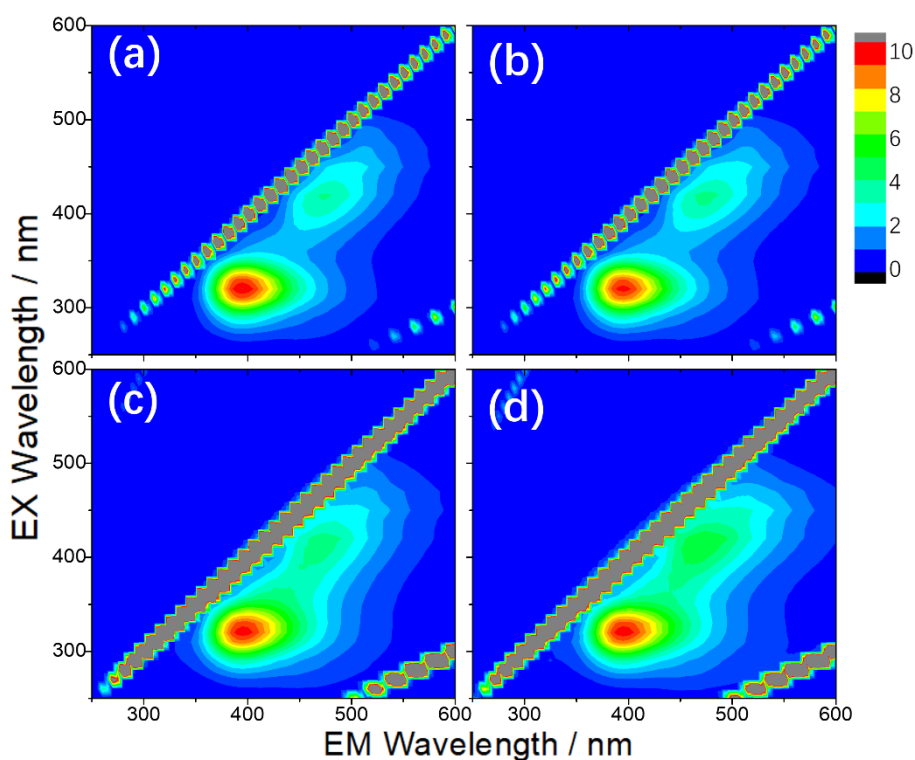
Figure 5.1.9 The 3D excitation-emission-intensity spectra of the as-prepared BONDs (a), and treated at 100, 200, and 300 °C (b-d), respectively, in aqueous solutions. The intensity scales for (a-d) are from 0 to $4.7*10^6$, $4.7*10^6$, $2.6*10^6$, and $9.3*10^5$, respectively.

Figure 5.1.10 further summarizes the relative changes of the two fluorescent centers and corresponding absorbed bands, as the function of the increasing treating temperature. It is clearly found that the fluorescent intensity decreases with an almost consistent trend of the intensity in the absorption band, which is also reflected in the TGA curve in **Figure 5.1.4**. Firstly, the BONDs are stable up to 100 °C in aspects of

optical intensity and weight. Subsequently, the decrease of fluorescence also shares with a similar path of structural degradation under higher temperatures. A similar change trend allows identifying the relationship between emission and absorption: The violet emission is from the absorption band at 308 nm, and the blue light is excited in the absorption centered at 413 nm. The falling optical performance is probably because that the thermal treating can promote the condensed process of B-OH and further reduce their defects, which is already shown in FTIR and XPS analysis (in **Figures 5.1.2** and **5.1.5**).
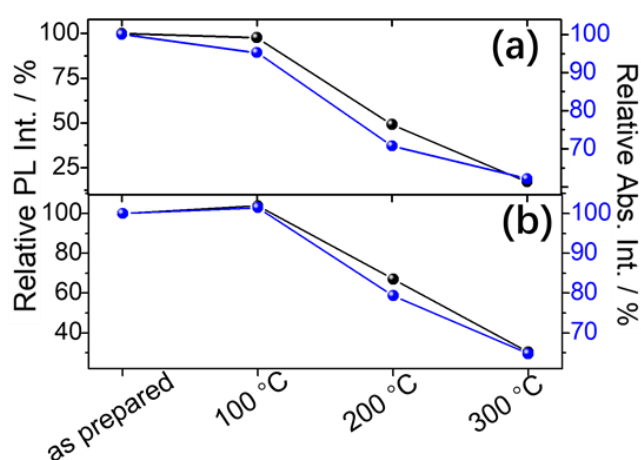
Figure 5.1.10 The relative intensity of emission (black dots) and absorption (blue dots) spectra: (a) λ_{ex} = 390 nm, λ_{abs} = 308 nm, (b) λ_{ex} = 470 nm, λ_{abs} = 413 nm.
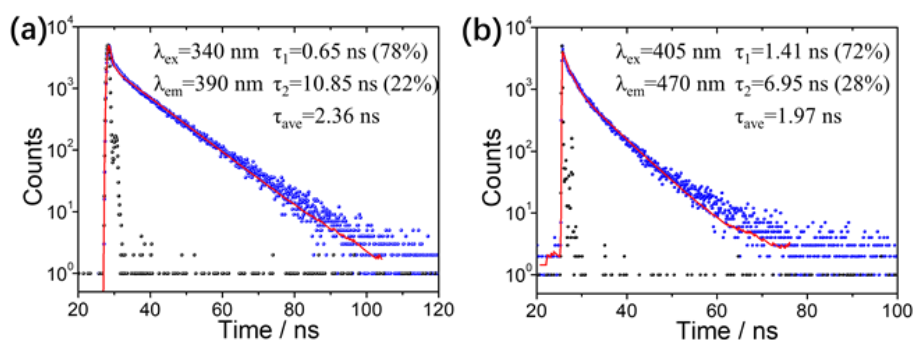
Figure 5.1.11 The time-resolved fluorescence spectra for the two-color emission from the as-prepared BONDs in an aqueous solution.

The fluorescent lifetime of the sample is obtained by the time-resolved spectra in **Figure 5.1.11**, which shows that there are at least two components, a slow and a fast, for the two emissions. Then the QYs of the BONDs solution are assessed by an absolute

testing way with the values of $7.4 \pm 0.7\%$ and $4.6 \pm 1.1\%$ under 310 and 410 nm excitations, respectively.

5.1.3.3. Solid-state film based on BONDs

The realization of solid-state lighting from BONDs is of great importance for more practical applications such as lighting and displays. It is a popular strategic technology to prepare fluorescent glasses via embedding the nanoparticles into sol-gel derived from Ormosil.

As shown in **Figure 5.1.12**, the optical features of the dots in water including both UV-Vis absorption and fluorescent spectra can be kept well when employed into methyltriethoxysilane (MTES) - tetraethoxysilane (TEOS) hybrid film. This means the emission from the nanoparticles is not easily affected by the chemical environment, which creates an opportunity to fabricate solid-state devices of the BONDs.
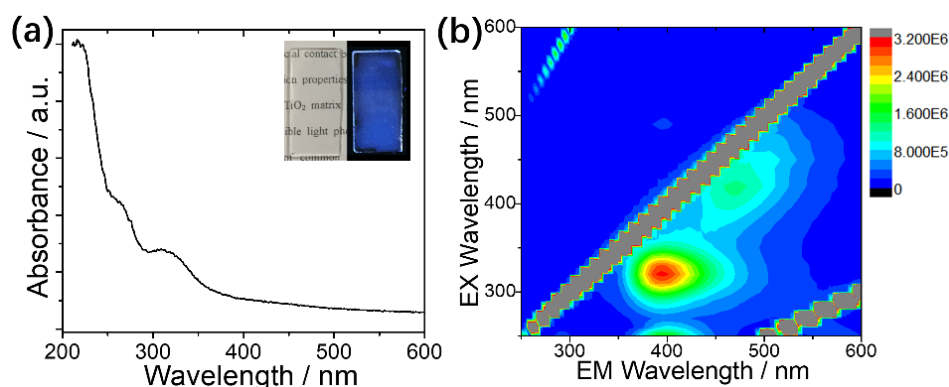
Figure 5.1.12 (a) UV-Vis absorption and (b) 3D PL spectra of the BONDs-doping hybrid film. The inset of (a) shows the optical images of the film under sunlight and 365 nm UV light.

5.1.4. Conclusions

In conclusion, the BONDs have been obtained via hydrothermal process. Two fluorescent peaks can be observed at 390 and 470 nm from the 3D PL excitation-emission spectra of the resulted nanoparticles. The BONDs are stable in both structure and emission up to 100 °C, however, a higher temperature (e.g. 200 or 300 °C) will cause the decrease of fluorescence in intensity because of the reduction of net-structure and defects.

To endow the BONDs with solid-state emitting, the fluorescent film is fabricated via embedding the as-prepared dots into Ormosil sol-gel, which can meet much more requirements of applications. Compared with the aqueous solution, the organic-inorganic hybrid silica film shows a similar two-color emission and UV-Vis absorption spectra, which lays the foundation for their applications in solid-state devices.

5.2. UV-emissive boron nitride nanodots by top-down route

This Section is summarized according to the following article: **Junkai Ren**, Luigi Stagi*, Luca Malfatti, Carlo Maria Carbonaro, Gaetano Granozzi, Laura Calvillo, Sebastiano Garroni, Stefano Enzo, and Plinio Innocenzi*. Engineering UV-emitting defects in h-BN nanodots by a top-down route. *Appl. Surf. Sci.*, **2021**, 567, 150727.

Various contents and figures in this Section are reproduced with permission of Ref.[10], Copyright (2021) Elsevier B.V.
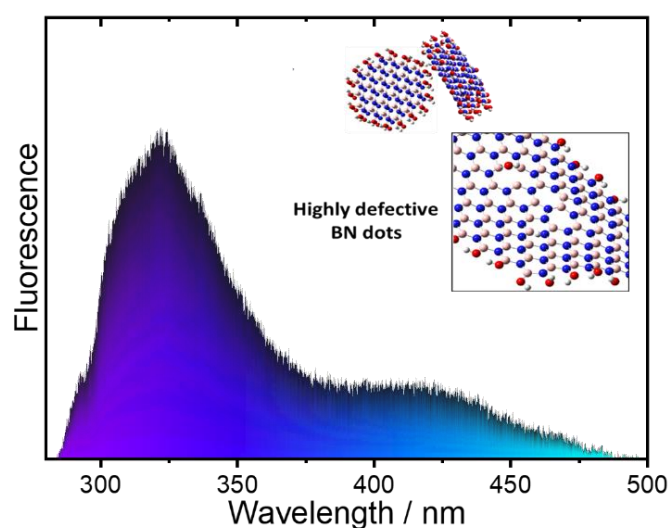
5.2.1. Introduction

Hexagonal boron nitride (*h*-BN), also called "white graphene", is characterized by a large bandgap of ~6.0 eV, making it an exciting two-dimensional (2D) layered material in electronics and optoelectronics.[108] In recent years, *h*-BN nanodots have been prepared via similar strategies of graphene quantum dots (GQDs). The emissive mechanisms of BN dots are usually attributed to the radiative recombination in the present defects, for example, boron/nitrogen vacancies, carbene structure, and oxygen-doping.[36]

The emerging efforts on BN dots have promoted the development of different synthesis routes. The control of processing parameters can allow preparing various BN

systems with different properties. Currently, some kinds of precursors (for instance, H_3BO_3, NH_3, $C_3H_6N_6$, $CH_3CH_2NH_2$) have been developed to prepare BN particles via a bottom-up hydrothermal or solvothermal method.[42-43, 45, 149] In **Section 5.1**, a type of "BN dots" were produced using a hydrothermal process from H_3BO_3 and NH_3, where the products are finally proved with a boron-oxynitride-hydrogen structural network. Generally, the bottom-up methods cannot allow the production of pure BN dots, and the impurities including carbon and oxygen cannot be avoided in the structure that affects the properties of the resulted materials.

The top-down route is an alternative to produce BN nanodots where the bulk hexagonal crystals can be exfoliated and cut into small fragments via cavitation process. Deionized water, ethylene glycol (EG), 1-methyl-2-pyrrolidone (NMP), and dimethylformamide (DMF) are the most used solvents in these top-down techniques, such as high-intensity sonication, ball-milling, solvothermal, and microwave treatments.[38, 61-62, 150] The use of organic solvents generally leads to the incorporation of impurities (e.g. carbon, oxygen, and hydrogen) into the B-N structure of the final particles. In particular, the introduction of carbon atoms is the main source of uncertainty in understanding and modulating the resulting structural and optical properties of *h*-BN systems.[151-152] Therefore, a carbon-free solvent is a good selection for the exfoliation to avoid the presence of carbon matter.

Great efforts have been devoted to the engineering of BN-based systems. Thus, it has been wildly reported that BN nanodots possess good aqueous dispersibility and show blue fluorescence under UV irradiation. However, it is still a challenging task to fabricate BN dots with controlled properties in aspects of dimension, structure, and functional response. A top-down design has the advantage of controlling composition because it starts from BN bulk materials and allows expecting the formation of possible defects. In this Section, a two-step approach has been developed to produce BN dots by heating and bath-sonicating bulk *h*-BN in Brønsted acid. The synthesized dots show both UV and visible emissions under different excitation wavelengths. Particularly, a special vibration can be strictly connected with the new UV luminescence.

5.2.2. Experimental section

5.2.2.1. Preparation of BN nanodots

BN dots were prepared via a top-down exfoliation route (see in **Scheme 5.2.1**). Firstly, 10 mg bulk *h*-BN powders were dispersed into 5 mL H_3PO_4 in a glass vial with a capacity of 25 mL. Subsequently, the dispersion was put in an oven under 200 °C for 1 h. When cooling down to room temperature, 15 mL H_3PO_4 was further added into the vial and then sealed. After 15 h bath sonication, the large fragments and unexfoliated *h*-BNs were precipitated by centrifugation at 12000 rpm for 15 min. Then the supernatant containing BN dots was diluted by water, and the H_3PO_4 was removed through dialysis against water (2000 MWCO) for 3 days. Finally, the BN nanodots in aqueous solution were collected by filtering via a 0.22 μm nylon membrane. The solid products could be obtained by a drying process in oven.

Thermal treatment of BN dots was performed in air at different temperatures, such as 100, 200, and 300 °C for 1 h.
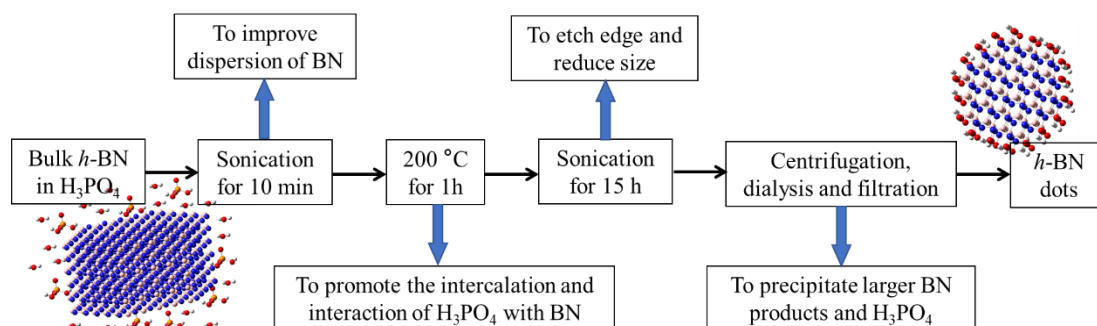
Scheme 5.2.1 Schematic illustration on synthesis process of BN nanodots.

5.2.2.2. Quantum chemical calculations

Density functional theory (DFT) combined with a cluster-based method was used for the investigation on the relationship of optical, structural, and vibrational features of *h*-BNs. The BN clusters of 180 atoms arranged in 61 rings were used to simulate the BN dots and experimental data by calculations using the Gaussian 16 code.[119] In the beginning, the clusters were optimized, and the B3PW91 functional was applied to calculate the corresponding energies and vibrational modes.[153] The basis sets for B, N and H atoms were accessed via the 6-31G(d,p). Starting from the relaxed structures, the

time-dependent (TD)-DFT method was used to calculate the electronic excitation energies with Becke's three parameters and the nonlocal B3LYP correlation functional of Lee-Yang-Parr.[120, 154] The vibration frequencies were refixed by a scaling factor of 0.9501.[153] These calculations were carried out with a medium of vacuum, and GaussView 6 was employed to interpret the simulation data.[121]

5.2.3. Results and discussion

5.2.3.1. Morphology and structure

The TEM images in **Figure 5.2.1a** have confirmed the formation of BN nanodots by Brønsted acid etching via sonication process. The BN particles appear of near-spherical shape with a size of less than 10 nm. The corresponding AFM profile is reported in **Figure 5.2.1b**, showing that the dimension of the nanodots does not exceed 15 nm in the height direction. The morphology results confirm the presence of layered structure without complete exfoliation, possessing at least a dozen BN layers.
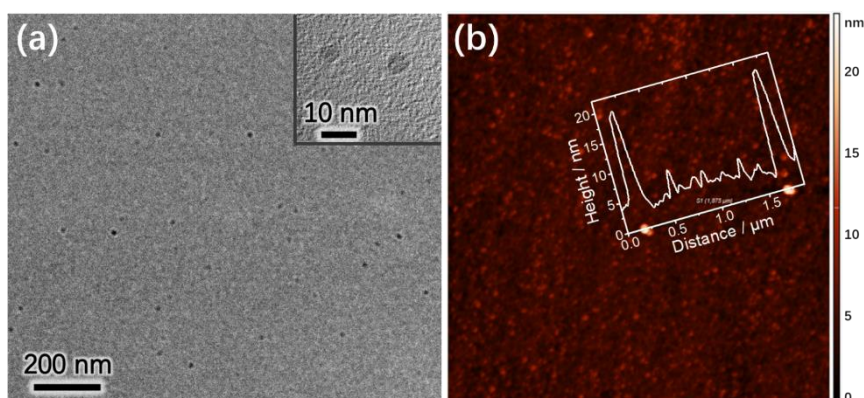
Figure 5.2.1 (a) TEM and (b) AFM images of the as-prepared BN dots. The inset in (a) shows an enlarged image, and in (b) corresponds to the line profile.

The inset in **Figure 5.2.1a** represents an enlarged region with two particles, however, which cannot allow collecting details of the structural edges or planes, because of the low contrast of the low-density BN with respect to the carbon support film. Additionally, the morphology analysis does not provide sufficient insights into the top-down exfoliation. Herein, Raman and XRD measurements have been further employed to explore the synthesis and thermal effect in air on BN products. For example, a shift toward a higher wavenumber can be observed from the characteristic E_{2g} mode of h-

BN when the layer number of the stacked hexagonal structure decreases from bulk scale to monolayer condition.[93, 155] The Raman spectra in **Figure 5.2.2a** show the E_{2g} signature of bulk BN at ~1366.5 cm^{-1}, and the values do not reflect a significant difference between the dots (both as-prepared and thermal-treated samples) and bulk crystal. It means that the nanodots possess more than 10 BN layers, in good accordance with AFM analysis. In another hand, the characteristic signal at 26.8° of 2θ from the XRD pattern (**Figure 5.2.2b**) can also confirm the stacked hexagonal geometry of the produced nanoparticles, corresponding to (002) plane.
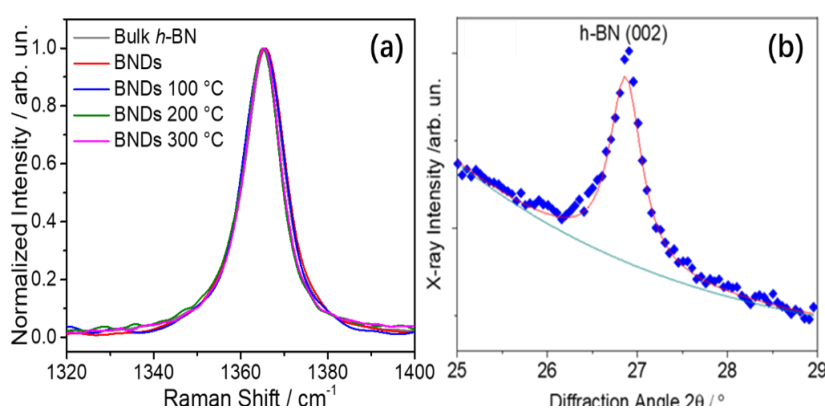
Figure 5.2.2 (a) Raman spectra in 1330 – 1400 cm^{-1} of bulk h-BN (as reference), as-prepared BN dots and thermally treated dots. (b) XRD pattern of the as-prepared dots.

5.2.3.2. Optical properties

To evaluate how a thermal treatment affects the optical properties of BN dots, the fluorescence and absorption spectra have been acquired from aqueous solutions of the as-prepared sample and samples treated in air upon 100, 200, and 300 °C. **Figure 5.2.3** describes both 3D excitation-emission-intensity and 2D photoluminescence (PL) spectra of these BN products, where double well-defined emissions have been observed in the pristine dots with the change of excitation wavelength from 250 to 400 nm. In **Figure 5.2.3a**, the first emission appears in the ultraviolet region of 300 – 380 nm under the excitation range in 250 – 290 nm, showing the PL maxima at 325 nm upon excitation of 260 nm. The second band is located in the blue area extending from 380 to 520 nm under excitation light at 290 – 400 nm, with the emission maxima at 420 nm using 310 nm excitation. As seen in **Figure 5.2.3b-c**, the thermal treatment of dots in air up to 200 °C will cause the fluorescent quenching of the UV emission and the enhanced blue

luminescence, accompanied with an overlap of two-color emissive areas. A higher temperature, i.e. 300 °C (**Figure 5.2.3d**), will lead to an obvious PL decline of the BN dots.

It is worth highlighting that the UV luminescence can only be realized after both thermal treating and sonication in Brønsted acid, whilst cannot be detected if the bulk crystals are exclusively subjected to either heating or sonicating process (see **Figure 5.2.4**). In another hand, the exfoliated *h*-BN systems have already been reported to show a visible emission due to the presence of defects, especially, the oxygen impurities. A similar work has already been detailly discussed in ***Section 4.1***, which involves a temperature-dependent and defect-assisted blue luminescence of water-exfoliated *h*-BN nanosheets.
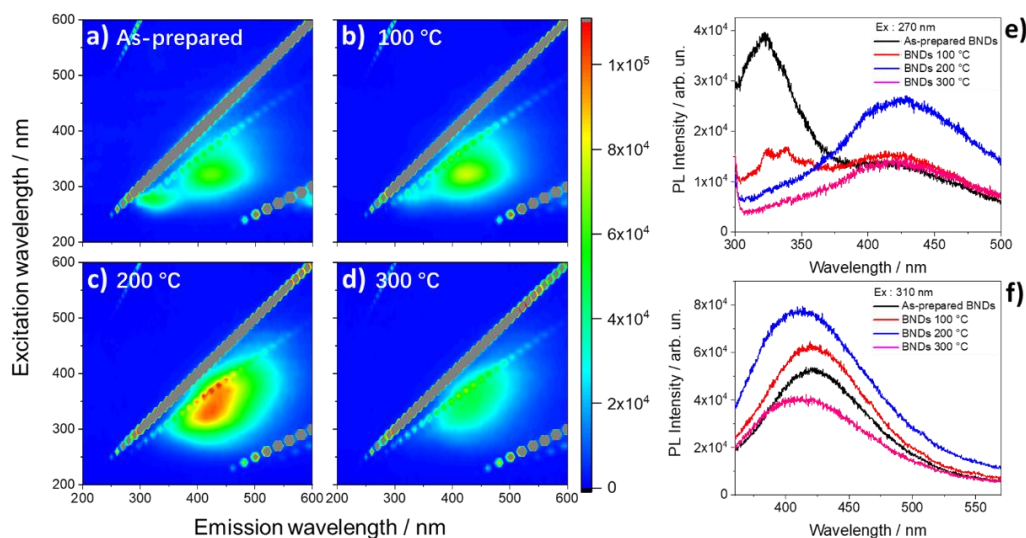
Figure 5.2.3 (a-d) The 3D excitation-emission-intensity and (e-f) 2D photoluminescence spectra of the prepared and thermal-treated BN dots.
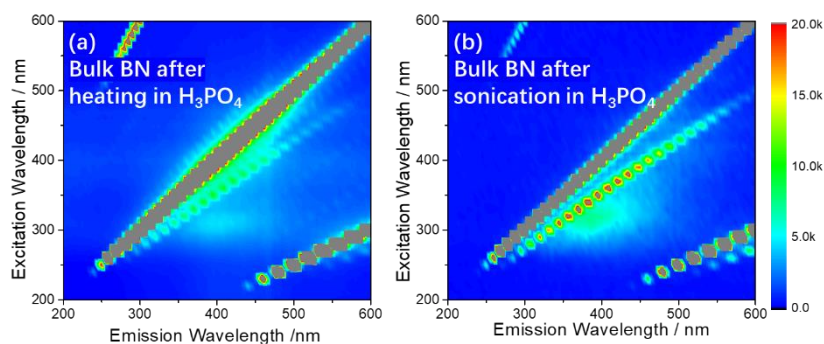
Figure 5.2.4 The 3D excitation-emission-intensity spectra of bulk BN (a) after heating at 200 °C in H_3PO_4 without sonication, (b) after sonication for 15 h in H_3PO_4 without heating.

Figure 5.2.5 shows the fluorescent decay curves of the BN dots in aqueous solutions; **Table 5.2.1** summarizes the fitted results of the time-resolved emission via a double-exponential function. The average lifetime of blue emission is calculated to be ~3.7 ns, suggesting that the lifetimes are typically unaffected by thermal treatments. It has been confirmed that heating the BN dots at 200 °C can lead to a strong emissive quenching of the PL located at 325 nm and an enhancement of the emission centered at 420 nm. The thermal performances of blue luminescence are in good accordance with the findings in *Section 4.1*.
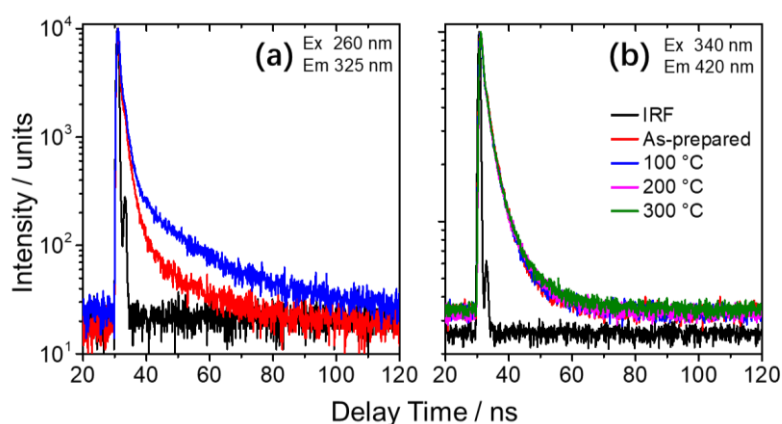
Figure 5.2.5 Fluorescence lifetime curves of (a) UV and (b) blue emissions in the as-prepared and thermal-treated BN dots.

Table 5.2.1 Fluorescence lifetime fitted results via a double-exponential-type formula.

(a) λ_{ex} = 260 nm, and λ_{em} = 325 nm

Samples	τ_1 (ns)	α_1	τ_2 (ns)	α_2	τ_{ave} (ns)	χ^2
As-prepared	1.72 ± 0.05	0.96	13.20 ± 1.12	0.04	2.18	1.05
100 °C	1.67 ± 0.05	0.92	15.71 ± 0.68	0.08	2.78	1.03

(b) λ_{ex} = 340 nm, and λ_{em} = 420 nm

Samples	τ_1 (ns)	α_1	τ_2 (ns)	α_2	τ_{ave} (ns)	χ^2
As-prepared	2.75 ± 0.28	0.74	6.91 ± 0.36	0.26	3.83	1.04
100 °C	2.56 ± 0.21	0.76	7.37 ± 0.34	0.24	3.71	1.04
200 °C	2.32 ± 0.04	0.74	7.50 ± 0.52	0.26	3.67	0.97
300 °C	2.43 ± 0.17	0.77	7.80 ± 0.32	0.23	3.67	1.02

The UV emission deserves further analysis. Museur et al. have observed a broad PL band maximized at ~3.9 eV in polycrystalline BN materials under the condition of room temperature, and also a sharper emission at ~5.5 eV in high-energy regions.[56] The authors have assigned the luminescence to the donor-acceptor pairs of localized centers in correspondence of defects coupled to the distal lattice points, where the defects can be B/N vacancies as well as their coupling with oxygen impurities. Similarly, *h*-BN with point-defect emission at ~5.27 eV has been grown using molecular beam epitaxy (MBE) at a high temperature (1850 °C).[156] In a very recent report, Stone–Wales defects, produced through rotating a B-N pair by 90 °, have also been accounted as a possible origin of UV emission in *h*-BN.[157] In our case, the UV luminescence triggered at 260 nm possibly corresponds to the particular structural defects which could be present in BN crystal lattice. A peculiar correlation has been well built between fluorescence and structural properties of our BN dots according to the following infrared absorption spectra and theoretical calculations (*vide infra*).

Figure 5.2.6a reports their corresponding UV-Vis absorption spectra, performed in aqueous solution using a comparable concentration. The dots are characterized by an intense absorption band in deep UV region with a broad absorption tail extending to the visible range that increases in intensity after thermal treating. The high-energy absorption at around 6 eV is assigned to the intrinsic band-to-band transition of the *h*-BN materials, and the thermal treatments cause a drop in intensity of this band. According to our observation, the dispersibility of BN dots still remains stable after the heating process. Therefore, it is reasonable to attribute the decreasing UV absorption to a possible alteration in intrinsic structures of the dots.

The energy gap (E_g) has been evaluated using the Tauc method according to the corresponding enlarged UV-Vis spectra (see **Figure 5.2.6b** and **Supplementary Note I**). The E_g value of the as-prepared dots is calculated to be ~5.47 eV and shifts towards higher values as 5.58, 5.69, and 5.80 eV as a function of the thermal treatment at 100, 200, and 300 °C, respectively. The intragap states of defects in *h*-BN generally arise as an absorption tail in its proximity of bandgap. The annealing effects and the resulting reduction of the structural disorder have allowed observing a shift of the absorption

edge to higher-energy, which has already been reported in *h*-BN films synthesized by metal-organic chemical vapor deposition (MOCVD) method.[158] In contrast, the annealing treatments lead to a rise of the absorption bands at visible wavelengths because of the oxidation of persistent defects in *h*-BN structure during the heating in air.[159]
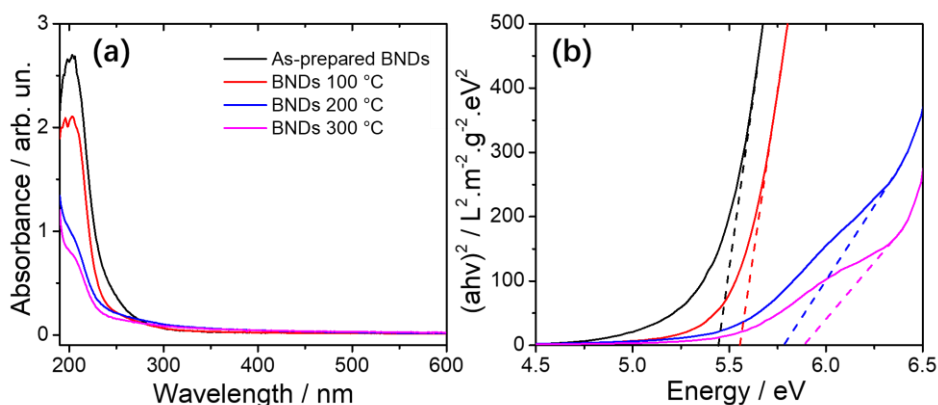
Figure 5.2.6 (a) UV-Vis absorption spectra and (b) the corresponding evaluation of E_g values of the as-prepared and thermal-treated BN dots.

5.2.3.3. Chemical composition

FTIR spectroscopy has been analyzed to explore the chemical groups and potential defects in the synthesized *h*-BN products. In **Figure 5.2.7a**, the characteristic vibrational bands at 1375 and 815 cm^{-1} represent the in-plane B-N stretching (E_{1u}) and the out-of-plane B-N-B bending (A_{2u}) vibrations, respectively. Interestingly, the two modes of nano-sized BN dots show a much narrower full width at half maximum (FWHM) with respect to bulk counterparts. Although this comparison has been ignored in many papers, the same phenomenon could be frequently encountered from their reported IR data including both 2D sheets[160-162] and 0D dots.[38, 62, 163-164] In the thesis, this problem is not addressed with a specific answer, but a reasonable suppose is that the dimension decrease, as well as the edge effects, will bear on the vibrational distributions of B-N and B-N-B bonds. Meanwhile, the intensity ratio of the two bands in bulk *h*-BN (I_{1375}: I_{815}, 3.07) is much smaller than that in BN dots (I_{1375}: I_{815}, 5.07), which is likely attributed to the strong exfoliation effect and a correlation of the modification in interplanar interactions.

The infrared spectrum of BN dots is also demonstrated with some modes in lower wavenumbers. The range of 400 – 750 cm^{-1} is induced by the oxidized BN structure, e.g. B-O and B-OH vibrations. The signals in 850 – 1250 cm^{-1} region can be attributed to the N-B-O and B-O stretching,[165] which are closed to the P-OH and P=O stretching vibrations (970 and 1210 cm^{-1}) in H$_3$PO$_4$ ATR-FTIR spectrum.[166] Actually, the H$_3$PO$_4$ composition can be excluded in the produced dots according to the infrared variation, and the Raman spectra do not report any fingerprints of phosphoric acid.
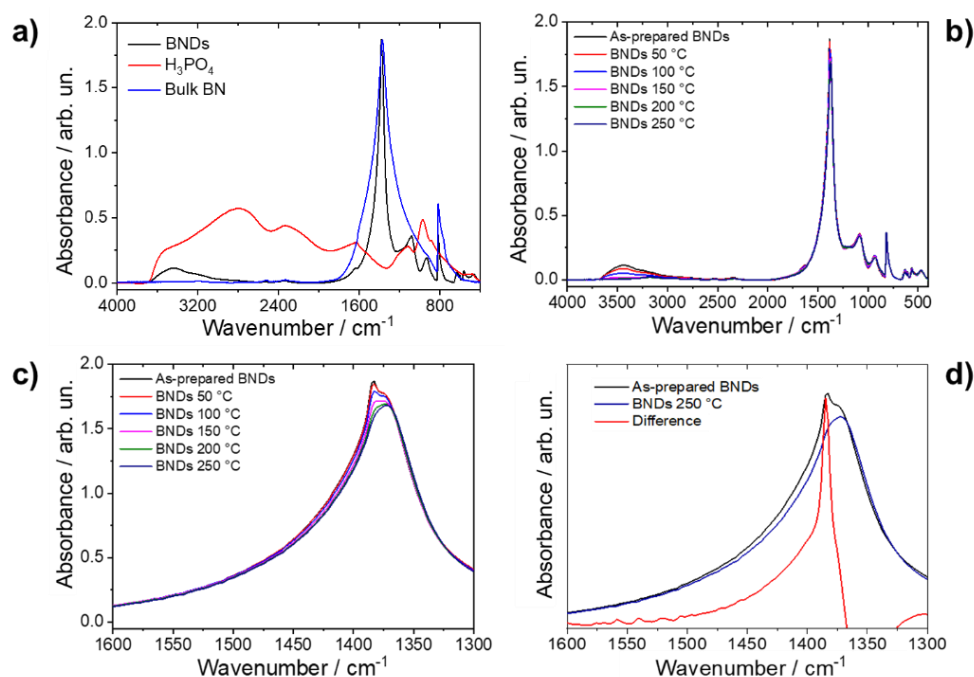
Figure 5.2.7 (a) FTIR spectra of BN dots, bulk *h*-BN, and H$_3$PO$_4$ (liquid, by ATR mode). (b) *In situ* FTIR spectra of BN dots as a function of temperature up to 250 °C and (c) their enlarged region at 1300 – 1600 cm^{-1}. (d) The spectral difference between as-prepared and treated samples.

Figure 5.2.7b shows the *in situ* spectra of BN dots as a function of temperature by heating from room condition to 250 °C, and Figure 5.2.7c reports a magnified region of 1300 – 1600 cm^{-1} to highlight a significant thermal-induced change. Two overlapped convolutions have contributed to this vibrational region: one at 1375 cm^{-1} from BN E_{1u} and another located at 1384 cm^{-1}. The latter mode shows a temperature-dependent intensity and even disappears after the 250 °C process. Herein, a spectral difference curve is captured between the as-prepared and 250 °C treated samples (see the red line in Figure 5.2.7d), which exhibits a sharp vibration with its maxima at 1385 cm^{-1}. An important story is that this sharp mode can be well correlated with the UV emission at

325 nm, because the annealing process has promoted a consistent decrease of both luminescence and IR intensities. A direct correspondence is thus allowed building between the two physical aspects.

To the best of our knowledge, the split of IR E_{1u} has been observed from BN nanoparticles in a few articles. For instance, a significant split at around 1380 – 1400 cm^{-1} has been attributed to the edge oxidization of BN dots, which are produced by potassium-assisted thermally cracking h-BN and following a reaction with ethanol/water solution.[36] This synthesis has been affected by the presence of carbon contamination. Similarly, the BN dots synthesized by hydrothermal reaction of boric acid and urea have shown the splitting vibrations at 1385 and 1439 cm^{-1} because of edge oxidation.[46] High-temperature treating h-BN and ferrite particles can introduce extensive physical defects, then a water-vapor exposure allows the saturation of -OH groups.[39] The E_{1u} bond of edge-hydroxylated BN dots has shown a marked shift toward high-wavenumbers with respect to the flakes. Two fluorescent emissions have been detected at about 320 and 450 nm from the resulting hydroxylated dots.[39] Coupled with these reports, our findings have excluded the carbon-doping and phosphorus functionalization as reasons of the optical and vibrational features of the prepared BN dots.

Herein, the infrared split at 1300 – 1600 cm^{-1} area primarily involves the B-N E_{1u} mode and the intrinsic hexagonal crystal structure. We presume that a characteristic defect and the consequent local deformation of the lattice can influence the B-N in-plane vibrational performances. The characteristic defect should be responsible for the UV emission and associated with the saturated -OH and -H groups. DFT calculations have reported that the pentagon–heptagon Stone–Wales (SW) defects are optically active in the UV region with an optical transition at 4.08 eV.[157] In our case, two weaker vibrations of B-H stretching have been observed at 2520 and 2425 cm^{-1}, and the latter mode decreases in intensity as the thermal process.

The detailed information of O-H and N-H bonds has been studied according to in-situ IR data in 3800 – 2600 cm^{-1} (see **Figure 5.2.8**), where the spectra can be deconvoluted into three chemical components. The deconvoluted peaks at 3450 and

2890 cm^{-1} are caused by hydrogen-bonded O-H and absorbed O-H at the surface. The heating process results in a rapid decline of the high-frequency component and a relatively slower decrease of the one in lower wavenumbers. It also indicates that the B-OH groups are mainly in an isolated state after treating at higher temperatures. The middle deconvoluted band at 3180 cm^{-1} is assigned to the N-H stretching absorption, which shows a similar decreasing trend in intensity to B-OH deconvolution. Upon annealing to 200 and 250 °C, minor changes are presented in the spectra.
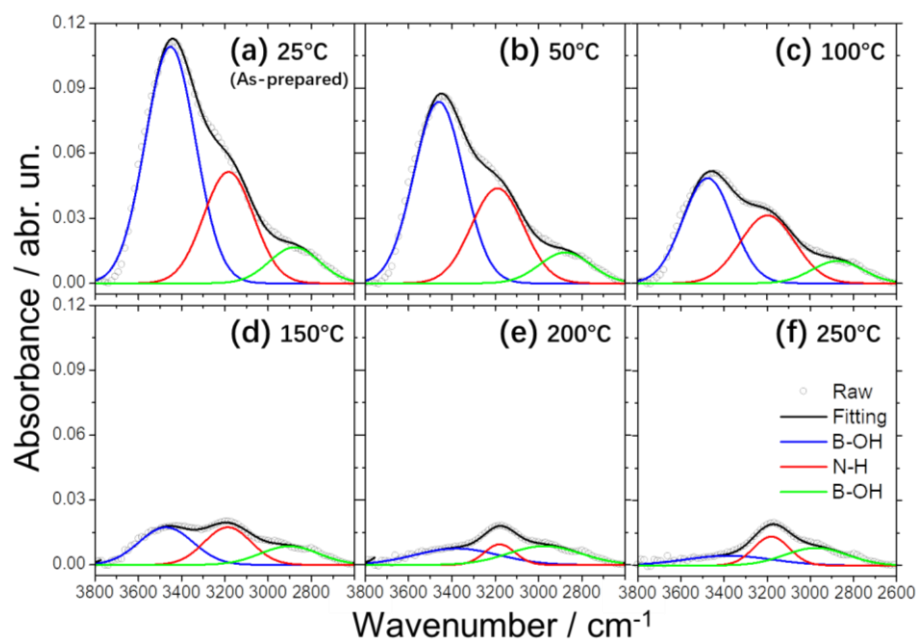
Figure 5.2.8 *In situ* FTIR spectra in the 3800 – 2600 cm^{-1} range of the as-prepared BN dots as function of different thermal temperatures: (a) 25, (b) 50, (c) 100, (d) 150, (e) 200, and (f) 250 °C.

In **Figure 5.2.9**, TGA-DTA data have been analyzed by coupling with the *in situ* FTIR spectra as a function of temperature. Two endothermic reactions have been observed: (i) The first step from 25 to 90 °C is caused by the loss of molecular adsorption of water in BN products, coupled with a 9.4% decline in weight; (ii) The second one from 90 to 300 °C exhibits complicated chemical reactions with a sharp peak at 180 °C and a wide peak at 215 °C, showing a 16.2% weight loss, which involves a progressive condensation of B-OH and the forming N-B-O structures. Furthermore, when the temperature is higher than 300 °C, strong oxidation can lead to the formation of boroxyl rings structures.
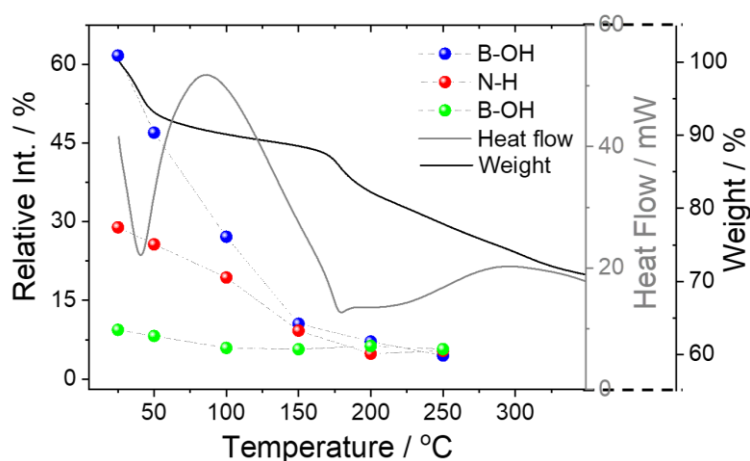
Figure 5.2.9 The relative intensity of three components of in-situ infrared spectra, accompanied with TGA and heat flow curves, as a function of increasing temperature.

5.2.3.4. Theoretical calculations

For a better understanding of the experimental results, DFT calculations have been applied to evaluate the impact of SW defects on the structural and optical features of a *h*-BN cluster system. A simplified model is built as a hexagonal-shaped BN monolayer, possessing a total of 180 atoms, consisting of 61 rings and edges saturated with protons. The SW defective structure is introduced by inserting a pentagon-heptagon as cause of a B-N couple rotation, making B-B and N-N couples keep a constant the atom sum in the final cluster.

A neutral charge configuration has been used for the calculations of defects via the following equation:[123]

$$E_{form} = E_D(q) - E_{BN} + n_i\mu_i + q(E_{VBM} + E_F)$$ **Equ. 5.2.1**

where $E_D(q)$ is the energy of charge state q in the defective cluster, E_{BN} is the energy in the pristine BN cluster, n_i is the number of exchanged species, and μ_i is the chemical potential for the related reservoir. E_F represents the Fermi energy and E_{VBM} refers to the maximum energy of the valence band. With the assumption of $q = 0$, the equation reduces into the difference of the formation energies between two clusters. The defect-free cluster shows an intense absorption at 205 nm (see **Figure 5.2.10a**) in good agreement with the experimental data of bulk BN.[52, 167] The corresponding optimized

97

structure displays the B-N bonds with a length of 1.446 Å at the center and 1.419 Å at the edge, which accord well with the reported data of small clusters.

To study the effect of SW-defect on the optical absorption, a pentagon–heptagon geometry is introduced into the core of the cluster and relaxed to the configuration with lower energy. The calculations have been carried out with the presence of single, double, and three defects. As seen in **Figure 5.2.10a**, the strong band-to-band transition shows a red-shift to 227 nm in BN(SW), and a low-energy transition appears at 283 nm, which is enhanced in BN(2SW) and BN(3SW). This effect can be attributed to the defect-related deformation of structure that can bend the planar geometry of *h*-BN cluster (see **Figure 5.2.10b**). It is worth stating that the simulated optical data is in good accordance with the experimental results. For example, both the absorption band at around 227 nm (**Figure 5.2.6**) and the excitation band of UV fluorescence (**Figure 5.2.3**) agree well with the calculated band-to-band and low-energy transitions in the defective BN systems, respectively.
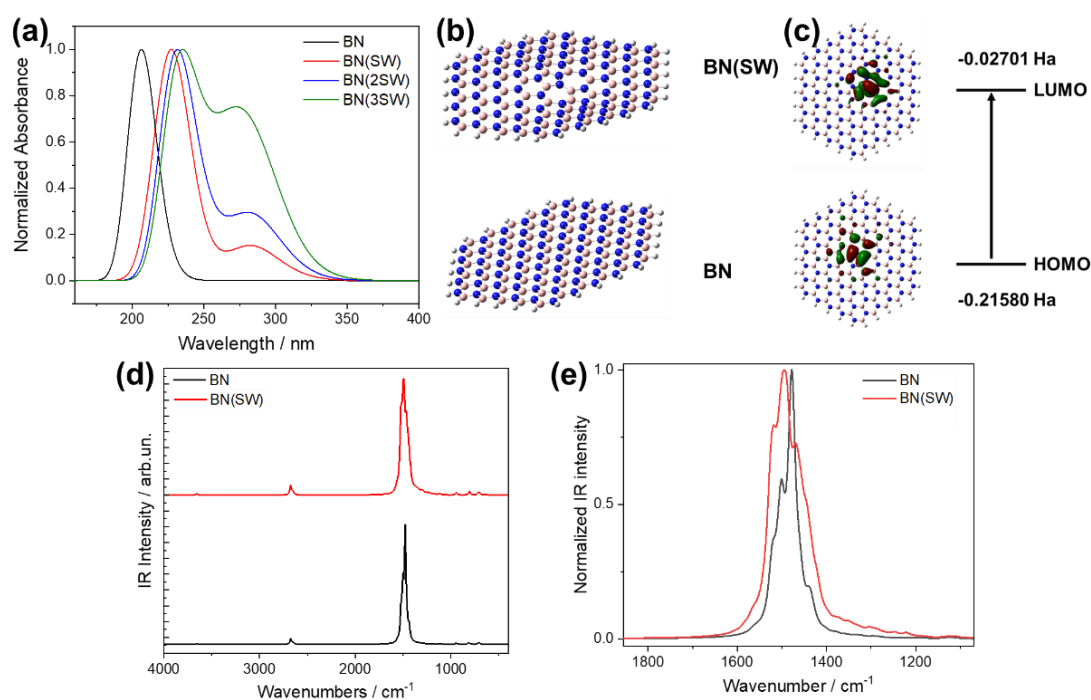
Figure 5.2.10 (a) Computed UV–Vis absorption spectra of pristine (BN) and defective *h*-BN (BN(SW)) clusters. (b) Representations of the optimized BN and BN(SW) structures. (c) Representation of HOMO-LUMO of the computed defects. (d) Calculated IR spectra of BN and BN(SW) clusters, and (e) the enlarged infrared region in $1100 – 1900$ cm^{-1}.

Figure 5.2.10c describes the HOMO-LUMO transition of BN(SW) along with the corresponding molecular orbital representations, which show a strong localization of the charge distribution around the SW defect. **Figure 5.2.10d** shows the calculated IR spectra pristine BN and BN(SW), and **Figure 5.2.10e** enlarges the region around B-N E_{1u} wavenumbers. Although there are some limitations in the simulated model (e.g. single layer, small dimension, and hydrogen saturation), the calculated infrared results are well qualitative with respect to the experimental data. Due to the effect of SW defects, a remarkable modulation of in-plane BN bending has been observed, which can be assigned to the strong removal of BN planarity.

Furthermore, we have estimated the impact of the position of SW defect in the cluster. As shown in **Figure 5.2.11**, the formation energy is 6.35 or 5.45 eV when the defect is at the center (BN(SW)$_c$) or edge (BN(SW)$_e$). It suggests that it is more favorable to facilitate the generation of SW defects at the edge of BN nanodots. In spite of the overestimation for vibrational frequency, the calculated optical transitions match well with the trend observed in the experimental findings. Thus, it can corroborate the hypothesis that the localized SW defects are the possible source of UV properties from the as-prepared BN dots.
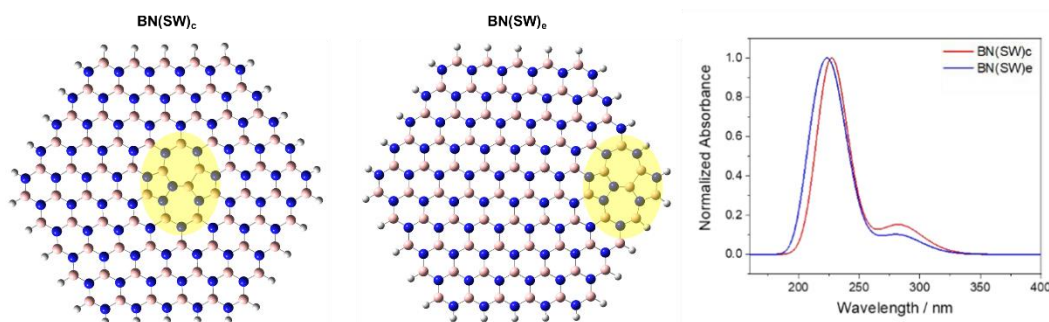
Figure 5.2.11 Relaxed structure and simulated UV-Vis absorption spectra of defective *h*-BN clusters as a function of SW defect position: center (BN(SW)$_c$) and edge (BN(SW)$_e$).

According to the above discussions, the synthesis process of BN dots has been summarized in **Scheme 5.2.2**, as well as the effect of Brønsted acid. Firstly, the bulk *h*-BN crystals can be dispersed in the concentrated acid by minutes of fast ultra-sonication. Then the thermal treatment can promote the intercalation and interaction of H_3PO_4 with the BN structure, where the heating temperature of 200 °C is close to the boiling point

of 212 °C. Meanwhile, the resulting strong oxidation gives rise to the breaking of B-N bonds, especially at the edge and exposed surface. The generated unsaturated bonds can service as anchor sites for -OH groups and protons. At the end of further long-time sonication, the BN crystal appears highly defective structure as demonstrated by the formation of UV emission.
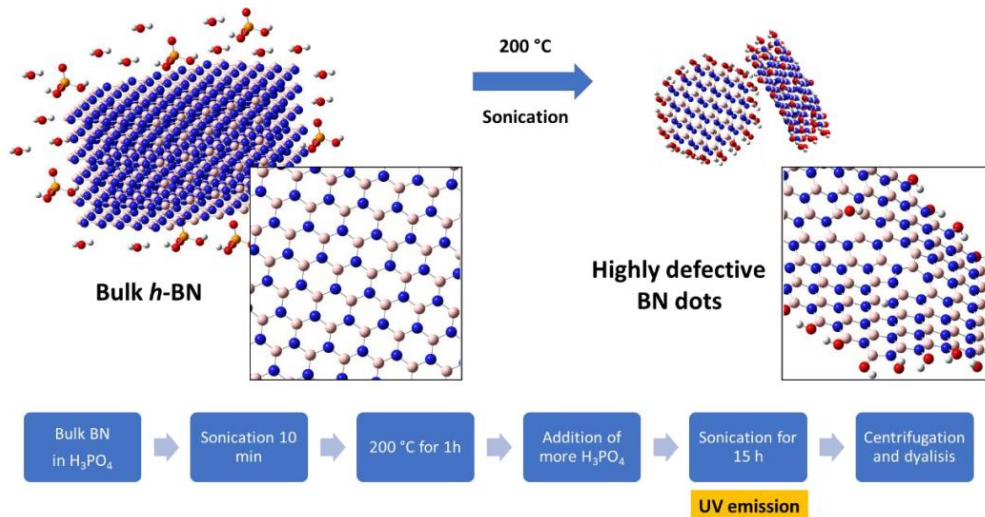
Scheme 5.2.2 Schematic illustration on synthesis process of BN nanodots by Brønsted acid etching.

5.2.4. Conclusions

h-BN nanodots with highly defective structures have been fabricated via a top-down route by oxidizing and etching their bulk counterparts in concentrated Brønsted acid. The resulted products show a two-color emission located at the UV and visible regions, respectively. The visible luminescence can be attributed to the hydroxyl groups and oxidation-related defects. The emission at 325 nm shows a serious quenching after thermal treatment in air. Meanwhile, a new sharp vibration has been detected in the region of in-plane E_{1u} wavenumbers, which decreases in intensity and finally disappears as a function of heating temperature up to 250 °C. Coupled with DFT theoretical analysis, the vibrational mode can be correlated with a characteristic B-N stretching, i.e. SW defects, as causes of the emergence of UV emission.

Chapter 6. Conclusions

This Chapter has summarized the main conclusions in the thesis. Meanwhile, a short perspective is shown to discuss the future development of hexagonal boron nitride (*h*-BN) nanomaterials.

6.1. Summary

This **Thesis** has mainly been devoted to exploring the correspondence between structure defects and optical properties of *h*-BN materials by synthesizing nanosheets and nanodots. Carbon-free routes have been performed to produce BN sheets and dots, which can avoid the interference of carbon impurities and introduce special defects. It creates the conditions to understand the possible defect-property causalities in *h*-BN systems.

In section of *h*-BN nanosheets, a kind of defective sheets can be produced via sonication-assisted exfoliation of bulk BN in water phase, which show a blue emission (see **Figure 6.1a**). When the exfoliation is carried out in N-methyl-2-pyrrolidone (NMP) or dimethyl sulfoxide (DMSO), relatively defect-free BN sheets can be obtained without the visible fluorescence of the former. It suggests that the blue luminescence depends on the presence of structural defects during synthesis. The infrared vibrational spectroscopy has allowed a good correlation between the presence of hydroxyl groups in the sheets and temperatures of thermal treatment. Furthermore, the introduced defects can also increase the optical absorption of *h*-BN sheets in the UV-Vis region, which is also supported by theoretical calculations.

Subsequently, sol-gel and self-assembly methods are used to respectively incorporate the defect-free and defective BN nanosheets into titania (TiO_2) mesoporous films to form heterostructures (see **Figure 6.1b**). Neither the bare nor defective *h*-BN sheets do not show any photocatalytic response but can promote the crystallization of TiO_2 anatase phase. Significantly, the defects of *h*-BN can increase the absorbance in

ultraviolet radiation A, consequently enhancing the photocatalysis of the heterojunction film under 365 nm with respect to the pure TiO_2 mesoporous film.
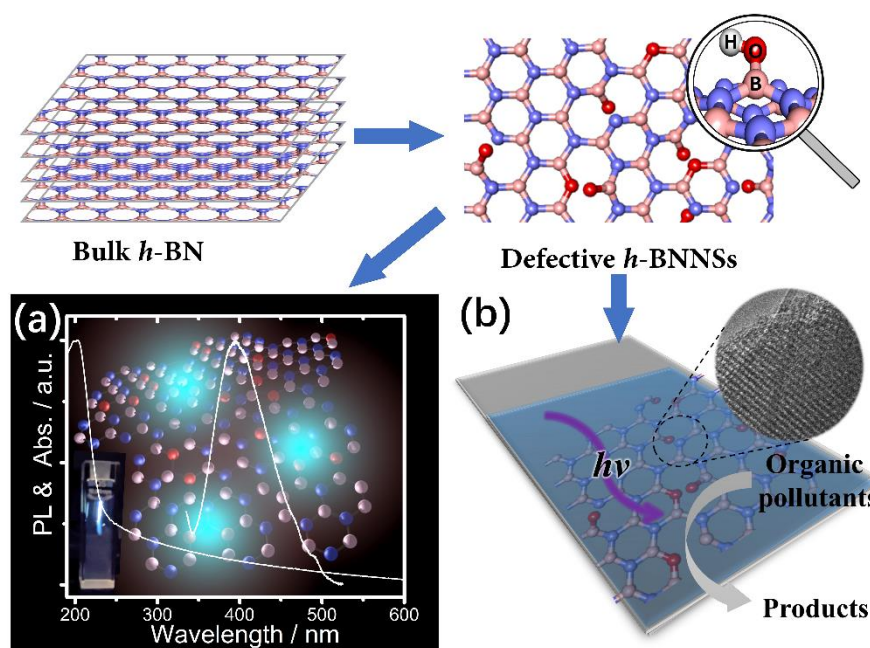
Figure 6.1 Defective *h*-BNNSs synthesized via sonication-assisted exfoliation. (a) Defect-assisted photoluminescence of *h*-BNNSs, (b) BN-TiO₂ film heterostructure with an enhanced photocatalysis.

In section of BN dots, both bottom-up and top-down methods have been used to synthesize fluorescent BN dots, where a carbon-free process can allow reconsidering the correspondence of defective structure and optical properties. In the bottom-up case, the BN dots have been prepared with boric acid and ammonium as precursors via hydrothermal method (see **Figure 6.2a**). The characterizations of structure and composition have shown that the produced nanoparticles possess a boron-oxynitride structure only with a limited amount of *h*-BN crystalline phase. Interestingly, two-color emissions can be detected at 390 and 470 nm, respectively, which are corrected to network or BO_x^- defects in the oxynitride structure.

Generally, bottom-up routes cannot allow producing pure BN dots with a good *h*-BN phase. Therefore, in the top-down case, bulk *h*-BN can be cut into nanosized dots through edge etching in phosphoric acid by the combination of sonication and thermal treatments, consequently creating defective BN nanodots (**Figure 6.2b**). Significantly, the synthesized *h*-BN dots not only show general blue fluorescence but also a new

emission in UV region that is correlated to a characteristic infrared-active vibration. Structural and optical characterizations have shown the correspondence of the visible emission and the hydroxyl covalent functionalization in the produced *h*-BN structure. Meanwhile, quantum chemistry calculations have been used to evaluate Stones-Wales defects as possible causes of the UV emission and the corresponding vibrational properties.
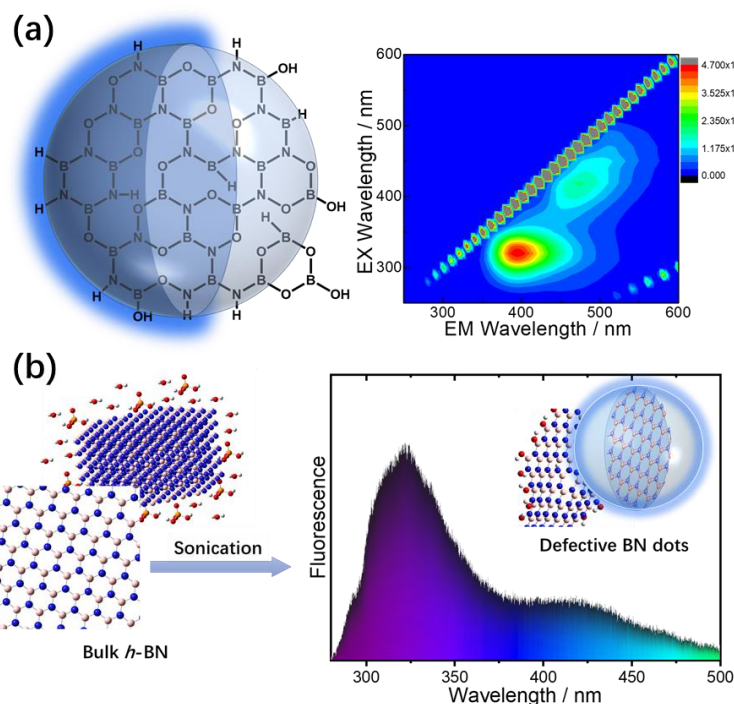
Figure 6.2 BN dots synthesized via (a) bottom-up and (b) top-down routes, respectively.

6.2. Outlook

The past decades have witnessed the great efforts of the scientific community made for BN-related materials. However, there are still many challenges to address and basic studies to exploit.

An important issue is related to the manufacturing process of *h*-BN, for example, reproducibility and controllability. The current techniques can still not allow producing *h*-BN sheets with a precisely controlled layer number. In general, the thickness and dimension are determined according to the corresponding average values. It means that

the applications, where strict control of structure and property is not required, will be more feasible.

Many current scattered studies have been mainly devoted to improving application behaviors, where the internal sciences are usually far from reaching. One suggestion is that more theoretical and experimental works should focus on the mechanism through which the defects contribute to the functional properties. On the contrary, some cases strongly require high-quality *h*-BN layers because a defect-free structure allows optimizing their thermal conductivity and electrical insulation.

A significant direction is to develop advanced technologies which enable designing property-tailored *h*-BN systems. In almost all fields of material science, feasible routes are necessary to translate the findings in laboratories into engineering in industries.

Reference

(1) Haubner, R.; Wilhelm, M.; Weissenbacher, R.; Lux, B. Boron nitrides—properties, synthesis and applications. In *High Performance Non-Oxide Ceramics II*, Jansen, M., Ed. Springer: 2002; Vol. 102, pp 1-45.

(2) Zhang, X.; Meng, J. Chapter 4 - Recent progress of boron nitrides. In *Ultra-Wide Bandgap Semiconductor Materials*, Liao, M.; Shen, B.; Wang, Z., Eds. Elsevier: 2019; pp 347-419.

(3) Weng, Q.; Wang, X.; Wang, X.; Bando, Y.; Golberg, D. Functionalized hexagonal boron nitride nanomaterials: emerging properties and applications. *Chem. Soc. Rev.* **2016**, *45*, 3989-4012.

(4) Ye, L.; Liang, F.; Zhao, L.; He, X.; Fang, W.; Chen, H.; Wang, X.; Wu, J.; An, S. Catalyzed synthesis of rhombohedral boron nitride in sodium chloride molten salt. *Ceram. Int.* **2016**, *42*, 11626-11633.

(5) Samantaray, C. B.; Singh, R. N. Review of synthesis and properties of cubic boron nitride (c-BN) thin films. *Int. Mater. Rev.* **2005**, *50*, 313-344.

(6) Liu, Y.; Zhan, G.; Wang, Q.; He, D.; Zhang, J.; Liang, A.; Moellendick, T. E.; Zhao, L.; Li, X. Hardness of polycrystalline wurtzite boron nitride (wBN) compacts. *Sci. Rep.* **2019**, *9*, 10215.

(7) Guo, Q.; Xie, Y.; Yi, C.; Zhu, L.; Gao, P. Synthesis of ultraviolet luminescent turbostratic boron nitride powders via a novel low-temperature, low-cost, and high-yield chemical route. *J. Solid State Chem.* **2005**, *178*, 1925-1928.

(8) Hong, S.; Lee, C.-S.; Lee, M.-H.; Lee, Y.; Ma, K. Y.; Kim, G.; Yoon, S. I.; Ihm, K.; Kim, K.-J.; Shin, T. J.; Kim, S. W.; Jeon, E.-c.; Jeon, H.; Kim, J.-Y.; Lee, H.-I.; Lee, Z.; Antidormi, A.; Roche, S.; Chhowalla, M.; Shin, H.-J.; Shin, H. S. Ultralow-dielectric-constant amorphous boron nitride. *Nature* **2020**, *582*, 511-514.

(9) Ren, J.; Stagi, L.; Innocenzi, P. Hydroxylated boron nitride materials: from structures to functional applications. *J. Mater. Sci.* **2021**, *56*, 4053-4079.

(10)Ren, J.; Stagi, L.; Malfatti, L.; Carbonaro, C. M.; Granozzi, G.; Calvillo, L.;

Garroni, S.; Enzo, S.; Innocenzi, P. Engineering UV-emitting defects in h-BN nanodots by a top-down route. *Appl. Surf. Sci.* **2021**, *567*, 150727.

(11) Zheng, Z.; Cox, M.; Li, B. Surface modification of hexagonal boron nitride nanomaterials: a review. *J. Mater. Sci.* **2018**, *53*, 66-99.

(12) Li, N.; Guo, X.; Yang, X.; Qi, R.; Qiao, T.; Li, Y.; Shi, R.; Li, Y.; Liu, K.; Xu, Z.; Liu, L.; García de Abajo, F. J.; Dai, Q.; Wang, E.-G.; Gao, P. Direct observation of highly confined phonon polaritons in suspended monolayer hexagonal boron nitride. *Nat. Mater.* **2021**, *20*, 43-48.

(13) Stagi, L.; Ren, J.; Innocenzi, P. From 2-D to 0-D boron nitride materials, the next challenge. *Materials* **2019**, *12*, 3905.

(14) Pacilé, D.; Meyer, J. C.; Girit, Ç. Ö.; Zettl, A. The two-dimensional phase of boron nitride: Few-atomic-layer sheets and suspended membranes. *Appl. Phys. Lett.* **2008**, *92*, 133107.

(15) Li, L. H.; Chen, Y.; Behan, G.; Zhang, H.; Petravic, M.; Glushenkov, A. M. Large-scale mechanical peeling of boron nitride nanosheets by low-energy ball milling. *J. Mater. Chem.* **2011**, *21*, 11862-11866.

(16) Lee, D.; Lee, B.; Park, K. H.; Ryu, H. J.; Jeon, S.; Hong, S. H. Scalable exfoliation process for highly soluble boron nitride nanoplatelets by hydroxide-assisted ball milling. *Nano Lett.* **2015**, *15*, 1238-1244.

(17) Liu, B.; Yan, S.; Zhang, A.; Song, Z.; Sun, Q.; Huo, B.; Yang, W.; Barrow, C. J.; Liu, J. Insight into catalytic mechanisms for the reduction of nitrophenol via heterojunctions of gold nanoclusters on 2D boron nitride nanosheets. *ChemNanoMat* **2019**, *5*, 784-791.

(18) Wang, Y.; Low, Z.-X.; Kim, S.; Zhang, H.; Chen, X.; Hou, J.; Seong, J. G.; Lee, Y. M.; Simon, G. P.; Davies, C. H. J.; Wang, H. Functionalized boron nitride nanosheets: A thermally rearranged polymer nanocomposite membrane for hydrogen separation. *Angew. Chem. Int. Ed.* **2018**, *57*, 16056-16061.

(19) Shaybanizadeh, S.; Najafi Chermahini, A. Fabricating boron nitride nanosheets from hexagonal BN in water solution by a combined sonication and thermal-assisted hydrolysis method. *Ceram. Int.* **2021**, *47*, 11122-11128.

(20)Lin, Y.; Williams, T. V.; Xu, T.-B.; Cao, W.; Elsayed-Ali, H. E.; Connell, J. W. Aqueous dispersions of few-layered and monolayered hexagonal boron nitride nanosheets from sonication-assisted hydrolysis: Critical role of water. *J. Phys. Chem. C* **2011**, *115*, 2679-2685.

(21)Nie, X.; Li, G.; Jiang, Z.; Li, W.; Ouyang, T.; Wang, J. Co-solvent exfoliation of hexagonal boron nitride: Effect of raw bulk boron nitride size and co-solvent composition. *Nanomaterials* **2020**, *10*, 1035.

(22)Ren, J.; Stagi, L.; Carbonaro, C. M.; Malfatti, L.; Casula, M. F.; Ricci, P. C.; Del Rio Castillo, A. E.; Bonaccorso, F.; Calvillo, L.; Granozzi, G.; Innocenzi, P. Defect-assisted photoluminescence in hexagonal boron nitride nanosheets. *2D Mater.* **2020**, *7*, 045023.

(23)Rosely, C. V. S.; Shaiju, P.; Gowd, E. B. Poly(l-lactic acid)/boron nitride nanocomposites: Influence of boron nitride functionalization on the properties of poly(l-lactic acid). *J. Phys. Chem. B* **2019**, *123*, 8599-8609.

(24)Jiang, F.; Cui, S.; Song, N.; Shi, L.; Ding, P. Hydrogen bond-regulated boron nitride network structures for improved thermal conductive property of polyamide-imide composites. *ACS Appl. Mater. Interfaces* **2018**, *10*, 16812-16821.

(25)Deshmukh, A. R.; Jeong, J. W.; Lee, S. J.; Park, G. U.; Kim, B. S. Ultrasound-assisted facile green synthesis of hexagonal boron nitride nanosheets and their applications. *ACS Sustainable Chem. Eng.* **2019**, *7*, 17114-17125.

(26)Ren, J.; Stagi, L.; Malfatti, L.; Garroni, S.; Enzo, S.; Innocenzi, P. Boron nitride–titania mesoporous film heterostructures. *Langmuir* **2021**, *37*, 5348-5355.

(27)Khan, M. H.; Liu, H. K.; Sun, X.; Yamauchi, Y.; Bando, Y.; Golberg, D.; Huang, Z. Few-atomic-layered hexagonal boron nitride: CVD growth, characterization, and applications. *Mater. Today* **2017**, *20*, 611-628.

(28)Song, X.; Gao, J.; Nie, Y.; Gao, T.; Sun, J.; Ma, D.; Li, Q.; Chen, Y.; Jin, C.; Bachmatiuk, A.; Rümmeli, M. H.; Ding, F.; Zhang, Y.; Liu, Z. Chemical vapor deposition growth of large-scale hexagonal boron nitride with controllable orientation. *Nano Res.* **2015**, *8*, 3164-3176.

(29)Gao, R.; Yin, L.; Wang, C.; Qi, Y.; Lun, N.; Zhang, L.; Liu, Y.-X.; Kang, L.; Wang,

X. High-yield synthesis of boron nitride nanosheets with strong ultraviolet cathodoluminescence emission. *J. Phys. Chem. C* **2009**, *113*, 15160-15165.

(30) Wang, X.; Zhi, C.; Li, L.; Zeng, H.; Li, C.; Mitome, M.; Golberg, D.; Bando, Y. "Chemical blowing" of thin-walled bubbles: High-Throughput fabrication of large-area, few-layered BN and C_x-BN nanosheets. *Adv. Mater.* **2011**, *23*, 4072-4076.

(31) Wang, X.-B.; Weng, Q.; Wang, X.; Li, X.; Zhang, J.; Liu, F.; Jiang, X.-F.; Guo, H.; Xu, N.; Golberg, D.; Bando, Y. Biomass-directed synthesis of 20 g high-quality boron nitride nanosheets for thermoconductive polymeric composites. *ACS Nano* **2014**, *8*, 9081-9088.

(32) Ahmad, P.; Khandaker, M. U.; Khan, Z. R.; Amin, Y. M. Synthesis of boron nitride nanotubes via chemical vapour deposition: a comprehensive review. *RSC Adv.* **2015**, *5*, 35116-35137.

(33) Oku, T.; Narita, I.; Koi, N.; Nishiwaki, A.; Suganuma, K.; Inoue, M.; Hiraga, K.; Matsuda, T.; Hirabayashi, M.; Tokoro, H. Boron nitride nanocage clusters, nanotubes, nanohorns, nanoparticles, and nanocapsules. In *BCN nanotubes and related nanostructures*, Springer: 2009; Vol. 6, pp 149-194.

(34) Zhi, C.; Bando, Y.; Tang, C.; Golberg, D. Boron nitride nanotubes. *Mater. Sci. Eng. R Rep.* **2010**, *70*, 92-111.

(35) Acharya, A.; Sharma, S.; Liu, X.; Zhang, D.; Yap, Y. K. A review on van der waals boron nitride quantum dots. *C* **2021**, *7*, 35.

(36) Lin, L.; Xu, Y.; Zhang, S.; Ross, I. M.; Ong, A. C. M.; Allwood, D. A. Fabrication and luminescence of monolayered boron nitride quantum dots. *Small* **2014**, *10*, 60-65.

(37) Li, H.; Tay, R. Y.; Tsang, S. H.; Zhen, X.; Teo, E. H. T. Controllable synthesis of highly luminescent boron nitride quantum dots. *Small* **2015**, *11*, 6491-6499.

(38) Liu, M.; Xu, Y.; Wang, Y.; Chen, X.; Ji, X.; Niu, F.; Song, Z.; Liu, J. Boron nitride quantum dots with solvent-regulated blue/green photoluminescence and electrochemiluminescent behavior for versatile applications. *Adv. Opt. Mater.* **2017**, *5*, 1600661.

(39) Jung, J.-H.; Kotal, M.; Jang, M.-H.; Lee, J.; Cho, Y.-H.; Kim, W.-J.; Oh, I.-K. Defect engineering route to boron nitride quantum dots and edge-hydroxylated

functionalization for bio-imaging. *RSC Adv.* **2016**, *6*, 73939-73946.

(40) Thangasamy, P.; Santhanam, M.; Sathish, M. Supercritical fluid facilitated disintegration of hexagonal boron nitride nanosheets to quantum dots and its application in cells imaging. *ACS Appl. Mater. Interfaces* **2016**, *8*, 18647-18651.

(41) Duong, N. M. H.; Glushkov, E.; Chernev, A.; Navikas, V.; Comtet, J.; Nguyen, M. A. P.; Toth, M.; Radenovic, A.; Tran, T. T.; Aharonovich, I. Facile production of hexagonal boron nitride nanoparticles by cryogenic exfoliation. *Nano Lett.* **2019**, *19*, 5417-5422.

(42) Ren, J.; Malfatti, L.; Enzo, S.; Carbonaro, C. M.; Calvillo, L.; Granozzi, G.; Innocenzi, P. Boron oxynitride two-colour fluorescent dots and their incorporation in a hybrid organic-inorganic film. *J. Colloid Interface Sci.* **2020**, *560*, 398-406.

(43) Liu, B.; Yan, S.; Song, Z.; Liu, M.; Ji, X.; Yang, W.; Liu, J. One-step synthesis of boron nitride quantum dots: Simple chemistry meets delicate nanotechnology. *Chem. Eur. J.* **2016**, *22*, 18899-18907.

(44) Yao, Q.; Feng, Y.; Rong, M.; He, S.; Chen, X. Determination of nickel(II) via quenching of the fluorescence of boron nitride quantum dots. *Microchim. Acta* **2017**, *184*, 4217-4223.

(45) Huo, B.; Liu, B.; Chen, T.; Cui, L.; Xu, G.; Liu, M.; Liu, J. One-step synthesis of fluorescent boron nitride quantum dots via a hydrothermal strategy using melamine as nitrogen source for the detection of ferric ions. *Langmuir* **2017**, *33*, 10673-10678.

(46) Yang, K.; Jia, P.; Hou, J.; Bu, T.; Sun, X.; Liu, Y.; Wang, L. Innovative dual-emitting ratiometric fluorescence sensor for tetracyclines detection based on boron nitride quantum dots and europium ions. *ACS Sustainable Chem. Eng.* **2020**, *8*, 17185-17193.

(47) Jerome, R.; Sundramoorthy, A. K. Hydrothermal synthesis of boron nitride quantum dots/poly(luminol) nanocomposite for selective detection of ascorbic acid. *J. Electrochem. Soc.* **2019**, *166*, B3017-B3024.

(48) Liu, Y.; Wang, M.; Nie, Y.; Zhang, Q.; Ma, Q. Sulfur regulated boron nitride quantum dots electrochemiluminescence with amplified surface plasmon coupling strategy for BRAF gene detection. *Anal. Chem.* **2019**, *91*, 6250-6258.

(49) Liang, Z.; Zhang, Q.; Nie, Y.; Zhang, X.; Ma, Q. Polarized-electrochemiluminescence biosensor based on surface plasmon coupling strategy and fluorine-doped BN quantum dots. *Anal. Chem.* **2020**, *92*, 9223-9229.

(50) Ren, J.; Innocenzi, P. 2D boron nitride heterostructures: Recent advances and future challenges. *Small Struct.* **2021**, *2*, 2100068.

(51) Wang, J.; Ma, F.; Liang, W.; Wang, R.; Sun, M. Optical, photonic and optoelectronic properties of graphene, h-BN and their hybrid materials. *Nanophotonics* **2017**, *6*, 943-976.

(52) Watanabe, K.; Taniguchi, T.; Kanda, H. Direct-bandgap properties and evidence for ultraviolet lasing of hexagonal boron nitride single crystal. *Nat. Mater.* **2004**, *3*, 404-409.

(53) Cassabois, G.; Valvin, P.; Gil, B. Hexagonal boron nitride is an indirect bandgap semiconductor. *Nat. Photonics* **2016**, *10*, 262-266.

(54) Arnaud, B.; Lebègue, S.; Rabiller, P.; Alouani, M. Huge excitonic effects in layered hexagonal boron nitride. *Phys. Rev. Lett.* **2006**, *96*, 026402.

(55) Sainsbury, T.; Satti, A.; May, P.; Wang, Z.; McGovern, I.; Gun'ko, Y. K.; Coleman, J. Oxygen radical functionalization of boron nitride nanosheets. *J. Am. Chem. Soc.* **2012**, *134*, 18758-18771.

(56) Museur, L.; Feldbach, E.; Kanaev, A. Defect-related photoluminescence of hexagonal boron nitride. *Phys. Rev. B* **2008**, *78*, 155204.

(57) Sagar, T. C.; Chinthapenta, V. Effect of substitutional and vacancy defects on the electrical and mechanical properties of 2D-hexagonal boron nitride. *J. Mol. Model.* **2020**, *26*, 192.

(58) Hernández-Mínguez, A.; Lähnemann, J.; Nakhaie, S.; Lopes, J. M. J.; Santos, P. V. Luminescent defects in a few-layer h-BN film grown by molecular beam epitaxy. *Phys. Rev. Applied* **2018**, *10*, 044031.

(59) Tang, C.; Bando, Y.; Zhi, C.; Golberg, D. Boron–oxygen luminescence centres in boron–nitrogen systems. *Chem. Commun.* **2007**, 4599-4601.

(60) Nguyen, V.; Yan, L.; Zhao, N.; Van Canh, N.; Hang, N. T. N.; Le, P. H. Tuning photoluminescence of boron nitride quantum dots via surface functionalization by

femtosecond laser ablation. *J. Mol. Struct.* **2021**, *1244*, 130922.

(61) Lei, Z.; Xu, S.; Wan, J.; Wu, P. Facile preparation and multifunctional applications of boron nitride quantum dots. *Nanoscale* **2015**, *7*, 18902-18907.

(62) Fan, L.; Zhou, Y.; He, M.; Tong, Y.; Zhong, X.; Fang, J.; Bu, X. Facile microwave approach to controllable boron nitride quantum dots. *J. Mater. Sci.* **2017**, *52*, 13522-13532.

(63) Ding, Y.; He, P.; Li, S.; Chang, B.; Zhang, S.; Wang, Z.; Chen, J.; Yu, J.; Wu, S.; Zeng, H.; Tao, L. Efficient full-color boron nitride quantum dots for thermostable flexible displays. *ACS Nano* **2021**, *15*, 14610-14617.

(64) Zhou, C.; Lai, C.; Zhang, C.; Zeng, G.; Huang, D.; Cheng, M.; Hu, L.; Xiong, W.; Chen, M.; Wang, J.; Yang, Y.; Jiang, L. Semiconductor/boron nitride composites: Synthesis, properties, and photocatalysis applications. *Appl. Catal. B* **2018**, *238*, 6-18.

(65) Li, X.; Zhang, J.; Zhang, S.; Xu, S.; Wu, X.; Chang, J.; He, Z. Hexagonal boron nitride composite photocatalysts for hydrogen production. *J. Alloys Compd.* **2021**, *864*, 158153.

(66) Cao, Y.; Zhang, R.; Zhou, T.; Jin, S.; Huang, J.; Ye, L.; Huang, Z.; Wang, F.; Zhou, Y. B–O Bonds in ultrathin boron nitride nanosheets to promote photocatalytic carbon dioxide conversion. *ACS Appl. Mater. Interfaces* **2020**, *12*, 9935-9943.

(67) Liu, Q.; Chen, C.; Du, M.; Wu, Y.; Ren, C.; Ding, K.; Song, M.; Huang, C. Porous hexagonal boron nitride sheets: Effect of hydroxyl and secondary amino groups on photocatalytic hydrogen evolution. *ACS Appl. Nano Mater.* **2018**, *1*, 4566-4575.

(68) Liu, D.; Zhang, M.; Xie, W.; Sun, L.; Chen, Y.; Lei, W. Porous BN/TiO_2 hybrid nanosheets as highly efficient visible-light-driven photocatalysts. *Appl. Catal. B* **2017**, *207*, 72-78.

(69) Zhao, G.; Zhang, F.; Wu, Y.; Hao, X.; Wang, Z.; Xu, X. One-step exfoliation and hydroxylation of boron nitride nanosheets with enhanced optical limiting performance. *Adv. Opt. Mater.* **2016**, *4*, 141-146.

(70) Xie, Z.; Wu, Y.; Sun, X.; Liu, S.; Ma, F.; Zhao, G.; Hao, X.; Zhou, S. Ultra-broadband nonlinear optical response of two-dimensional h-BN nanosheets and their hybrid gel glasses. *Nanoscale* **2018**, *10*, 4276-4283.

(71) Cai, Q.; Mateti, S.; Watanabe, K.; Taniguchi, T.; Huang, S.; Chen, Y.; Li, L. H. Boron nitride nanosheet-veiled gold nanoparticles for surface-enhanced raman scattering. *ACS Appl. Mater. Interfaces* **2016**, *8*, 15630-15636.

(72) Cai, Q.; Li, L. H.; Yu, Y.; Liu, Y.; Huang, S.; Chen, Y.; Watanabe, K.; Taniguchi, T. Boron nitride nanosheets as improved and reusable substrates for gold nanoparticles enabled surface enhanced Raman spectroscopy. *Phys. Chem. Chem. Phys.* **2015**, *17*, 7761-7766.

(73) Zhang, K.; Feng, Y.; Wang, F.; Yang, Z.; Wang, J. Two dimensional hexagonal boron nitride (2D-hBN): synthesis, properties and applications. *J. Mater. Chem. C* **2017**, *5*, 11992-12022.

(74) Tang, C.; Cheng, B.; Aldosary, M.; Wang, Z.; Jiang, Z.; Watanabe, K.; Taniguchi, T.; Bockrath, M.; Shi, J. Approaching quantum anomalous Hall effect in proximity-coupled YIG/graphene/h-BN sandwich structure. *APL Mater.* **2018**, *6*, 026401.

(75) Ahmad, P.; Khandaker, M. U.; Muhammad, N.; Khan, G.; Rehman, F.; Khan, A. S.; Ullah, Z.; Khan, A.; Ali, H.; Ahmed, S. M.; Rauf Khan, M. A.; Iqbal, J.; Khan, A. A.; Irshad, M. I. Fabrication of hexagonal boron nitride quantum dots via a facile bottom-up technique. *Ceram. Int.* **2019**, *45*, 22765-22768.

(76) Yang, Y.; Zhang, C.; Huang, D.; Zeng, G.; Huang, J.; Lai, C.; Zhou, C.; Wang, W.; Guo, H.; Xue, W.; Deng, R.; Cheng, M.; Xiong, W. Boron nitride quantum dots decorated ultrathin porous g-C_3N_4: Intensified exciton dissociation and charge transfer for promoting visible-light-driven molecular oxygen activation. *Appl. Catal. B* **2019**, *245*, 87-99.

(77) Lin, Z.; Liu, Y.; Raghavan, S.; Moon, K.-s.; Sitaraman, S. K.; Wong, C.-p. Magnetic alignment of hexagonal boron nitride platelets in polymer matrix: Toward high performance anisotropic polymer composites for electronic encapsulation. *ACS Appl. Mater. Interfaces* **2013**, *5*, 7633-7640.

(78) Song, L.; Ci, L.; Lu, H.; Sorokin, P. B.; Jin, C.; Ni, J.; Kvashnin, A. G.; Kvashnin, D. G.; Lou, J.; Yakobson, B. I.; Ajayan, P. M. Large scale growth and characterization of atomic hexagonal boron nitride layers. *Nano Lett.* **2010**, *10*, 3209-3215.

(79) Kim, S. M.; Hsu, A.; Park, M. H.; Chae, S. H.; Yun, S. J.; Lee, J. S.; Cho, D.-H.;

Fang, W.; Lee, C.; Palacios, T.; Dresselhaus, M.; Kim, K. K.; Lee, Y. H.; Kong, J. Synthesis of large-area multilayer hexagonal boron nitride for high material performance. *Nat. Commun.* **2015**, *6*, 8662.

(80) Cretu, O.; Lin, Y.-C.; Koshino, M.; Tizei, L. H. G.; Liu, Z.; Suenaga, K. Structure and local chemical properties of boron-terminated tetravacancies in hexagonal boron nitride. *Phys. Rev. Lett.* **2015**, *114*, 075502.

(81) Qu, W.; Chen, X.; Ke, C. Temperature-dependent frictional properties of ultra-thin boron nitride nanosheets. *Appl. Phys. Lett.* **2017**, *110*, 143110.

(82) Göddenhenrich, T.; Müller, S.; Heiden, C. A lateral modulation technique for simultaneous friction and topography measurements with the atomic force microscope. *Rev. Sci. Instrum.* **1994**, *65*, 2870-2873.

(83) Zhu, T.; Liang, Y.; Zhang, C.; Wang, Z.; Dong, M.; Wang, C.; Yang, M.; Goto, T.; Tu, R.; Zhang, S. A high-throughput synthesis of large-sized single-crystal hexagonal boron nitride on a Cu–Ni gradient enclosure. *RSC Adv.* **2020**, *10*, 16088-16093.

(84) Wen, Y.; Shang, X.; Dong, J.; Xu, K.; He, J.; Jiang, C. Ultraclean and large-area monolayer hexagonal boron nitride on Cu foil using chemical vapor deposition. *Nanotechnology* **2015**, *26*, 275601.

(85) Liu, D.; Chen, X.; Yan, Y.; Zhang, Z.; Jin, Z.; Yi, K.; Zhang, C.; Zheng, Y.; Wang, Y.; Yang, J.; Xu, X.; Chen, J.; Lu, Y.; Wei, D.; Wee, A. T. S.; Wei, D. Conformal hexagonal-boron nitride dielectric interface for tungsten diselenide devices with improved mobility and thermal dissipation. *Nat. Commun.* **2019**, *10*, 1188.

(86) Yao, K.; Finney, N. R.; Zhang, J.; Moore, S. L.; Xian, L.; Tancogne-Dejean, N.; Liu, F.; Ardelean, J.; Xu, X.; Halbertal, D.; Watanabe, K.; Taniguchi, T.; Ochoa, H.; Asenjo-Garcia, A.; Zhu, X.; Basov, D. N.; Rubio, A.; Dean, C. R.; Hone, J.; Schuck, P. J. Enhanced tunable second harmonic generation from twistable interfaces and vertical superlattices in boron nitride homostructures. *Sci. Adv.* **2021**, *7*, eabe8691.

(87) Battiston, G. A.; Berto, D.; Convertino, A.; Emiliani, D.; Figueras, A.; Gerbasi, R.; Viticoli, S. PECVD of h-BN and c-BN films from boranedimethylamine as a single source precursor. *Electrochim. Acta* **2005**, *50*, 4600-4604.

(88) Ulrich, S.; Scherer, J.; Schwan, J.; Barzen, I.; Jung, K.; Scheib, M.; Ehrhardt, H.

Preparation of cubic boron nitride films by radio frequency magnetron sputtering and radio frequency ion plating. *Appl. Phys. Lett.* **1996**, *68*, 909-911.

(89) Shen, T.; Liu, S.; Yan, W.; Wang, J. Highly efficient preparation of hexagonal boron nitride by direct microwave heating for dye removal. *J. Mater. Sci.* **2019**, *54*, 8852-8859.

(90) Huang, C.; Chen, C.; Ye, X.; Ye, W.; Hu, J.; Xu, C.; Qiu, X. Stable colloidal boron nitride nanosheet dispersion and its potential application in catalysis. *J. Mater. Chem. A* **2013**, *1*, 12192-12197.

(91) Nautiyal, P.; Loganathan, A.; Agrawal, R.; Boesl, B.; Wang, C.; Agarwal, A. Oxidative unzipping and transformation of high aspect ratio boron nitride nanotubes into "white graphene oxide" platelets. *Sci. Rep.* **2016**, *6*, 29498.

(92) Andrews, L.; Burkholder, T. R. Infrared spectra of molecular $B(OH)_3$ and HOBO in solid argon. *J. Chem. Phys.* **1992**, *97*, 7203-7210.

(93) Gorbachev, R. V.; Riaz, I.; Nair, R. R.; Jalil, R.; Britnell, L.; Belle, B. D.; Hill, E. W.; Novoselov, K. S.; Watanabe, K.; Taniguchi, T.; Geim, A. K.; Blake, P. Hunting for monolayer boron nitride: Optical and raman signatures. *Small* **2011**, *7*, 465-468.

(94) Reich, S.; Ferrari, A. C.; Arenal, R.; Loiseau, A.; Bello, I.; Robertson, J. Resonant Raman scattering in cubic and hexagonal boron nitride. *Phys. Rev. B* **2005**, *71*, 205201.

(95) Chen, C.; Yin, D.; Kato, T.; Taniguchi, T.; Watanabe, K.; Ma, X.; Ye, H.; Ikuhara, Y. Stabilizing the metastable superhard material wurtzite boron nitride by three-dimensional networks of planar defects. *Proc. Natl. Acad. Sci. U.S.A.* **2019**, *116*, 11181-11186.

(96) Ohba, N.; Miwa, K.; Nagasako, N.; Fukumoto, A. First-principles study on structural, dielectric, and dynamical properties for three BN polytypes. *Phys. Rev. B* **2001**, *63*, 115207.

(97) Aradi, E.; Naidoo, S. R.; Cummings, F.; Motochi, I.; Derry, T. E. Cross-sectional transmission electron microscopy studies of boron ion implantation in hexagonal boron nitride. *Diam. Relat. Mater.* **2019**, *92*, 168-173.

(98) Li, L. H.; Cervenka, J.; Watanabe, K.; Taniguchi, T.; Chen, Y. Strong oxidation resistance of atomically thin boron nitride nanosheets. *ACS Nano* **2014**, *8*, 1457-1462.

(99) Hou, X.; Wang, M.; Fu, L.; Chen, Y.; Jiang, N.; Lin, C.-T.; Wang, Z.; Yu, J. Boron

nitride nanosheet nanofluids for enhanced thermal conductivity. *Nanoscale* **2018**, *10*, 13004-13010.

(100)   Song, Y.; Zhang, C.; Li, B.; Ding, G.; Jiang, D.; Wang, H.; Xie, X. Van der Waals epitaxy and characterization of hexagonal boron nitride nanosheets on graphene. *Nanoscale Res. Lett.* **2014**, *9*, 367.

(101)   Ingo, G. M.; Padeletti, G.; de Caro, T.; Riccucci, C.; Faraldi, F.; Curulli, A.; Mezzi, A.; Piccinini, M. Novel route to high-yield synthesis of sp^2-hybridized boron nitride nanoplates on stainless steel. *J. Mater. Chem.* **2011**, *21*, 10268-10272.

(102)   Chubarov, M.; Högberg, H.; Henry, A.; Pedersen, H. Review article: Challenge in determining the crystal structure of epitaxial 0001 oriented sp^2-BN films. *J. Vac. Sci. Technol.* **2018**, *36*, 030801.

(103)   Holder, C. F.; Schaak, R. E. Tutorial on powder X-ray diffraction for characterizing nanoscale materials. *ACS Nano* **2019**, *13*, 7359-7365.

(104)   Chubarov, M.; Pedersen, H.; Högberg, H.; Filippov, S.; Engelbrecht, J. A. A.; O'Connel, J.; Henry, A. Boron nitride: A new photonic material. *Physica B Condens. Matter* **2014**, *439*, 29-34.

(105)   Schimpf, C.; Motylenko, M.; Rafaja, D. Quantitative description of microstructure defects in hexagonal boron nitrides using X-ray diffraction analysis. *Mater. Charact.* **2013**, *86*, 190-199.

(106)   Sharma, S.; Kalita, G.; Vishwakarma, R.; Zulkifli, Z.; Tanemura, M. Opening of triangular hole in triangular-shaped chemical vapor deposited hexagonal boron nitride crystal. *Sci. Rep.* **2015**, *5*, 10426.

(107)   Tauc, J. Optical properties and electronic structure of amorphous Ge and Si. *Mater. Res. Bull.* **1968**, *3*, 37-46.

(108)   Caldwell, J. D.; Aharonovich, I.; Cassabois, G.; Edgar, J. H.; Gil, B.; Basov, D. N. Photonics with hexagonal boron nitride. *Nat. Rev. Mater.* **2019**, *4*, 552-567.

(109)   Jiang, H. X.; Lin, J. Y. Review—Hexagonal boron nitride epilayers: Growth, optical properties and device applications. *ECS J. Solid State Sci. Technol.* **2016**, *6*, Q3012-Q3021.

(110)   Li, Q.; Zheng, Y.; Hou, X.; Yang, T.; Liang, T.; Zheng, J. A wide range

photoluminescence intensity-based temperature sensor developed with BN quantum dots and the photoluminescence mechanism. *Sens. Actuators B Chem.* **2020**, *304*, 127353.

(111)   Chen, H.; Yang, Z.; Guo, W.; Dunlap, J. R.; Liang, J.; Sun, Y.; Jie, K.; Wang, S.; Fu, J.; Dai, S. From highly purified boron nitride to boron nitride-based heterostructures: An inorganic precursor-based strategy. *Adv. Funct. Mater.* **2019**, *29*, 1906284.

(112)   Li, J.; Yi, M.; Shen, Z.; Ma, S.; Zhang, X.; Xing, Y. Experimental study on a designed jet cavitation device for producing two-dimensional nanosheets. *Sci. China Technol. Sci.* **2012**, *55*, 2815-2819.

(113)   Yi, M.; Shen, Z.; Zhu, J. A fluid dynamics route for producing graphene and its analogues. *Chin. Sci. Bull.* **2014**, *59*, 1794-1799.

(114)   Xiao, F.; Naficy, S.; Casillas, G.; Khan, M. H.; Katkus, T.; Jiang, L.; Liu, H.; Li, H.; Huang, Z. Edge-hydroxylated boron nitride nanosheets as an effective additive to improve the thermal response of hydrogels. *Adv. Mater.* **2015**, *27*, 7196-7203.

(115)   Shi, L.; Wang, D.; Song, W.; Shao, D.; Zhang, W.-P.; Lu, A.-H. Edge-hydroxylated boron nitride for oxidative dehydrogenation of propane to propylene. *ChemCatChem* **2017**, *9*, 1788-1793.

(116)   Ravan, B. A.; Jafari, H. DFT study on electronic and optical properties of halogen-adsorbed hexagonal boron nitride. *Comput. Condens. Matter.* **2019**, *21*, e00416.

(117)   Zunger, A.; Katzir, A.; Halperin, A. Optical properties of hexagonal boron nitride. *Phys. Rev. B* **1976**, *13*, 5560-5573.

(118)   Yamijala, S. S.; Bandyopadhyay, A.; Pati, S. K. Structural stability, electronic, magnetic, and optical properties of rectangular graphene and boron nitride quantum dots: Effects of size, substitution, and electric field. *J. Phys. Chem. C* **2013**, *117*, 23295-23304.

(119)   Frisch, M. J.; Trucks, G. W.; Schlegel, H. B.; Scuseria, G. E.; Robb, M. A.; Cheeseman, J. R.; Scalmani, G.; Barone, V.; Petersson, G. A.; Nakatsuji, H.; Li, X.; Caricato, M.; Marenich, A. V.; Bloino, J.; Janesko, B. G.; Gomperts, R.; Mennucci, B.; Hratchian, H. P.; Ortiz, J. V.; Izmaylov, A. F.; Sonnenberg, J. L.; Williams; Ding, F.;

Lipparini, F.; Egidi, F.; Goings, J.; Peng, B.; Petrone, A.; Henderson, T.; Ranasinghe, D.; Zakrzewski, V. G.; Gao, J.; Rega, N.; Zheng, G.; Liang, W.; Hada, M.; Ehara, M.; Toyota, K.; Fukuda, R.; Hasegawa, J.; Ishida, M.; Nakajima, T.; Honda, Y.; Kitao, O.; Nakai, H.; Vreven, T.; Throssell, K.; Montgomery Jr., J. A.; Peralta, J. E.; Ogliaro, F.; Bearpark, M. J.; Heyd, J. J.; Brothers, E. N.; Kudin, K. N.; Staroverov, V. N.; Keith, T. A.; Kobayashi, R.; Normand, J.; Raghavachari, K.; Rendell, A. P.; Burant, J. C.; Iyengar, S. S.; Tomasi, J.; Cossi, M.; Millam, J. M.; Klene, M.; Adamo, C.; Cammi, R.; Ochterski, J. W.; Martin, R. L.; Morokuma, K.; Farkas, O.; Foresman, J. B.; Fox, D. J. *Gaussian 16 Rev. C.01*, Wallingford, CT, 2016.

(120)   Becke, A. D. Density‐functional thermochemistry. III. The role of exact exchange. *J. Chem. Phys.* **1993**, *98*, 5648-5652.

(121)   Dennington;, R.; Keith;, T. A.; Millam, J. M. *GaussView, Version 6*, Semichem Inc., Shawnee Mission, 2016.

(122)   Innocenzi, P. Infrared spectroscopy of sol–gel derived silica-based films: a spectra-microstructure overview. *J. Non-Cryst. Solids* **2003**, *316*, 309-319.

(123)   Lin, C.-K. Theoretical study of nitrogen-doped graphene nanoflakes: Stability and spectroscopy depending on dopant types and flake sizes. *J. Comput. Chem.* **2018**, *39*, 1387-1397.

(124)   Doan, T. C.; Li, J.; Lin, J. Y.; Jiang, H. X. Charge carrier transport properties in layer structured hexagonal boron nitride. *AIP Adv.* **2014**, *4*, 107126.

(125)   Guo, Q.; Zhou, C.; Ma, Z.; Yang, X. Fundamentals of TiO_2 photocatalysis: Concepts, mechanisms, and challenges. *Adv. Mater.* **2019**, *31*, 1901997.

(126)   Singh, B.; Singh, K.; Kumar, M.; Thakur, S.; Kumar, A. Insights of preferred growth, elemental and morphological properties of BN/SnO_2 composite for photocatalytic applications towards organic pollutants. *Chem. Phys.* **2020**, *531*, 110659.

(127)   Wang, N.; Yang, G.; Wang, H.; Sun, R.; Wong, C.-P. Visible light-responsive photocatalytic activity of boron nitride incorporated composites. *Front. Chem.* **2018**, *6*, 440.

(128)   Classification of titanium dioxide published in EU Official Journal. EUR-Lex -32020R0217. http://data.europa.eu/eli/reg_del/2020/217/oj.

(129)   Singh, B.; kaur, G.; Singh, P.; Singh, K.; Sharma, J.; Kumar, M.; Bala, R.; Meena, R.; Sharma, S. K.; Kumar, A. Nanostructured BN–TiO$_2$ composite with ultra-high photocatalytic activity. *New J. Chem.* **2017**, *41*, 11640-11646.

(130)   Sheng, Y.; Yang, J.; Wang, F.; Liu, L.; Liu, H.; Yan, C.; Guo, Z. Sol-gel synthesized hexagonal boron nitride/titania nanocomposites with enhanced photocatalytic activity. *Appl. Surf. Sci.* **2019**, *465*, 154-163.

(131)   Malfatti, L.; Falcaro, P.; Pinna, A.; Lasio, B.; Casula, M. F.; Loche, D.; Falqui, A.; Marmiroli, B.; Amenitsch, H.; Sanna, R.; Mariani, A.; Innocenzi, P. Exfoliated graphene into highly ordered mesoporous titania films: Highly performing nanocomposites from integrated processing. *ACS Appl. Mater. Interfaces* **2014**, *6*, 795-802.

(132)   Kidchob, T.; Malfatti, L.; Marongiu, D.; Enzo, S.; Innocenzi, P. An alternative sol–gel route for the preparation of thin films in CeO$_2$–TiO$_2$ binary system. *Thin Solid Films* **2010**, *518*, 1653-1657.

(133)   Stagi, L.; Carbonaro, C. M.; Corpino, R.; Chiriu, D.; Ricci, P. C. Light induced TiO$_2$ phase transformation: Correlation with luminescent surface defects. *Phys. Status Solidi B* **2015**, *252*, 124-129.

(134)   Tian, F.; Zhang, Y.; Zhang, J.; Pan, C. Raman spectroscopy: A new approach to measure the percentage of anatase TiO$_2$ exposed (001) facets. *J. Phys. Chem. C* **2012**, *116*, 7515-7519.

(135)   Angelomé, P. C.; Andrini, L.; Calvo, M. E.; Requejo, F. G.; Bilmes, S. A.; Soler-Illia, G. J. A. A. Mesoporous anatase TiO$_2$ films: Use of Ti K XANES for the quantification of the nanocrystalline character and substrate effects in the photocatalysis behavior. *J. Phys. Chem. C* **2007**, *111*, 10886-10893.

(136)   Violi, I. L.; Perez, M. D.; Fuertes, M. C.; Soler-Illia, G. J. A. A. Highly ordered, accessible and nanocrystalline mesoporous TiO$_2$ thin films on transparent conductive substrates. *ACS Appl. Mater. Interfaces* **2012**, *4*, 4320-4330.

(137)   Yang, C.; Fan, H.; Xi, Y.; Chen, J.; Li, Z. Effects of depositing temperatures on structure and optical properties of TiO$_2$ film deposited by ion beam assisted electron beam evaporation. *Appl. Surf. Sci.* **2008**, *254*, 2685-2689.

(138)   Kumar, R.; Singh, R. K.; Yadav, S. K.; Savu, R.; Moshkalev, S. A. Mechanical pressure induced chemical cutting of boron nitride sheets into boron nitride quantum dots and optical properties. *J. Alloys Compd.* **2016**, *683*, 38-45.

(139)   Ibrahim, K. H.; Irannejad, M.; Wales, B.; Sanderson, J.; Yavuz, M.; Musselman, K. P. Simultaneous fabrication and functionalization of nanoparticles of 2D materials with hybrid optical properties. *Adv. Opt. Mater.* **2018**, *6*, 1701365.

(140)   Ogden, J. S.; Young, N. A. The characterisation of molecular boric acid by mass spectrometry and matrix isolation infrared spectroscopy. *J. Chem. Soc., Dalton Trans.* **1988**, 1645-1652.

(141)   Malfatti, L.; Kidchob, T.; Falcaro, P.; Costacurta, S.; Piccinini, M.; Guidi, M. C.; Marcelli, A.; Corrias, A.; Casula, M. F.; Amenitsch, H.; Innocenzi, P. Highly ordered self-assembled mesostructured membranes: Porous structure and pore surface coverage. *Microporous Mesoporous Mater.* **2007**, *103*, 113-122.

(142)   Pascuta, P.; Pop, L.; Rada, S.; Bosca, M.; Culea, E. The local structure of bismuth borate glasses doped with europium ions evidenced by FT-IR spectroscopy. *J. Mater. Sci. Mater. Electron.* **2008**, *19*, 424-428.

(143)   Peng, D.; Zhang, L.; Li, F.-F.; Cui, W.-R.; Liang, R.-P.; Qiu, J.-D. Facile and green approach to the synthesis of boron nitride quantum dots for 2,4,6-trinitrophenol sensing. *ACS Appl. Mater. Interfaces* **2018**, *10*, 7315-7323.

(144)   Khanaki, A.; Xu, Z.; Tian, H.; Zheng, R.; Zuo, Z.; Zheng, J.-G.; Liu, J. Self-assembled cubic boron nitride nanodots. *Sci. Rep.* **2017**, *7*, 4087.

(145)   Singh, B.; Kaur, G.; Singh, P.; Singh, K.; Kumar, B.; Vij, A.; Kumar, M.; Bala, R.; Meena, R.; Singh, A.; Thakur, A.; Kumar, A. Nanostructured boron nitride with high water dispersibility for boron neutron capture therapy. *Sci. Rep.* **2016**, *6*, 35535.

(146)   Sajid, A.; Reimers, J. R.; Ford, M. J. Defect states in hexagonal boron nitride: Assignments of observed properties and prediction of properties relevant to quantum computation. *Phys. Rev. B* **2018**, *97*, 064101.

(147)   Weston, L.; Wickramaratne, D.; Mackoit, M.; Alkauskas, A.; Van de Walle, C. G. Native point defects and impurities in hexagonal boron nitride. *Phys. Rev. B* **2018**, *97*, 214104.

(148)   Gao, G.; Mathkar, A.; Martins, E. P.; Galvão, D. S.; Gao, D.; Autreto, P. A. d. S.; Sun, C.; Cai, L.; Ajayan, P. M. Designing nanoscaled hybrids from atomic layered boron nitride with silver nanoparticle deposition. *J. Mater. Chem. A* **2014**, *2*, 3148-3154.

(149)   Kainthola, A.; Bijalwan, K.; Negi, S.; Sharma, H.; Dwivedi, C. Hydrothermal synthesis of highly stable boron nitride nanoparticles. *Mater. Today Proc.* **2020**, *28*, 138-140.

(150)   Angizi, S.; Hatamie, A.; Ghanbari, H.; Simchi, A. Mechanochemical green synthesis of exfoliated edge-functionalized boron nitride quantum dots: Application to vitamin c sensing through hybridization with gold electrodes. *ACS Appl. Mater. Interfaces* **2018**, *10*, 28819-28827.

(151)   Mackoit-Sinkevičienė, M.; Maciaszek, M.; Walle, C. G. V. d.; Alkauskas, A. Carbon dimer defect as a source of the 4.1 eV luminescence in hexagonal boron nitride. *Appl. Phys. Lett.* **2019**, *115*, 212101.

(152)   Mendelson, N.; Chugh, D.; Reimers, J. R.; Cheng, T. S.; Gottscholl, A.; Long, H.; Mellor, C. J.; Zettl, A.; Dyakonov, V.; Beton, P. H.; Novikov, S. V.; Jagadish, C.; Tan, H. H.; Ford, M. J.; Toth, M.; Bradac, C.; Aharonovich, I. Identifying carbon as the source of visible single-photon emission from hexagonal boron nitride. *Nat. Mater.* **2021**, *20*, 321-328.

(153)   Palafox, M. A. DFT computations on vibrational spectra: Scaling procedures to improve the wavenumbers. *Phys. Sci. Rev.* **2018**, *3*.

(154)   Lee, C.; Yang, W.; Parr, R. G. Development of the Colle-Salvetti correlation-energy formula into a functional of the electron density. *Phys. Rev. B* **1988**, *37*, 785-789.

(155)   Cai, Q.; Scullion, D.; Falin, A.; Watanabe, K.; Taniguchi, T.; Chen, Y.; Santos, E. J. G.; Li, L. H. Raman signature and phonon dispersion of atomically thin boron nitride. *Nanoscale* **2017**, *9*, 3059-3067.

(156)   Vuong, T. Q. P.; Cassabois, G.; Valvin, P.; Rousseau, E.; Summerfield, A.; Mellor, C. J.; Cho, Y.; Cheng, T. S.; Albar, J. D.; Eaves, L.; Foxon, C. T.; Beton, P. H.; Novikov, S. V.; Gil, B. Deep ultraviolet emission in hexagonal boron nitride grown by high-temperature molecular beam epitaxy. *2D Mater.* **2017**, *4*, 021023.

(157)   Hamdi, H.; Thiering, G.; Bodrog, Z.; Ivády, V.; Gali, A. Stone–Wales defects in hexagonal boron nitride as ultraviolet emitters. *npj Comput. Mater.* **2020**, *6*, 178.

(158)   Lee, S. H.; Jeong, H.; Okello, O. F. N.; Xiao, S.; Moon, S.; Kim, D. Y.; Kim, G.-Y.; Lo, J.-I.; Peng, Y.-C.; Cheng, B.-M.; Miyake, H.; Choi, S.-Y.; Kim, J. K. Improvements in structural and optical properties of wafer-scale hexagonal boron nitride film by post-growth annealing. *Sci. Rep.* **2019**, *9*, 10590.

(159)   Singh, R. S.; Tay, R. Y.; Chow, W. L.; Tsang, S. H.; Mallick, G.; Teo, E. H. T. Band gap effects of hexagonal boron nitride using oxygen plasma. *Appl. Phys. Lett.* **2014**, *104*, 163101.

(160)   Wang, Y.; Shi, Z.; Yin, J. Boron nitride nanosheets: large-scale exfoliation in methanesulfonic acid and their composites with polybenzimidazole. *J. Mater. Chem.* **2011**, *21*, 11371-11377.

(161)   Cai, W.; Hong, N.; Feng, X.; Zeng, W.; Shi, Y.; Zhang, Y.; Wang, B.; Hu, Y. A facile strategy to simultaneously exfoliate and functionalize boron nitride nanosheets via Lewis acid-base interaction. *Chem. Eng. J.* **2017**, *330*, 309-321.

(162)   Kong, D.; Zhang, D.; Guo, H.; Zhao, J.; Wang, Z.; Hu, H.; Xu, J.; Fu, C. Functionalized boron nitride nanosheets/poly(l-lactide) nanocomposites and their crystallization behavior. *Polymers* **2019**, *11*, 440.

(163)   Zhou, S.; Xu, T.; Jiang, F.; Song, N.; Shi, L.; Ding, P. High thermal conductivity property of polyamide-imide/boron nitride composite films by doping boron nitride quantum dots. *J. Mater. Chem. C* **2019**, *7*, 13896-13903.

(164)   Zhan, Y.; Yang, J.; Guo, L.; Luo, F.; Qiu, B.; Hong, G.; Lin, Z. Targets regulated formation of boron nitride quantum dots – Gold nanoparticles nanocomposites for ultrasensitive detection of acetylcholinesterase activity and its inhibitors. *Sens. Actuators B Chem.* **2019**, *279*, 61-68.

(165)   Lu, Q.; Zhao, Q.; Yang, T.; Zhai, C.; Wang, D.; Zhang, M. Preparation of boron nitride nanoparticles with oxygen doping and a study of their room-temperature ferromagnetism. *ACS Appl. Mater. Interfaces* **2018**, *10*, 12947-12953.

(166)   Rudolph, W. W. Raman- and infrared-spectroscopic investigations of dilute aqueous phosphoric acid solutions. *Dalton Trans.* **2010**, *39*, 9642-9653.

(167)   Elias, C.; Valvin, P.; Pelini, T.; Summerfield, A.; Mellor, C. J.; Cheng, T. S.; Eaves, L.; Foxon, C. T.; Beton, P. H.; Novikov, S. V.; Gil, B.; Cassabois, G. Direct band-gap crossover in epitaxial monolayer boron nitride. *Nat. Commun.* **2019**, *10*, 2639.

Supplementary Notes

Note I: *Evaluation of band gap*

The bandgap, E_g, value can be evaluated by Tauc equation:

$$(\alpha h v)^n = A(h v - E_g)$$

where $h v$ is the photon energy, α energy the absorption coefficient (can be calculated from UV-Vis absorption spectra), A the absorption edge width parameter, E_g the band gap, and the exponent n depends on the type of optical transition in the gap region (n equals 2 for a direct transition). E_g could be obtained by extrapolating the linear region of plots of $(\alpha h v)^2$ versus energy ($h v$).

Note II: *Evaluation of crystallite size*

The crystallite size can be estimated by Scherrer equation:

$$L = K\lambda/\beta cos\theta$$

according to XRD patterns, where L is crystallite size to calculate, K is the Scherrer constant (here 0.89 for the integral breadth), λ is the X-ray wavelength in nm (0.154 nm in this thesis), β is the full-width at half-maximum (FWHM) of the diffraction peak in radian, and θ is the corresponding diffraction angle.

Note III: *Evaluation of residual H_3BO_3 in BONDs*
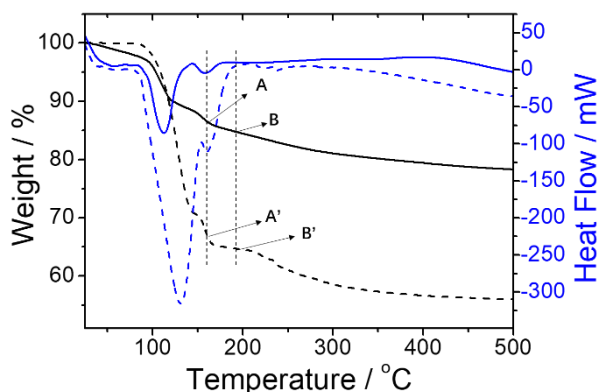
Figure 5.1.4

In **Figure 5.1.4**, the coordinates (x, y) for points A and B in BONDs line are (160, 86.58) and (194, 84.49), where x and y represent the value temperature (°C) and weight

(%). Meanwhile, the coordinates (x, y) for points A' and B' in of H_3BO_3 are (160, 64.65) and (194, 26.35).

From 160 to 194 °C, the weight loss for H_3BO_3 is caused by B-OH condensation. Therefore, we can calculate the residual H_3BO_3 in BONDs in the following equation:

$$\frac{64.65\text{-}26.35}{100\%} = \frac{86.58\text{-}84.49}{x}$$

and the calculated result of x is 5.5%. It means that the maximum residue of H_3BO_3 in BONDs is ~5.5%.

List of Publications

[1] Luigi Stagi, **Junkai Ren**, and Plinio Innocenzi*. From 2-D to 0-D boron nitride materials, the next challenge. *Materials*, **2019**, 12, 3905. https://doi.org/10.3390/ma12233905 (Ref.[13], Related to **Chapter 1**)

[2] **Junkai Ren**, Luigi Stagi*, and Plinio Innocenzi*. Hydroxylated boron nitride materials: from structures to functional applications. *J. Mater. Sci.*, **2021**, 56, 4053. https://doi.org/10.1007/s10853-020-05513-6 (Ref.[9], Related to **Chapter 1**)

[3] **Junkai Ren**, Luigi Stagi*, Carlo Maria Carbonaro, Luca Malfatti, Maria Francesca Casula, Pier Carlo Ricci, Antonio Del Rio, Francesco Bonaccorso, Laura Calvillo, Gaetano Granozzi, and Plinio Innocenzi*. Defect-assisted photoluminescence in hexagonal boron nitride nanosheets. *2D Mater.*, **2020**, 7, 045023. https://doi.org/10.1088/2053-1583/ababf0 (Ref.[22], Related to **Chapter 4.1**)

[4] **Junkai Ren**, Luigi Stagi*, Luca Malfatti, Sebastiano Garroni, Stefano Enzo, and Plinio Innocenzi*. Boron nitride-titania mesoporous film heterostructures. *Langmuir*, **2021**, 37, 5348. https://doi.org/10.1021/acs.langmuir.1c00460 (Ref.[26], Related to **Chapter 4.2**)

[5] **Junkai Ren**, Luca Malfatti, Stefano Enzo, Carlo Maria Carbonaro, Laura Calvillo, Gaetano Granozzi, and Plinio Innocenzi*. Boron oxynitride two-colour fluorescent dots and their incorporation in a hybrid organic-inorganic film. *J. Colloid Interface Sci.*, **2020**, 560, 398. https://doi.org/10.1016/j.jcis.2019.10.020 (Ref.[42], Related to **Chapter 5.1**)

[6] **Junkai Ren**, Luigi Stagi*, Luca Malfatti, Carlo Maria Carbonaro, Gaetano Granozzi, Laura Calvillo, Sebastiano Garroni, Stefano Enzo, and Plinio Innocenzi*. Engineering UV-emitting defects in h-BN nanodots by a top-down route. *Appl. Surf. Sci.*, **2021**, 567, 150727. https://doi.org/10.1016/j.apsusc.2021.150727 (Ref.[10], Related to **Chapter 5.2**)

[7] **Junkai Ren**, Luigi Stagi, and Plinio Innocenzi*. Fluorescent carbon dots in solid-state: from nanostructures to functional devices. *Prog. Solid. State Ch.*, **2021**, 62, 100295.

https://doi.org/10.1016/j.progsolidstchem.2020.100295 (Not including in the thesis)

[8] **Junkai Ren**, Luca Malfatti, and Plinio Innocenzi*. Citric acid derived carbon dots, the challenge of understanding the synthesis-structure relationship. *C*, **2021**, 7, 2.

https://doi.org/10.3390/c7010002 (Not including in the thesis)

[9] **Junkai Ren**, and Plinio Innocenzi*. 2D boron nitride heterostructures: Recent advances and future challenges. *Small Struct.*, **2021**, 2, 2100068.

https://doi.org/10.1002/sstr.202100068 (Not including in the thesis)

Acknowledgments

The PhD research presented in this thesis could not be finished during my three-year tenure without the assist and support from my professors, colleagues, and friends in University of Sassari (UNISS), University of Cagliari (UNICA), and other institutions.

First of all, I want to thank my principal investigator and supervisor, Prof. Plinio Innocenzi (UNISS), for providing me with an opportunity to study at Laboratory of Materials Science and Nanotechnology (LMNT) and experience life in Italy. Plinio is a bright and hardworking scientist, and I hope to emulate the energy and effort that he puts into his work. I would also like to thank him for continuous education, good caring, and great encouragement.

I wish to express my infinite gratitude to another brilliant advisor, Prof. Luca Malfatti (UNISS). During my time in LMNT, he has constantly educated and encouraged me. I would like to thank him for all the interesting discussions and his great passion for everything in not only my PhD project but also my life in Italy.

I would also like to thank my colleagues at LMNT and friends in Italy, Dr. Stefania Mura (UNISS), Dr. Luigi Stagi (UNISS), Dr. Manuela Meloni (UNISS), Dr. Robert Ludmerski (UNICA), Dr. Francesco Radica (University of Rome Tor Vergata), Dr. Valentina Paolucci (University of L'Aquila), and Mr. Matteo Poddighe (UNISS) for their accompany and help on my work and life in Porto Conte Ricerche. Meanwhile, my classmates Mr. Antonio Lacomini and Mr. Federico Riu (XXXIV-Cycle PhD students at UNISS) have helped me much in my study.

I also want to mention some people who have helped me solve the problems I encountered, in particular, the professional research issues. Prof. Stefano Enzo (UNISS) and Prof. Carlo Maria Carbonaro (UNICA) have given principle guidance on X-ray powder diffraction (XRD) analysis and ultrafast time-resolved fluorescence measurements, respectively. Dr. Sebastiano Garroni (UNISS) and Prof. Gaetano Granozzi (University of Padova) have assisted me with the operation of transmission electron microscopy (TEM) and X-ray photoelectron spectroscopy (XPS), respectively.

Prof. Francesco Bonaccorso (Istituto Italiano di Tecnologia) has provided me with the knowledge of two-dimensional materials.

Particularly, I would like to express my thanks to the Chinese Embassy in Italy and the Chinese Students and Scholars Union in Italy (CSSUI). During the Covid-19 period, they have provided me with important information on self-protection, as well as medical masks and disinfectants.

I am appreciative of Ms. Menghong Li for her company and encouragement. She has helped me greatly improve my spoken English.

Most importantly, I want to express my sincere gratitude to my family for their continuous support for my everything.

Lastly, I would also like to thank all people again in the three-year joint PhD program at UNISS and UNICA who have helped me in both life and study.

Alghero, April 2022

Junkai Ren / 任俊凯

Abbreviations

2D	two-dimensional
a-	amorphous
AFM	atomic force microscopy
ATR	attenuated total reflection
BN	boron nitride
BOND	boron-oxygen-nitrogen-hydrogen dot
c-	cubic
CL	cathodoluminescence
CVD	chemical vapor deposition
DFT	density functional theory
DLS	dynamic light scattering
DMF	dimethylformamide
DMSO	dimethyl sulfoxide
EDS	energy dispersive spectroscopy
EELS	electron energy loss spectroscopy
EG	ethylene glycol
FFT	fast Fourier transform
FTIR	Fourier-transform infrared spectroscopy
FWHM	full width at half-maximum
h-	hexagonal
HOMO	highest occupied molecular orbital
HR	high-resolution
IR	infrared
LDA	local density approximation
LO	longitudinal optic
LUMO	lowest unoccupied molecular orbital
MTES	methyltriethoxysilane

NMP	N-methyl-2-pyrrolidone
MOCVD	metal-organic chemical vapor deposition
NLO	nonlinear optical
NR	nanoribbon
NS	nanosheet
NT	nanotube
PL	photoluminescence
QD	quantum dot
QY	quantum yield
r-	rhombohedral
SAED	selected area electron diffraction
SEM	scanning electron microscopy
SERS	surface-enhanced Raman scattering
SW	Stone–Wales
t-	turbostratic
TD	time-dependent
TEM	transmission electron microscopy
TEOS	tetraethoxysilane
TGA	thermal gravimetric analysis
TO	transverse optical
TR	time-resolved
w-	wurtzite
UV-Vis	ultraviolet-visible
XRD	X-ray diffraction
XPS	X-ray photoelectron spectroscopy